Theory and simulation of the optical response of novel nanomaterials from visible to terahertz

Mohamed Ameen Poyli

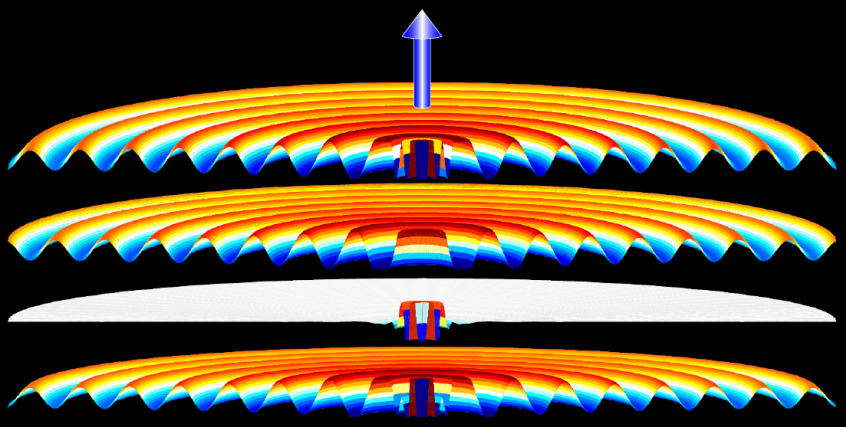

PhD Thesis

Supervised by
Dr. Rubén Esteban and Prof. Javier Aizpurua

2015

eman ta zabal zazu
Universidad del País Vasco
Euskal Herriko Unibertsitatea

Department of Materials Physics
UNIVERSIDAD DEL PAIS VASCO
THE UNIVERSITY OF THE BASQUE COUNTRY

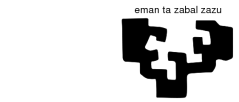

Theory and simulation of the optical response of novel nanomaterials from visible to terahertz

Thesis developed by

MOHAMED AMEEN POYLI

for the degree of

DOCTOR OF PHILOSOPHY IN PHYSICS

Supervised by

Dr. Rubén Esteban and Prof. Javier Aizpurua

Donostia-San Sebastián, Spain, June 2015.

Acknowledgements

This thesis would not have been possible without the efforts and support of many people. Here I would like to acknowledge and thank all who contributed to this thesis and supported me during the years of my graduation.

First of all I would like to express my immense gratitude to my thesis supervisor Prof. Javier Aizpurua. I am very thankful for the opportunity to work with him in the Theory of Nanophotonics Group. I am grateful for his supervision, his help to develop my scientific knowledge and his constant support that allowed me to work in a challenging position in his highly dynamic research group. I cannot thank Javier enough for the personal support he extended to me, especially during the final stressful months.

I would also like to express my gratitude to Dr. Rubén Esteban, also my thesis supervisor. I am specially thankful to Rubén for his dedication towards our project during the last years of my PhD. Rubén's supervision and help in coordinating the research findings and writing the thesis was invaluable towards the timely finishing of the thesis.

I thank Prof. Vyacheslav Silkin for his active collaboration in two of the main projects that are part of this thesis. I also thank my close collaborators, particularly, Dr. Ricardo Díez Muiño, Dr. Ilya Nechaev, Dr. Alexey Nikitin, Dr. Pablo Albella and Prof. Juan José Sáenz.

I acknowledge the Donostia International Physics Center (DIPC), the Material Physics Center (MPC), joint center of the Spanish Council for Scientific Research (CSIC) and the University of the Basque Country (UPV/EHU) for financial support.

I would like to thank all the members of the Theory of Nanophotonics Group for their support and for the friendly academic atmosphere. I appreciate the academic and friendly discussions and friendship with Mikołaj Schmidt, Garikoitz Aguirregabiria, Dr. Aitzol García-Etxarri, Tomas Neuman, Dr. Christos Tserkezis, Dr. Ollala Pérez, Prof. Nerea

Zabala and Prof. Alberto Rivacoba. I thank Garikoitz for helping me with the administrative procedures related to the thesis.

My study, research and life in San Sebastián are founded on the support from my family, relatives and friends. First of all I thank Sabeena Mannilthodi, my wife, for her love and constant support and encouragement. I specially thank Sabeena for taking care of our daughter in my absence. Many thanks to Amelia, my daughter, for keeping me happy during the final months of the PhD. I am deeply obliged to my parents for their unconditional love, for educating me and for their wholehearted support to build my career. I am indebted to my sisters and brother for their love and for taking care of our parents during these years. I extend my gratitude to my parents-in-law and family for their support to me and my family especially during my stay in Spain. I also thank all my relatives and friends back in India for their personal and emotional support.

Life away from home would have been tedious without my good friends in San Sebastián. I would like to thank specially Musthafa Kummali and Sadique Vellamarthodika for all the good moments we had in San Sebastián. I also thank Siddharth Gautham, Sitharamaiah, Debsindhu and Ravi Sharma among others who are too numerous to mention here.

Mohamed Ameen Poyli,
June 2015,
Donostia-San Sebastián.

Resumen

Los avances tecnológicos ocurridos a partir del siglo XVI han permitido explorar tanto el mundo microscópico como el macroscópico, gracias al desarrollo de dispositivos basados en lentes y espejos, desconocidos hasta entonces. El telescopio, inventado por Hans Lippershey y utilizado por Galileo Galilei y sus contemporáneos para realizar sus observaciones astronómicas, ha permitido revelar los misterios del cosmos. En la escala opuesta, el uso del microscopio por Zacharias Janssen, Robert Hooke y Antonie van Leeuwenhoek inauguró el estudio del mundo de los microorganismos y de lo diminuto.

En el siglo XVII se produjo un considerable avance en el estudio la naturaleza de la luz, con dos teorías que años más tarde se revelarían como complementarias: la teoría corpuscular de Isaac Newton y la teoría ondulatoria de Christiaan Huygens. Posteriormente, James Clerk Maxwell postuló la teoría electromagnética, mediante la cual estableció la naturaleza ondulatoria de la luz compuesta de oscilaciones de campos eléctricos y magnéticos y sentó las bases para la posterior aparición de la óptica física y de la fotónica. Unas décadas más tarde, el desarrollo de la óptica cuántica y de la dualidad onda-partícula de la luz permitieron una comprensión más profunda de la naturaleza de la luz.

Los microscopios modernos, apoyados por potentes ordenadores y tecnologías de alta precisión, permiten observar microorganismos y otros objetos muy pequeños a escala nanométrica, así como también estudiar procesos ultrarápidos en volúmenes reducidos. Sin embargo, el efecto de la difracción impone a menudo una barrera a nuestra capacidad de estudiar el mundo microscópico. Debido a su naturaleza ondulatoria, la óptica convencional no permite enfocar la luz por debajo de un área menor que aproximadamente la mitad su longitud de onda, es decir, en dimensiones inferiores a unos pocos cientos de nanómetros. Por tanto, objetos menores de unos 200 nanómetros no pueden ser distinguidos mediante microscopios ópticos convencionales.

Las partículas dieléctricas y metálicas de tamaño reducido exhiben modos electromagnéticos bien definidos, como se pone de manifiesto cuando son iluminadas por radiación electromagnética. Una de las principales características de estos modos es la presencia de ondas evanescentes que concentran la energía incidente cerca de la partícula, en una región muy pequeña de dimensiones comparables o incluso mucho más pequeñas que la longitud de onda incidente. Uno de los principales motores que han motivado el avance de la nanofotónica, una rama de la ciencia incluida dentro de la nanociencia y la nanotecnología, ha sido controlar y utilizar la luz más allá del límite de difracción.

Los esfuerzos iniciales en el campo de la nanofotónica se basaron en gran medida en tres tipos de sistemas: resonadores dieléctricos, puntos cuánticos y nanopartículas metálicas. Los resonadores basados en materiales dieléctricos son estructuras de tamaño normalmente micrométrico que exhiben resonancias de tipo Fabry-Pérot o similares, que permiten alcanzar factores de calidad extremadamente altos y un considerable aumento del campo eléctrico. Los puntos cuánticos son nanoestructuras semiconductoras cristalinas con niveles energéticos cuantizados debido al confinamiento de los pares electrón-hueco. Las transiciones entre estos niveles energéticos corresponden a menudo a frecuencias ópticas, y se manifiestan en forma de líneas espectrales muy estrechas de absorción y emisión, que pueden ser sintonizadas si se cambian las propiedades estructurales o el tamaño del sistema. Los metales nobles tales como la plata y el oro presentan gran interés en aplicaciones plasmónicas y nanofotónicas porque exhiben claras resonancias electromagnéticas en la región visible e infrarroja del espectro. Las resonancias en estructuras métalicas permiten localizar los campos electromagnéticos en regiones muy inferiores a lo permitido por el límite de difracción.

En la actualidad se buscan materiales alternativos a los anteriormente apuntados, que presenten propiedades ópticas novedosas y útiles para mejorar el control sobre los campos eléctricos y magnéticos, en regiones de dimensiones nanométricas y en un espectro lo más amplio posible. Dentro de este esfuerzo se encuadran diversos trabajos que han comenzado a investigar metales plasmónicos no convencionales, partículas pequeñas de materiales dieléctricos, cristales fonónicos y sistemas electrónicos bidimensiones, entre otros. De manera más específica, algunos metales plásmonicos no convencionales tales como el paladio, el platino y el cobalto pueden presentar pérdidas de energía superiores a las del oro o la plata pero, como contrapartida, pueden resultar útiles en aplicaciones tales como catálisis, sensórica de gases o magneto-óptica, por ejemplo. Por otra parte, las partículas dieléctricas de tamaño submicrométrico permiten excitar una fuerte respuesta eléctrica y magnética en el rango espectral del infrarrojo cercano. Los materiales polares

como el carburo de silicio también presentan resonancias ópticas claras en frecuencias que corresponden al infrarrojo medio, debidas a las vibraciones fonónicas de la estructura cristalina. Finalmente, el grafeno, los aislantes topológicos y otros materiales constituidos por gases electrónicos bidimensionales presentan propiedades ópticas muy peculiares que se extienden desde frecuencias de la luz visible hasta la radiación de terahertz, y permiten confinar la luz en volúmenes de dimensiones muy inferiores a la longitud de onda. Estos sistemas con pocas pérdidas pueden ser sintonizados mediante una fuente de tensión externa.

Esta tesis describe los estudios teóricos sobre las propiedades ópticas de diversas estructuras y nanomateriales que permiten controlar la luz en un amplio rango de frecuencias. En la **introducción** se describen estos aspectos de manera general en una gran variedad de materiales, incluyendo los plasmones en metales, las resonancias geométricas en partículas dieléctricas, las resonancias fonónicas en cristales polares y los plasmones bidimensionales en materiales como el grafeno o los aislantes topológicos.

El segundo capítulo investiga cómo obtener información sobre la absorción de hidrógeno en discos de paladio mediante el análisis de los cambios de la respuesta plasmónica. La absorción del hidrógeno es un proceso reversible de gran interés para el almacenamiento de energía y para el estudio de las propiedades catalíticas del paladio. A medida que los átomos de hidrógeno se incorporan a la estructura cristalina, las propiedades eléctricas y ópticas del material son modificadas de manera significativa. En concreto, este capítulo analiza los importantes cambios experimentados por las resonancias plasmónicas de diferentes sistemas, con particular interés en el caso de discos de paladio de cientos de nanómetros de diámetro, que presentan resonancias en el espectro visible e infrarrojo cercano.

Para estudiar este proceso en detalle, ha sido necesario emplear un enfoque multidimensional del problema. En un primer paso, los cálculos cuánticos permiten obtener la respuesta óptica de la estructura cristalina de Pd-H a nivel microscópico. A partir de estos cálculos se puede definir la constante dieléctrica de volumen del material, considerado como un sistema homogéneo. En los experimentos, sin embargo, se pueden formar regiones de propiedades diferentes, y por tanto, se define una constante dieléctrica efectiva de este material compuesto mediante el uso de la aproximación de medio efectivo de Bruggerman. Una vez definida la constante dieléctrica efectiva, la respuesta plasmónica de los discos o del nanosistema utilizado puede ser obtenida mediante la resolución de las ecuaciones electrodinámicas de Maxwell.

El análisis de los resultados y la comparación con los experimentos respaldan la interpretación de la absorción del hidrógeno como un proceso según el cual diversos dominios de Pd-H aparecen dentro del disco de paladio, dominios que no están plenamente hidrogenados y cuyo volumen total crece a medida que el hidrógeno es progresivamente absorbido por el sistema. Además de la importancia tecnológica del estudio del proceso de absorción de hidrógeno en paladio, este estudio también sirve para establecer una metodología de análisis de sistemas multidimensionales que puede resultar de utilidad en otros contextos.

El tercer capítulo estudia en detalle el acoplamiento entre las diversas resonancias eléctricas y magnéticas de dos partículas dieléctricas de radio 150 nanómetros. Algunos sistemas fotónicos basados en materiales dieléctricos han sido estudiados anteriormente. Sin embargo, aunque algunos de los dispositivos propuestos son capaces de concentrar la luz en regiones con dimensiones de cientos de nanometros, su tamaño fisico es generalmente de varios micrómetros al menos en alguna de las dimensiones. El sistema dieléctrico presentado en esta tesis, en cambio, es claramente submicrométrico en todas las dimensiones.

Una esfera suficientemente grande de un material dieléctrico de alta constante dieléctrica presenta diversas resonancias de carácter eléctrico o magnético a frecuencias visibles y del infrarrojo cercano, con una sección eficaz de extinción comparable con la de estructuras plasmónicas similares. Estos modos pueden interaccionar con los de una segunda esfera presente en su proximidad, dando lugar a resonancias de naturaleza eléctrica, magnética o mixta del sistema completo. En este trabajo se estudia en detalle el comportamiento de estos modos a medida que la distancia de separación entre las partículas es reducida hasta alcanzar unos pocos nanómetros. Este estudio se realiza mediante simulaciones electromagnéticas combinadas con un modelo analítico que incorpora el acoplamiento dipolar. La polarización de la onda plana utilizada para iluminar el sistema es un parámetro importante para determinar la orientación e interacción entre los diversos dipolos excitados en las esferas.

Los resultados obtenidos en este apartado son también de interés en aplicaciones prácticas. En particular, se describen con cierto detalle las ventajas que presentan las partículas dieléctricas en la identificación de moléculas que se encuentran en la cavidad nanométrica formada entre las dos esferas. De manera parecida a lo demostrado para diversos sistemas plasmónicos, aunque en menor medida, es posible conseguir un aumento del campo eléctrico en la cavidad que se traduzca en una mejora substancial de la señal emitida o absorbida debido a las diferentes transiciones de carácter eléctrico de la molécula,

facilitando la medición e identificación experimental de esta huella espectroscópica. Adicionalmente, las estructuras dieléctricas presentan la ventaja de un bajo nivel de pérdidas comparado con sistemas plasmónicos, un aspecto muy atractivo para diversas técnicas espectroscópicas. Por último, y debido a la posibilidad de aumentar la intensidad del campo magnético en la cavidad, estas estructuras resultan igualmente adecuadas para estudiar la señal emitida por transiciones de carácter magnético .

El cuarto capítulo trata la excitación de plasmones en películas delgadas de aislantes topológicos, y analiza la posibilidad de controlar el espín y la carga efectiva de estas resonancias mediante la iluminación y la geometría del sistema. Los sistemas electrónicos bidimensionales como el grafeno pueden ser descritos como un gas de electrones libres confinado en dos dimensiones, con resonancias plasmónicas similares a las presentes en sistemas metálicos. Los plasmones en estos materiales bidimensionales han generado un gran interés por el bajo nivel de pérdidas energéticas que presentan, porque pueden ser excitados tanto a frecuencias ópticas como de terahertz y, en especial, porque pueden ser sintonizados de manera relativamente sencilla usando una fuente de tensión externa. Los aislantes topológicos estudiados en este capítulo son materiales como el Bi_2Se_3, transparentes excepto en sus superficies, donde presentan los plasmones bidimensionales. Además de las ventajas de las bajas pérdidas de energía y de poder ser sintonizadas, las resonancias plasmónicas en estos materiales también ofrecen la posibilidad de controlar las propiedades de espín.

Para ser capaces de tratar estos sistemas, se ha seguido una metodología similar a la utilizada para estudiar la absorción de hidrógeno en sistemas de paladio. En primer lugar, un tratamiento cuántico permite definir las propiedades del material, en esta ocasión mediante la obtención de una conductividad del gas bidimensional de electrones. Una vez establecida la conductividad, la respuesta del sistema puede ser obtenida mediante un tratamiento electromagnético clásico, resolviendo las ecuaciones de Maxwell. Los resultados presentados en este capítulo revelan la importancia de describir correctamente la respuesta no local de la conductividad en la descripción precisa de las resonancias.

De manera más concreta, esta parte de la tesis explora inicialmente la respuesta plasmónica de un substrato de aislante topológico, para después concentrarse en películas delgadas del mismo material. En este último caso, los plasmones en cada una de las dos superficies planas se acoplan debido a la interacción de Coulomb para dar lugar a modos plasmónicos híbridos de carácter óptico o acústico, dependiendo de las simetrías de las cargas inducidas. Los modos ópticos presentan carga neta efectiva pero la suma del espín de las dos superficies resulta ser cero, mientras que los modos acústicos se caracterizan

por espín neto efectivo pero sin presencia de carga total. Se estudia cómo estos modos pueden ser excitados en películas delgadas de dimensiones laterales infinitas, así como en discos del mismo grosor y de diámetro de 50 o 600 nanómetros.

En estos materiales aislantes topológicos, una fuente de luz localizada en la cercanía del substrato o de las películas delgadas puede excitar modos plasmónicos propagantes de superficie. La distancia entre la fuente y la película delgada permite controlar la importancia relativa de los modos acústicos y ópticos, y por tanto de la carga y espín efectivos de la resonancia excitada. En el caso de discos delgados de dimensiones laterales finitas, se excitan modos plasmónicos localizados, muy estrechos espectralmente y confinados en volúmenes muy pequeños. La frecuencia de excitación depende del diámetro de los discos. La posibilidad de cambiar la conductividad del gas de electrones mediante una fuente de tensión externa ofrecería la capacidad de sintonizar estas resonancias una vez que el tamaño del disco ha sido fijado por el proceso de fabricación. Los modos acústicos pueden ser excitados por fuentes localizados, mientras que los modos ópticos pueden acoplarse tanto a fuentes localizadas como a ondas planas. La excitación de estos dos tipos de resonancias permite de nuevo obtener una respuesta fuertemente dominada por el espín efectivo o por la carga efectiva. Por tanto, las películas y discos delgados de aislantes topológicos se presentan como sistemas con grandes posibilidades para el control de las propiedades de espín o de carga a frecuencias infrarrojas y de terahertz, que podrian ser muy útiles, por ejemplo, en el diseño de futuros dispositivos plasmónicos y espintrónicos que puedan funcionar a velocidades muy elevadas.

Por último, esta tesis incluye tres **apéndices** que describen en detalle ciertos métodos matemáticos necesarios para obtener los resultados anteriores. El primer apéndice muestra la derivación de los coeficientes de Fresnel para superficies caracterizadas por la presencia de un gas de electrones bidimensional, iluminado por ondas planas, así como la utilización de estos coeficientes para el estudio de películas delgadas. El según apéndice presenta cómo tratar la respuesta de este tipo de estructuras en el caso de excitación dipolar mediante la descomposición de esta fuente de luz en ondas planas. El último apéndice describe y compara dos de las aproximaciones de medio efectivo más habituales para tratar las propiedades ópticas de materiales compuestos: el modelo de Maxwell-Garnett y el modelo de Bruggeman.

Contents

Chapter 1

Introduction

The control of light using lenses and mirrors developed during the 16^{th} century opened the door to access to two unknown realms of the universe, the macro cosmos and the microscopic world. The invention of the telescope by Hans Lippershey and its successive use by Galileo Galilei and his contemporaries for astronomical observations unveiled the sky and heavenly bodies [1, 2]. On the opposite scale, the microscopes of Zacharias Janssen, Robert Hooke and Antonie van Leeuwenhoek revealed the world of microorganisms and small particles [2–4].

The efforts to understand the fundamental nature of light intensified in the 17^{th} century with Isaac Newton's proposal of the corpuscular nature of light [5] and the wave theory of light by Christiaan Huygens [6]. James Clerk Maxwell set the theory of the electromagnetic nature of light and laid the foundation of electromagnetics, which would ultimately lead to the establishment of wave optics and photonics. A few decades later, progress in quantum mechanics and the development of the wave-particle dual description of photons resulted in a better fundamental understanding of the nature of light [7].

Modern microscopes, helped by computers and different high-precision control technologies enable observing small objects and microorganisms at nanometer dimensions as well as studying ultrafast processes happening in small dimensions. However the extent of the microscopic world accessible by light is usually constrained by the diffraction limit [8, 9]. Because of its wave nature, light cannot be focused by conventional optics to an area smaller than the dimension of about half of its wavelength, i.e., a few hundred nanometers [8, 9]. Therefore, conventional optics cannot be used for observing objects smaller than about 200 nm.

Small dielectric and metallic particles show well-defined electromagnetic modes that can be effectively excited when illuminated with electromagnetic radiation. These modes are characterized by intense evanescent fields strongly localized to very small regions in the vicinity of the particles, of dimensions comparable or even much smaller than the wavelength of light. The opportunity to access and control these sub-wavelength fields enables us to break the diffraction limit and triggers out the field of nanophotonics, in the context of the more general advances in nanoscience and nanotechnology [9, 10].

Many of the early works in the field of nanophotonics were focused on three types of systems, namely dielectric resonators [11–13], quantum dots [14–16] and metallic nanoparticles [17–20]. Typical dielectric resonators are micron sized structures of dielectric materials supporting strong Fabry-Pérot and similar optical resonances with very large quality factors and field enhancement [21, 22]. Quantum dots are nanocrystals of semiconducting materials, in which the light matter interaction is mediated by quantized excitonic energy levels in the particle due to the three dimensional confinement of excited electron-hole pairs. These energy levels are mainly active in the optical range and highly tunable showing sharp optical absorption and emission lines. Noble metals like gold and silver have been considered as suitable materials for plasmonic and nanophotonic applications because of their well-defined electromagnetic resonances in the visible and near-infrared region of the spectrum. Moreover, metallic structures also allow to localize electromagnetic fields to very small, sub-diffraction limit regions.

There is a strong interest in the search of alternative materials with novel properties to achieve even finer control of the electric and magnetic fields at nanometric dimensions and in a wider spectral regime. This brought the attention to non-conventional plasmonic metals [23–27], small particles of dielectric materials [28–30], phononic crystals [31, 32] and 2D electron systems [33–35]. Particularly, non-conventional plasmonic metals like palladium, platinum and cobalt show larger losses compared to gold and silver but can be useful for specific applications, for example, in catalysis, gas sensing and magneto-optics [25–27]. On the other hand, dielectric particles of submicrometric sizes show strong electric and magnetic response in the near-infrared range of the spectrum [28]. Polar materials like silicon carbide also show very well defined optical resonances in the mid-infrared range of the spectrum arising from the phononic vibrations of the lattice [31, 32, 36]. 2D electron systems like graphene and topological insulators with extraordinary electromagnetic properties in the whole range of the visible to THz offer particularly tight confinement of electromagnetic fields in extreme sub-wavelength dimensions, low losses and the possibility to tune the resonances externally [33–35].

In this thesis we present theoretical studies of the optical response of a variety of nanomaterials and systems, covering much of the electromagnetic spectrum from the visible to terahertz. In this chapter, we describe the relevant optical properties of these novel materials that will be studied throughout the different chapters of this thesis, with special emphasis in their applications in nanophotonics. In Chapter 2 the optical properties of palladium (Pd) modified by hydrogen are studied in the visible and near-infrared range of the spectrum for hydrogen sensing application. We discuss in Chapter 3, the strong electric and magnetic response of dielectric particles in the near-infrared range and their use for low-loss field enhanced spectroscopy. Finally, in Chapter 4, we study the charge and spin properties of electromagnetic collective excitations in topological insulators.

In the remaining part of this introductory chapter, we give a brief description of the general optical properties of these systems, including also the well known excitation of plasmons in Drude metals, the geometrical electromagnetic resonance in dielectric particles, the phononic resonances in polar crystals and the plasmon excitations in general 2D materials such as graphene.

1.1. Optical response of metals in the visible

Metallic structures support strong plasmonic resonances, given by the collective oscillation of the free electron gas. These resonances can can be understood using a classical Drude model based on the harmonic oscillator. In this model the metal is considered as a free electron gas loosely bound to the positive ionic core. This free electron gas oscillates in response to the electric field of the incident electromagnetic radiation. The resulting equation of motion for the free electron gas placed in an external electric field $\mathbf{E}$ can be written as [37]

$$m_e\ddot{\mathbf{x}} + m_e\gamma\dot{\mathbf{x}} = -e\mathbf{E}, \tag{1.1}$$

where m_e is the mass of electron, γ is the damping constant, e is the electron charge and $\mathbf{x}$ is the displacement of the free electron gas from its mean position. We use SI units unless otherwise specified. Let us assume a harmonic time dependence for the applied field, $\mathbf{E}(t) = \mathbf{E}_0 e^{-i\omega t}$, oscillating with an angular frequency ω and amplitude $\mathbf{E}_0$. By considering that the oscillating free electrons modify the macroscopic polarizability of the medium, this model allows to derive a complex relative dielectric function $\varepsilon_m(\omega)$ for

the metals given by

$$\varepsilon_m(\omega) = \varepsilon_\infty - \frac{\omega_P^2}{\omega^2 + i\gamma\omega}. \tag{1.2}$$

ε_∞ is the background dielectric function of the interband transitions and ω_P is the characteristic frequency of the free electron gas, called plasma frequency given by (in SI units)

$$\omega_P = \sqrt{\frac{ne^2}{\varepsilon_0 m}}, \tag{1.3}$$

where n is the free electron density and ε_0 is the electric permittivity of free space. For an ideal free electron gas ($\varepsilon_\infty = 1$), in the absence of damping, Eq. (1.2) acquires the simple form,

$$\varepsilon_m(\omega) = 1 - \frac{\omega_P^2}{\omega^2}. \tag{1.4}$$

At $\omega = \omega_P$, a Drude metal shows a dielectric function $\varepsilon_m(\omega) = 0$, thus supporting longitudinal collective oscillation of free electrons, so-called bulk plasmons. Above the plasma frequency, and assuming γ=0, ideal Drude metals are transparent to electromagnetic radiation and the free electron plasma supports propagation of transverse electromagnetic (light) waves.

The dispersion relation for the propagating bulk plasmons in a Drude-like metal is given by

$$\omega^2 = \omega_P^2 + c^2 q_P^2, \tag{1.5}$$

where c is the speed of light in vacuum and q_P is the propagation vector $2\pi/\lambda_P$, λ_P being the plasmon wavelength. The dispersion of the plasmons is shown in Fig. 1.1(b) (red line), as a function of wavevector q.

The Drude model is a reasonable approximation to describe the dielectric response of metals like silver in the visible and gold for energies $\lesssim 2$ eV [37]. Above these energies, the electronic inter-band transitions in the material also contribute to the total response and a simple free electron model breaks down. Figure 1.2 shows the real and imaginary part of the dielectric function of gold. The value of the energy where $\varepsilon_m(\omega) = 0$ falls below the plasma frequency of a purely free electron metal because of interband transitions.

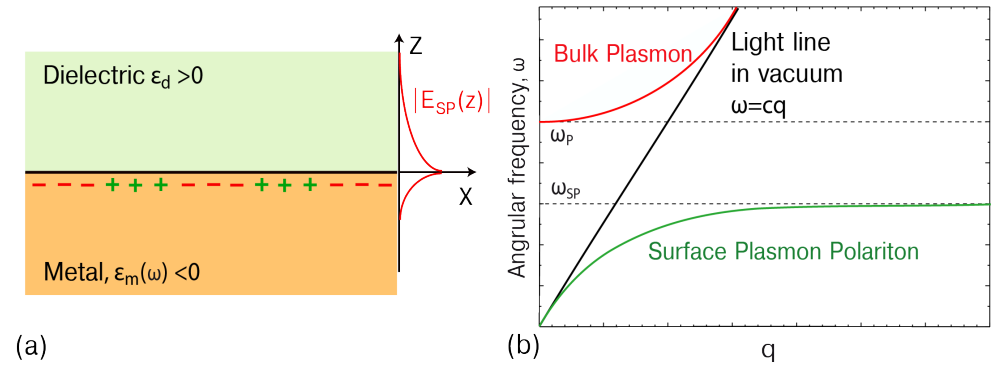

FIGURE 1.1: (a) Sketch of a surface plasmon supported by a semi-infinite metal-dielectric flat interface. The metal-dielectric interface can support propagating surface plasmons when the dielectric function of the metal is $\varepsilon_m(\omega)$ <0 and the dielectric is characterized by ε_d >0. The electric field induced by the surface plasmons decays exponentially in the direction normal to the interface plane at each side of the interface. (b) Bulk plasmon (red) and surface plasmon polariton (green) dispersion for a simple Drude metal. The dashed lines mark the bulk plasmon (ω_P) and surface plasmon (ω_{SP}) frequencies and the black line shows the dispersion line of light in vacuum. For the surface plasmon, $\varepsilon_d = 1$.

In the visible-near-infrared region, metals show negative values of the real part of the dielectric function, as shown in Fig. 1.2 for gold, as an example.

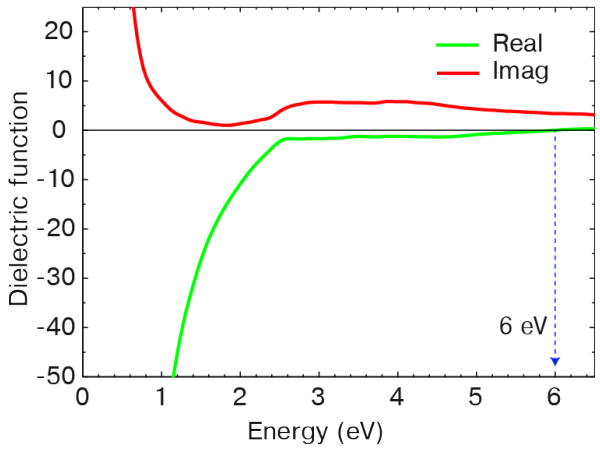

FIGURE 1.2: Real and imaginary part of the dielectric function of gold (Johnson and Christy [38]). The arrow marks the energy where Re[ε_m]=0.

Nonetheless, bulk plasmons cannot be excited by optical illumination and we focus next on surface plasmons. In the simple case of an infinite flat interface separating a metallic and a dielectric semi-infinite regions [as schematically shown in Fig. 1.1(a)], Surface Plasmon Polaritons (SPP) are obtained as solutions of the poles of the Fresnel reflection

r_p or transmission t_p coefficients given by

$$r_p = \frac{\varepsilon_m k_{1z} - \varepsilon_d k_{2z}}{\varepsilon_m k_{1z} + \varepsilon_d k_{2z}}; \qquad t_p = \frac{2\varepsilon_d k_{1z} k_2/k_1}{\varepsilon_m k_{1z} + \varepsilon_d k_{2z}}, \tag{1.6}$$

where k_{1z} and k_{2z} are the z components of the wavevectors k_1 and k_2 of the incident and transmitted plane-waves in the dielectric medium (characterized by ε_d) and in the metal respectively. The derivation of these equations is detailed in Appendix A.

The dispersion relationship of SPPs can thus be written as

$$\omega_{\mathrm{SPP}} = \sqrt{\frac{\varepsilon_m + \varepsilon_d}{\varepsilon_m \varepsilon_d}} cq. \tag{1.7}$$

For a metal characterized by the Drude model of Eq. (1.4), the dispersion of SPPs is shown in Fig. 1.1(b) (green line). For large values of q the SPPs asymptotically approach the value ω_{SP}, called surface plasmon frequency. In this range the metal dielectric interface satisfies the condition $\varepsilon_m(\omega) + \varepsilon_d = 0$, which gives, for a lossless Drude metal, the energy of the Surface Plasmons (SP), ω_{SP}, as:

$$\omega_{\mathrm{SP}}^2 = \frac{\omega_{\mathrm{P}}^2}{1 + \varepsilon_d}. \tag{1.8}$$

If the dielectric medium is vacuum, $\varepsilon_d = 1$, this equation simplifies to

$$\omega_{\mathrm{SP}} = \frac{\omega_{\mathrm{P}}}{\sqrt{2}}. \tag{1.9}$$

As can be seen in Fig. 1.1(b), surface plasmons appear thus at lower energy compared to the plasma energy of the metal.

SPPs cannot be coupled directly to an incoming plane-wave incident on the surface of a metal. In order to excite the SPPs, the momentum parallel to the substrate of the incoming photon should equal the momentum of the plasmon, but the latter is too large for this condition to be satisfied, as observed in Fig. 1.1. However the coupling can be achieved using a prism (Kretschmann configuration [39, 40]) or gratings [41–43] to provide additional momentum to the incident light.

Going beyond semi-infinite substrates, surface plasmon resonances in closed surfaces such as in metallic nanostructures, acquire a localized nature and are known as Localized Surface Plasmons Polaritons (LSPPs). The energy of LSPPs depends strongly on the material properties, the size, shape as well as on the dielectric surroundings

of the nanostructure and the coupling with neighbouring structures. Gold and silver nanostructures have very well defined LSPPs in the visible and near-infrared ranges of the spectrum, which can be excited by direct illumination, thanks to the momentum matching between LSPPs and the incident light.

LSPPs are exploited in various nanophotonic applications. For example, the dependence of the LSPP energy on the dielectric environment is commonly used to detect biological molecules and in chemical sensing [44–46]. The enhanced near-field and strong scattering property of metallic particles at LSPR is also used to enhance the emission from minute amounts of molecules in spectroscopic studies [47]. Enhanced light-matter interaction mediated by metallic particles is also explored to increase the performance of solar cells [48, 49]. In medicine, as a last example, surface plasmon resonances in gold nanostructures are used in diagnostics and treatment of cancer [50, 51].

The concept of Localized Surface Plasmon Resonance (LSPR) can be understood, for example, by describing the interaction of a homogeneous isotropic metallic spheroid with the electromagnetic radiation, when the size s of the particle is much smaller than the wavelength of the radiation, $s \ll \lambda$. The electric dipole moment $\mathbf{p}$ of a spheroidal particle of radii a', b' and c' and dielectric function ε_m placed in a homogeneous medium ε_d and subjected to a uniform electric field $\mathbf{E}_0$ is [52]:

$$\mathbf{p} = \varepsilon_0 \varepsilon_d \alpha \mathbf{E}_0, \tag{1.10}$$

where the complex polarizability of the particle, α is given by

$$\alpha = 4\pi a' b' c' \, \frac{\varepsilon_m - \varepsilon_d}{3\varepsilon_d + 3L(\varepsilon_m - \varepsilon_d)}, \tag{1.11}$$

L is a geometrical depolarization factor that depends on the shape (values of a', b', c') and the polarization direction, which has been assumed to be parallel to one of the axis. In the case of a sphere of radius a (L=1/3), Eq. (1.11) becomes

$$\alpha = 4\pi a^3 \frac{\varepsilon_m - \varepsilon_d}{\varepsilon_m + 2\varepsilon_d}. \tag{1.12}$$

The polarizability of the spherical particle attains a maximum value (resonance) under the condition $\mathrm{Re}[\varepsilon_m(\omega)] = -2\varepsilon_d$, provided that the imaginary part of the dielectric function is small. This condition corresponds to the LSPR of the particle. At resonance, these nanoparticles can be considered as an oscillating electric dipole, which shows antenna

properties like strong resonant absorption and scattering of electromagnetic radiation. The properties of metallic nanostructures as optical nanoantennas have been widely explored for various applications like field enhanced spectroscopy and plasmonic sensing [53, 54].

The scattering, σ_{scat}, and absorption, σ_{abs}, cross sections of a nanoparticle can be expressed in terms of the resonant polarisation α, given in the electrostatic limit by

$$\begin{aligned} \sigma_{scat} = \frac{k_d^4}{6\pi}|\alpha|^2 &= \frac{8\pi}{3} k_d^4 a^6 \left|\frac{\varepsilon_m - \varepsilon_d}{\varepsilon_m + 2\varepsilon_d}\right|^2, \\ \sigma_{abs} = k_d \,\mathrm{Im}[\alpha] &= 4\pi k_d a^3 \mathrm{Im}\left[\frac{\varepsilon_m - \varepsilon_d}{\varepsilon_m + 2\varepsilon_d}\right], \end{aligned} \tag{1.13}$$

where $k_d = \omega\sqrt{\varepsilon_d}/c$ is the wave number of the incoming light in the embedding dielectric medium. For low enough losses, the scattering and absorption cross sections show clear resonances at the localized resonance condition of the particle, $\mathrm{Re}[\varepsilon_m(\omega)] = -2\varepsilon_d$. The extinction cross section of a particle is given by the sum of the absorption and scattering cross sections. Moreover, at resonance, these particles show strong enhancement of the electric field in their vicinity. It is worthwhile to notice from Eq. (1.13) that since the scattering and absorption scales with a^6 and a^3 respectively, the scattering from sufficiently small particles is much smaller than the absorption.

As an example, in Fig. 1.3(a) we show the scattering and absorption of a silver sphere of radius 20 nm calculated by solving Maxwell's equations with appropriate boundary conditions. At $\lambda = 360$ nm the particle shows enhanced scattering and absorption resulting from the dipolar electromagnetic resonance. The electric near-field E calculated around the particle at $\lambda = 360$ nm and normalized to the incident amplitude $\mathrm{E_{inc}}$ is displayed in Fig. 1.3(b). It shows the expected dipolar field distribution and a strong local field enhancement $\mathrm{E/E_{inc}}$ near the particle. The spectral position of this resonance can be strongly shifted by changing the shape (depolarization factor L), the size of the particle or the surrounding medium.

In the case of large particles and nanostructures with complex geometry, however, simple analytical solutions of the plasmonic response are not possible. Even for a simple shape, the polarizability given by Eq. (1.11) breaks down as the size of the particle grows because it does not consider retardation and radiation effects [55, 56]. For large and/or complex structures we can use numerical computational methods, to get the full electrodynamical response by solving Maxwell's equations to obtain the fields in a system.

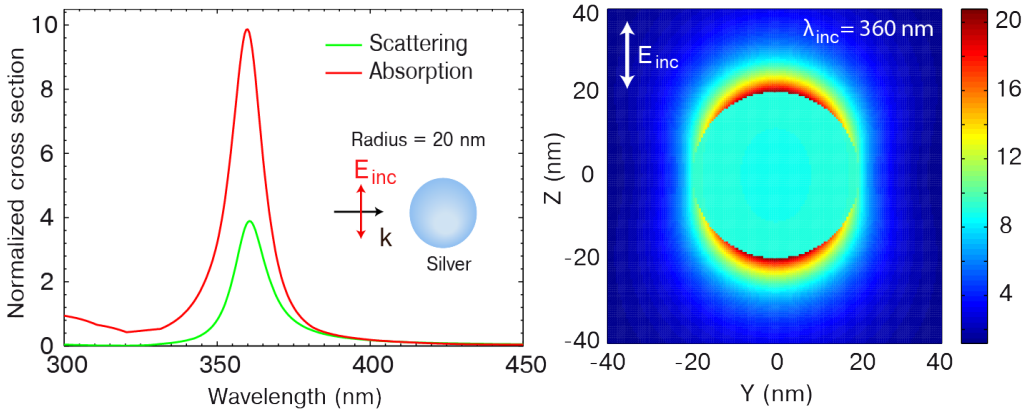

FIGURE 1.3: Full electrodynamic response of a silver sphere of radius 20 nm. (a) Scattering and absorption cross sections of the particle normalized to the surface area of the sphere showing dipolar resonance peak at λ= 360 nm, for a linearly polarized plane-wave illumination as shown in the inset. (b) Amplitude map of the electric near-field enhancement around the particle at the dipolar resonance (λ = 360 nm), showing a dipolar field distribution.

1.1.1. Plasmonic modes in metals beyond gold and silver

Gold and silver are the metals most frequently used for plasmonic studies due to relatively moderate losses that lead to well defined resonances. Their small chemical reactivity and well developed fabrication methods are additional advantages [57, 58]. Nevertheless, several other metals and metallic alloys show plasmonic response at optical frequencies [23, 24]. Even though many of these materials exhibit large losses, their optical properties are promising for various plasmonic applications. For example the plasmonic response of nickel and cobalt nanodisks has been studied for magneto-plasmonic applications [27, 59]. Hot electron generation in several metals, including aluminium, copper and metal oxides are also studied for catalytic and photovoltaic applications [60]. The optical properties of platinum have been equally explored for nano catalysis applications [25, 26].

In this thesis we have focused in Palladium as an alternative plasmonic metal of special interest. The catalytic properties of palladium make it an important material in research and industry [62, 63].

Figure 1.4 displays the dielectric function of palladium, which shows Re[$\varepsilon(\omega_P)$]=0 at 7.78 eV. Due to the negative values of the real part of the dielectric function below 7.78 eV, SPPs in Pd appear in the ultraviolet. At large energy, Pd shows large plasmonic losses compared to gold and silver, which results in more strongly damped plasmonic resonances. Figure 1.5 shows the extinction spectra of nanospheres of palladium of

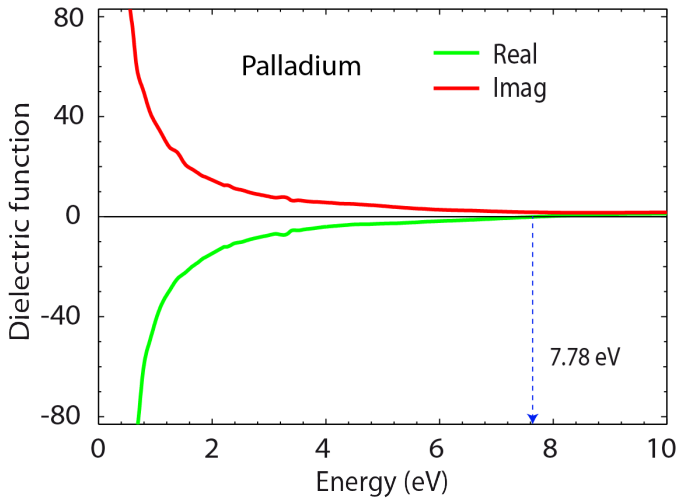

FIGURE 1.4: Real and imaginary parts of the dielectric function of palladium. The data are experimental values taken from Ref [61]. The real part of the dielectric function of Pd becomes zero at 7.78 eV, and shows negative values below this energy.

radius 75 nm compared with gold and silver spheres of the same size. The size of these particles are too large to be described using the quasistatic approach, and therefore full electrodynamical calculations are performed using the Boundary Element Method [64, 65]. While gold and silver show well defined resonances, the palladium nanosphere has a very broad and damped resonance.

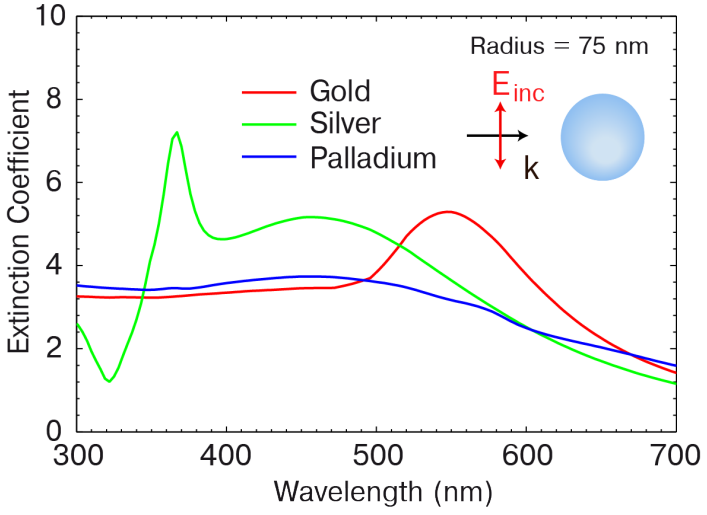

FIGURE 1.5: Extinction spectra of individual nanospheres of gold, silver and palladium of radius 75 nm, for linearly polarized plane-waves incident as schematically shown in the inset. Well defined localized resonances are shown for gold (λ=547 nm) and silver (λ=455 nm and λ=367 nm). The resonance of the Pd sphere (λ=457 nm) is significantly more damped.

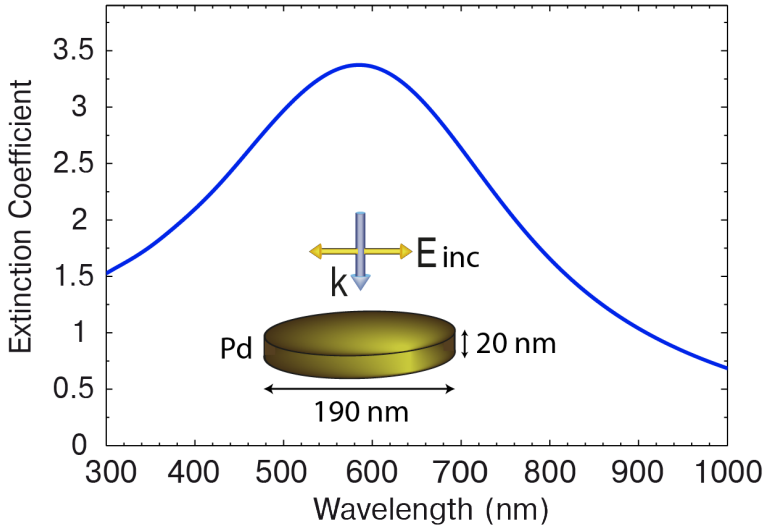

FIGURE 1.6: Extinction spectra of a palladium nanodisk of 190 nm diameter and 20 nm thickness surrounded by vacuum, when illuminated with a linearly polarized plane-wave incident from the top as schematically shown in the inset. The spectra shows a clearly-defined localized plasmonic resonance at $\lambda = 585$ nm.

Despite these large losses, well defined plasmonic resonances can be obtained for Pd structures in the visible and near-infrared region by carefully designing the geometry. Figure 1.6 shows the localized surface plasmon resonance in a Pd nanodisk of 190 nm radius and 20 nm thickness placed in vacuum. A clear dipolar resonance at λ=585 nm that extends to the ultraviolet is found.

An interesting property of palladium is that it can dissociate molecular hydrogen and incorporate the hydrogen atoms to the lattice to form palladium hydride (PdH). This structural modification results in an appreciable change in the dielectric response of the metal and consequently in the plasmonic response as well. The amount of hydrogen absorbed in the metal and the structural modification in the material can be thus traced by following the changes in the LSPR response of Pd nanostructures exposed to hydrogen. The modification of the optical response of palladium by the presence of hydrogen is of interest in hydrogen sensing and storage applications[66–68].

A detailed discussion of the hydrogen sensing properties of Pd is presented in Chapter 2. We first identify a suitable system for performing LSPR sensing of hydrogen in Pd. We employ a theoretical model that takes into account the atomic scale changes, structural changes as well as morphological aspects that contribute to the optical response of metal hydride (PdH) nanostructures. For this purpose we combine ab-initio quantum

mechanical calculations with classical electrodynamics to study the optical response of Pd nanostructures modified by the presence of hydrogen.

1.2. Optical response of materials in the infrared

Several materials including molecules and molecular groups show vibrational excitations in the infrared range of the spectrum. The study of these molecular fingerprints are important in biological and chemical sensing as well as in the study of the physical and chemical properties of molecular samples. Some effective tools to study small amounts of these materials are field enhanced spectroscopic techniques like surface-enhanced Raman scattering (SERS) and surface-enhanced infrared absorption (SEIRA). In SERS, the Raman signal from molecules adsorbed in rough metal surfaces or near metallic particles can be detected due to the enhanced scattering provided by the strong near-field at the metal surface [69–71]. Enhancements of many order of magnitudes and detection of single molecules are possible using this technique [53, 72, 73]. In the case of SEIRA, the vibrational signal of the molecular groups is directly detectable in transmission mode due to the direct interaction with the antenna resonance [74, 75].

In order to get an enhanced SEIRA signal from small amounts of sample, it is important to design antennas resonant in the infrared that couple effectively to, for example, vibrational excitations in the sample. Instead of simply considering large metallic system, we are interested here in other low-loss dielectric materials such as silicon that also lead to a strong response to infrared radiation. The interaction of pure dielectrics with infrared radiation is mainly mediated by the polarisation of the bound charges of the atoms. Purely non-magnetic dielectric particles of high refractive index show strong electric and magnetic response for infrared light, as a result of geometric resonances in the particle [28]. Interesting field enhancement and scattering properties arise for this type of nanomaterials as discussed in Section 1.2.1 and in Chapter 3.

Polar crystals, on the other hand, show sharp electromagnetic resonances at well-defined wavelengths that arise from lattice vibrations in the mid-infrared. As a consequence, small particles of polar materials can exhibit large field enhancement and strong scattering [31, 32]. We discuss the optical properties of polar materials in Subsection 1.2.2, taking silicon carbide as an example.

Another class of materials showing strong response to infrared radiation are semiconductors. The interaction of light with semiconductors, is mediated by the excitation of

charge carries in the form of electron-holes pairs. A relatively large concentration of free carriers in semiconductors can support plasmons in the same manner as we have already described in the case of metals. These plasmons can be also tuned by controlling the carrier concentrations via doping [76, 77]. As the achievable carrier concentration is low compared to metals, the plasmon resonances in semiconductors fall at low energies.

We devote this section to discuss the optical properties of dielectric particles and polar crystals. A short discussion of the plasmonic response of doped semiconductors and large metallic structures is also included in the end of the section for completeness.

1.2.1. Optical response of dielectric particles

Dielectric materials have been used to obtain strong optical response with use of structures of micron sizes such as toroids, micro-pillars or photonic crystals [13]. Here, we are interested in dielectric nanoparticles of dimensions of hundreds of nanometers that can be used to enhance and control the emission from single molecules and quantum dots [78, 79] in nanophotonics. These structures can be complementary to plasmonic nanoantennas in many applications, with the added advantage of low ohmic losses.

Several groups recently demonstrated that dielectric antennas present not only electric resonances, but interestingly also magnetic modes [28, 80–82]. The electric modes of these particles are associated with the depolarizing field and the magnetic resonances result from the circular current loops. Magnetic dipole resonances in dielectric nanospheres have been experimentally demonstrated for silicon nanoparticles [83]. Silicon has a high dielectric function $\varepsilon \approx 12.25$ in the infrared region with negligible losses (very small imaginary part of dielectric function). The coupling of electric and magnetic single photon emitters (dipole-like) with electric and magnetic modes of a dielectric antenna can be also used to control photon emission [30, 84]. The coupling with dipolar magnetic transitions in materials like lanthanide ions [85–87] has been studied, for example, to enhance the dipolar magnetic transitions. The simultaneous coupling of emitters with the electric and magnetic modes can help to control the directionality of scattering, as theoretically shown [29, 88, 89] and experimentally demonstrated in the microwave [90] and visible [80, 91] range of the spectrum. The interplay of electric and magnetic resonances and the resultant anisotropic scattering can be also a platform to study optical forces in dielectric particles [29, 89, 92, 93].

This subsection briefly reviews the scattering properties and the near-field distribution of a single silicon sphere of radius 150 nm in the visible and near-infrared wavelengths. The

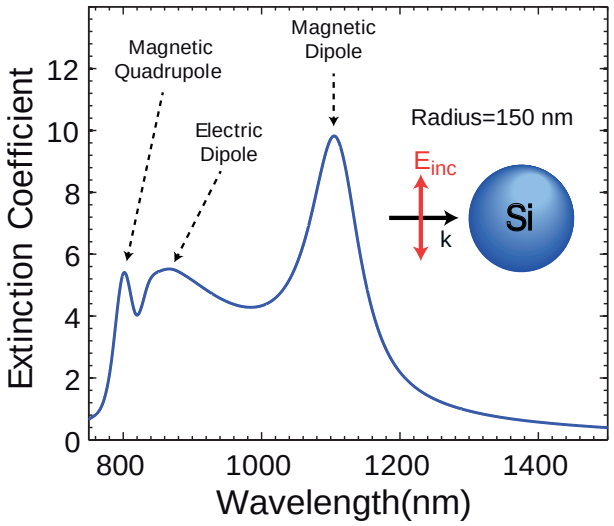

FIGURE 1.7: Extinction coefficient calculated for a silicon sphere of radius 150 nm. The peaks at $\lambda = 1108$ nm, 864 nm and 800 nm correspond to magnetic dipolar, electric dipolar and magnetic quadrupolar resonances respectively.

extinction spectrum in Fig. 1.7 shows the well-defined magnetic dipole, electric dipole and magnetic quadrupole resonances at $\lambda = 1108$ nm, 864 nm and 800 nm respectively. The magnetic dipolar peak is relatively strong and the electric dipolar peak extends over a wide spectral range. The magnetic quadrupolar peak is significantly narrower. Surprisingly, the order of appearance of the modes in the spectrum is reversed with respect to the standard case of typical metallic spheres, being the magnetic dipolar resonance the lowest energy excitation. Figure 1.8 shows the electric and magnetic field amplitude enhancement around the sphere calculated at the electric dipolar resonance ($\lambda = 864$ nm) and at the magnetic dipolar resonance ($\lambda = 1108$ nm). The enhancement corresponds to the electric field amplitude normalized to the incident amplitude. The incident field is polarized along y and propagate along the z direction. The field maps are calculated in the $x - y$ plane perpendicular to the incident radiation and passing through the center of the sphere. In the case of the electric dipolar resonance the incident electric field creates an electric displacement current parallel to the y axis [Fig. 1.8(a)], which is equivalent to an electric dipole. This electric dipole induces a loop of magnetic field around it [Fig. 1.8(b)]. In contrast, the dipolar magnetic resonance is characterized by a circulating loop of electric field [Fig. 1.8(c)] inside the sphere. This current loop induces the magnetic dipole oscillating along the x direction shown in Fig. 1.8(d).

From the field distribution shown in Fig. 1.8, it can be observed that the electric field enhancement is stronger outside the particle, while the magnetic field is significantly

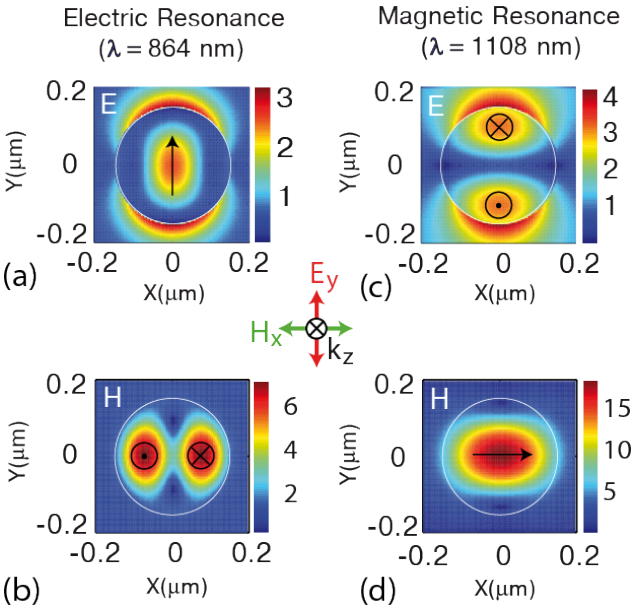

FIGURE 1.8: The electric and magnetic near-field amplitude enhancement calculated at the electric (λ_{inc}=864 nm) and the magnetic (λ_{inc}=1108 nm) resonances in a silicon sphere of radius 150 nm. The fields are calculated in a plane normal to the incident k and contains the center of the spheres. At the electric resonance, the field maps show the dipolar distribution of electric field (a) and the resultant induced circular magnetic field distribution (b). At the magnetic resonance, the field maps show the dipolar distribution of magnetic field (d) and the resultant induced circular electric field distribution (c).

stronger inside the particle than outside. In order to explore the possibilities of the resonant magnetic field of these particles in applications like probing of magnetic transitions, it is often desirable to achieve strong magnetic field enhancement outside the particle. A possibility to achieve this aim is to modify the antenna morphology or to couple two or more resonant structures.

In Chapter 3 we present our investigation of the scattering as well as of the electric and magnetic field enhancement properties for a dielectric dimer antenna made of two identical silicon spheres. The coupling of the electric and magnetic dipoles induced in the two spheres makes it possible to strongly modify the field distribution presented by the individual spheres and strengthen the electric and magnetic fields outside the particles. We use the incident polarization as a means to control the electric and magnetic coupling between the particles. Furthermore, we develop and use an analytical model, based on electric-electric, magnetic-magnetic and electric-magnetic interactions in the dimer, to better understand the resonance couplings in the system. We thus identify two coupling regimes for the dimer, based on the strength of the interaction between the spheres, as a function of the dimer gap distance.

1.2.2. Optical response of polar materials

Polar crystals are a class of materials showing very interesting optical properties at infrared wavelengths. Polar materials are characterized by a charge distribution that can give locally non-zero dipole moments which can couple with an electromagnetic field. A strong response is induced when light couples resonantly with a vibrational mode of the crystal lattice leading to collective ionic oscillations called phononic resonances. Silicon carbide is a typical example of a phononic material that shows a sharp and well-defined phononic response [32, 94].

The relative dielectric function for a simple polar material can be expressed as

$$\varepsilon_{ph} = \varepsilon_{\infty} \frac{\omega_{\mathrm{LO}}^2 - \omega^2 - i\gamma\omega}{\omega_{\mathrm{TO}}^2 - \omega^2 - i\gamma\omega}, \tag{1.14}$$

where ω is the incident angular frequency, ω_{LO} and ω_{TO} are respectively the angular frequencies of the longitudinal optical (LO) and the transverse optical (TO) vibrational modes in the crystal, γ is the damping constant [95, 96] and ε_{∞} is the background dielectric function of the material.

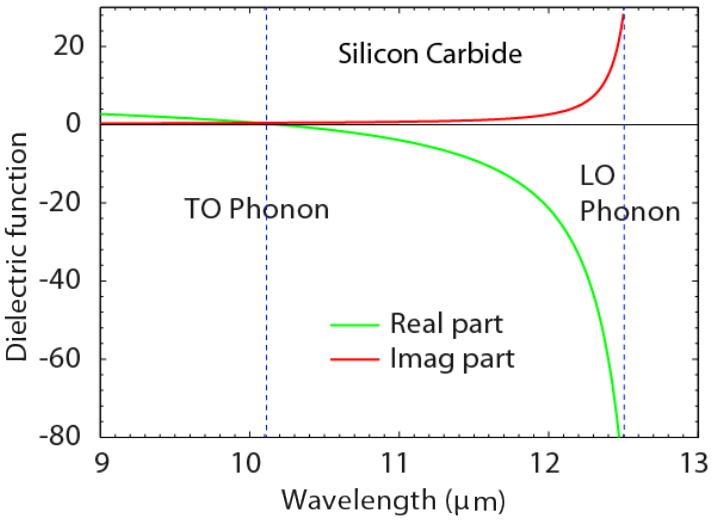

FIGURE 1.9: Real and imaginary parts of the dielectric function of SiC in the infrared. The material shows negative real part of dielectric function between longitudinal (LO) and transverse (TO) phonon frequencies, marked by dashed lines. Data taken from Ref [61].

The real and imaginary parts of the dielectric function for SiC is shown in Fig. 1.9. Notably, between the frequencies ω_{TO} and ω_{LO}, corresponding to the wavelength around 11 μm, the value of ε_{ph} is negative. Thus, surface phononic modes can be excited at

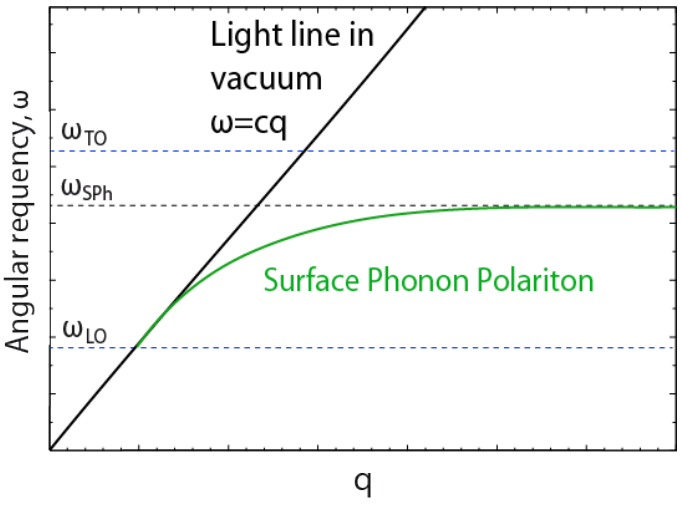

FIGURE 1.10: Dispersion relation of Surface Phonon Polaritons in the interface between a polar material and vacuum. The surface phonon modes exist in the frequency range between the transverse, ω_{TO}, and longitudinal, ω_{LO}, optical phonon frequencies. ω_{SPh} is the surface phonon frequency. The dispersion line of light in vacuum is also shown.

the interface with a dielectric of positive dielectric function, in a similar manner to the plasmonic response of metals in the visible.

Both propagating [94] Surface Phonon Polaritons (SPhPs) in flat interfaces and gratings [97] and Localized Surface Phonon Polaritons (LSPhPs) in phononic antennas [31, 98, 99] can be coupled to electromagnetic IR radiation in polar materials, such as SiC.

Substituting ε_{ph} to Eq. (1.7) gives the dispersion relation for SPhPs in a polar material. Figure 1.10 sketches the result for a typical polar material. It can be noticed that the dispersion relation of the SPhPs is similar to that of SPPs shown in Fig. 1.1. Nonetheless, notice that SPhP is only present between ω_{TO} and ω_{LO}, while for metals there is no well-defined frequency below which no surface plasmons are possible.

In the absence of damping, the asymptote at large wavevectors with vacuum as dielectric medium gives the surface phonon frequency

$$\omega_{\mathrm{SPh}} = \sqrt{\frac{\omega_{\mathrm{TO}}^2 + \varepsilon_\infty \omega_{\mathrm{LO}}^2}{1 + \varepsilon_\infty}}. \tag{1.15}$$

The LSPhPs supported by nanostructures of polar materials also behaves similar in the infrared to the LSPPs in metal nanoparticles at optical frequencies [32]. LSPhPs depend on the properties of the polar material, the size and shape of the structures and the interactions with the surrounding medium and other scattering objects [100]. As for metallic

structures, phononic antennas can be thus suitable for different nanophotonic applications. For example, the field enhancement induced near phononic antennas made of SiC nanostructures occurs at frequencies suitable for surface enhanced infrared absorption (SEIRA) [74]. In SEIRA, the signature of vibrational resonances of the molecular groups can be enhanced by coupling with the fields produced at the phononic antenna, lowering the detection limit of the amount of molecular groups [74]. The optical response of small particles of phononic materials are therefore explored for nanophotonic applications like field enhanced spectroscopy [101] and near-field microscopy [32, 102].

Here we briefely discuss our studies on the optical response of SiC disks for infrared radiation [36]. We present the study of the response of disks of different dimensions, with size ranging from 400 nm to 600 nm and thickness ranging from 50 nm to 100 nm to understand the dependence of antenna resonances on the geometrical parameters of the disk. The far-field response and near-field enhancement properties of the disks suspended in vacuum are studied for plane-wave illumination in the wavelength range of 9.5 μm to 12.5 μm using the Boundary Element Method [64, 65] to solve the Maxwell's equations. The near-field response of the disk is also shown for further understanding of the spectral peaks and the associated modes excited. For simplicity, in the calculations, the disks are approximated by ellipsoids. SiC is used here as a good example of polar material.

1.2.2.1. Infrared response of SiC disks

We analyze in this section the typical response of a phononic particle as an example of localized response in the IR. First of all we show the far-field response of the disks as a function of the disk size (radius). Figure 1.11 shows the far-field response of disks of various sizes and thicknesses for an oblique illumination using a p-polarized plane-wave as schematically shown in the inset.

Figure 1.11(a) shows the extinction spectra of disks of thickness 50 nm for radii, R = 400 nm (green), 500 nm (blue) and 600 nm (red). The extinction spectra presents well defined peaks as a result of the resonant excitation of localized surface phonons in the disk. The stronger peak in the spectra corresponds to the excitation of a dipolar localized surface phonon mode in the disk. At the dipolar resonance, the disk attains an effective electric dipole moment because of the polarisation of the positive and negative charges at radially opposite ends of the disk.

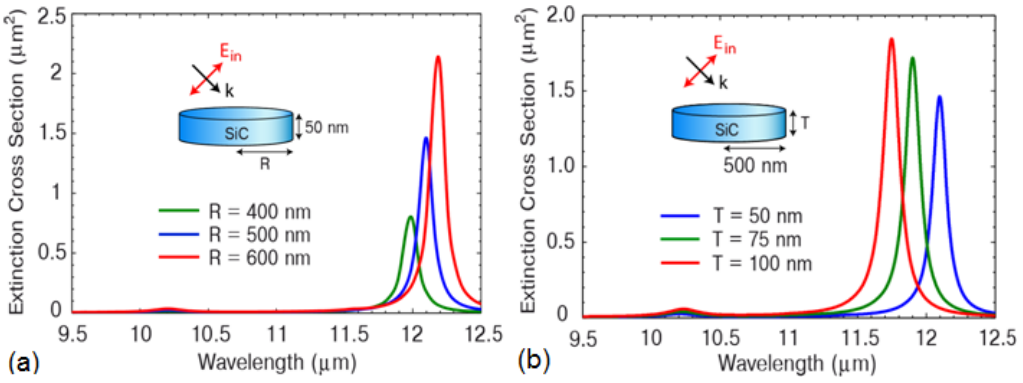

FIGURE 1.11: Far-field response of SiC disks of various sizes and thickness. (a) Extinction spectra of a disk of thickness 50 nm calculated for various disk radii, R = 400 nm (green), 500 nm (blue) and 600 nm (red). (b) Extinction spectra of a disk of radius 500 nm calculated for various thicknesses, T = 50 nm (blue), 75 nm (green) and 100 nm (red).

Two main changes are observed in the spectra as the radius of the disk is increased, namely the redshifting of the dipolar resonance and the increase in the strength of the extinction at resonance. A disk of 50 nm thickness and 400 nm radius presents a dipolar resonance peak at λ=11.99 μm. As the radius is increased, the position of the dipolar resonance is redshifted, and for a radius of 600 nm it appears at λ=12.19 μm. The redshift of the peak results from the lowering of the energy of the phononic oscillator as the radius of the disk is increased, similar to the evolution of localized plasmonic resonances with particle size. The larger the radius of the disk, the larger is the separation between the positive and negative charges in the disk, thus lowering the energy of the harmonic oscillator of charges formed. For particles much smaller than the wavelength of the incident radiation, the absorption and the scattering cross sections are proportional to the volume and to the square of the volume of the particle, respectively. In the simplest case, the absorption and scattering from the disks can be understood in terms of the polarizability of an ellipsoidal particle parallel to one of its principal axes, as given by Eq. (1.11). Since the extinction cross section of a particle is given by the sum of the absorption and scattering cross sections, it is clear from Eq. (1.13) that the strength of extinction increases with the size of the particle. This explains the observed increase in the extinction cross section of the SiC disk with increase in size.

Another parameter of interest in the study of SiC disk nanoantennas is the dependence of the antenna resonance on the thickness of the disk. Therefore in the next step, we study the far-field response of a disk of given radius for various thicknesses. Figure 1.11(b) shows the extinction spectra obtained for disks of radius 500 nm and thickness of 50 nm (blue), 75 nm (green) and 100 nm (red) respectively. Two main changes are observed in

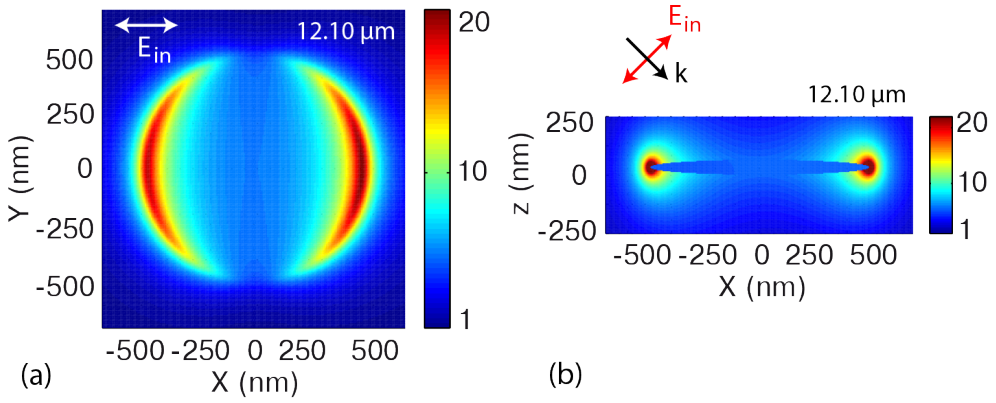

FIGURE 1.12: Maps of the electric near-field amplitude enhancement around a SiC disk of radius 500 nm and thickness 50 nm, calculated at the phononic dipolar resonance ($\lambda = 12.10\,\mu$m). The top (a) and side cross section (b) views of the field distribution reveals the dipolar nature of the phononic resonance and also provides information on the enhancement and localization of the electric near-field.

the spectra as the thickness of the disks is decreased, namely the decrease in the strength of extinction peaks and redshift of the antenna resonance. The decrease in the strength of extinction at antenna resonances goes in line with the increased extinction for larger disks discussed earlier in this section. Since the scattering scales with the square of the volume, the thinner the disk is, the weaker the extinction.

A disk of 100 nm thickness and 500 nm radius shows a dipolar antenna resonance at λ=11.75 μm. As the thickness of the disk is decreased, the position of the dipolar resonance is redshifted and reaches λ=12.10 μm for a thickness of 50 nm. This dependence of the spectral position of the antenna response on the thickness of the disk is governed by the interaction of the surface modes at the surface of the antenna. This surface mode interaction can be understood as the Coulomb interaction between the charges induced at the top and bottom surfaces of the disk. For very small thicknesses, a coupled resonance is generated with charges of same sign at the top and bottom surfaces. This coupled resonance is analogous to the symmetric solutions of molecular orbitals in quantum chemistry [103]. The energy of this bonding mode depends on the separation between the induced charges at each surface of the disk. Therefore the spectral position of the phononic resonance depends strongly on the thickness of the disk. The smaller the separation between the top and the bottom surfaces, the smaller is the energy of the bonding mode. This is the reason why the antenna resonance is redshifted as the thickness of the disk is decreased. In the following, the investigations on the field enhancement properties of phononic antennas are presented.

Figure 1.12 shows the amplitude enhancement of the electric near-field distribution around a SiC disk of radius 500 nm and thickness 50 nm at an illuminating wavelength of 12.10 μm, which corresponds to the dipolar phononic resonance of the disk as shown in Fig. 1.11. We use the same illumination as previously, a p-polarized plane-wave obliquely incident, as schematically shown in the figure. The top view of the near-field map [Fig. 1.12(a)] and the side view [Fig. 1.12(b)] clearly shows the dipolar field distribution around the antenna, due to the dipolar antenna resonance. The near-field distribution also reveals that the electric field enhancement is maximum close to the edges of the nanodisk, in the direction of the incident electric field. This enables us to predict that the signal from molecular groups to be studied (the sample) can be efficiently enhanced if it is located near the edge of the disk, along the x axis.

There are several conventional techniques to study vibrational spectroscopy of molecules. Most of these techniques are limited when the number of sample molecules is very small or when the demand of specificity is high. Progress in nanophotonics and plasmonic has revolutionized the field of vibrational spectroscopy by reducing the detection limit of sample molecules and by increasing the sensitivity and specificity. If a molecular group is located in an area of high field intensity, it is possible to enhance the intensity of the scattered field substantially, which is the working principle of surface enhanced scattering techniques such as Surface Enhanced Raman Scattering (SERS) [70, 71, 104] and Surface Enhanced Infrared Absorption spectroscopy (SEIRA) [74]. In both cases, the signal from a molecular group is resonantly enhanced several orders of magnitude by placing the molecule in the area of enhanced field. This is realized by careful design of nanoantennas to provide sufficient field enhancement and reasonable scattering intensity [105].

The results presented in this section show that nanoantennas of phononic materials present well defined resonances that can be tuned by varying the dimensions of the antenna. Furthermore, we also show that with effective nanoantenna design, we can get enhanced scattering and near-field enhancement in phononic nanoantennas, which is crucial for optimizing applications like field enhanced spectroscopy and sensing.

1.2.3. Optical response of doped semiconductors and large metallic structures

The density of charge carriers in a semiconductor can be controlled by intrinsic doping. For sufficiently high doping, semiconductor nanostructures can thus support plasmonic

excitations at energies that depend on the square root of the carrier concentration, as shown in Eq. (1.3). Micron-sized structures of doped semiconductors can support fundamental antenna resonances in the infrared and THz wavelengths [76, 106, 107], which have been explored for plasmonic sensing and field enhanced spectroscopy [77, 108].

On the other hand, plasmonic resonances of metallic nanostructures generally redshift with increasing size. For sufficiently large sizes, metallic structures can also support fundamental antenna resonances at infrared wavelengths [109]. The field enhancement and antenna properties of these metallic structures, resonant also in the infrared, have also been explored for field enhanced spectroscopy [74].

Doped semiconductor nanostructures and large metallic structures can be thus used as alternatives to obtain resonances in the infrared. Their optical properties can be approximately described using the Drude model.

1.3. Optical response of 2D electron gases in the terahertz

The terahertz (THz) spectral range includes wavelengths from the far-infrared to the microwave in the electromagnetic spectrum. At these frequencies, a variety of substances such as gases, biomolecules, organic substances and polymers show spectroscopic fingerprints, arising from the rotational and vibration excitations in the materials [110, 111]. The electromagnetic sensing and spectroscopy of materials at THz frequencies has significant importance in chemical, biomedical, as well as in other industrial applications [112–115]. THz spectroscopy techniques are used, among others, for detection and identification of explosive materials and drugs [116, 117]. Another important area where THz radiation is useful is in optoelectronics and electromagnetic communication at small length scales [118, 119]. In these applications, it is very important to achieve efficient coupling of THz radiation with small-scale devices [118].

The interaction of the THz radiation with different substances can be enhanced by a plasmonic antenna helping to increase the sensing capability [77, 120] and to improve the spectroscopic signature [121] of different substances. Devices based on optical antennas can also be very compact, with sub-diffraction dimensions, which can be particularly interesting for long wavelength applications. Therefore plasmonic antennas can thus be useful for applications at THz frequencies [122, 123]. Excitation of plasmonic resonances

at THz frequencies has been demonstrated, for example using doped semiconductors [77, 124], as mentioned in the previous section.

An interesting novel material that shows resonant coupling with THz radiation is graphene. Graphene is a monolayer of carbon atoms in a honeycomb configuration showing attractive electronic, mechanical and optical properties. [125–127]. The main reason behind the electronic and optical properties of graphene is the electronic structure of the two dimensional (2D) Dirac electron gas in the monolayer. This 2D electron system supports collective plasmonic oscillations (Dirac plasmons) [33], which occur in the far-infrared and THz range of the spectrum.

The dispersion relationship of surface plasmons in an interface separating two media can be obtained from the poles of the Fresnel reflection coefficients of the interface. The Fresnel reflection coefficient for an infinitely plane surface carrying a conductivity σ can be derived by applying the electromagnetic boundary conditions at the interface (see Appendix A). For p-polarized plane-wave of angular frequency ω, the reflection coefficient can be written as

$$r_p = \frac{\varepsilon_2 k_{1z} - \varepsilon_1 k_{2z} + (\sigma/(\varepsilon_0\omega))k_{1z}k_{2z}}{\varepsilon_2 k_{1z} + \varepsilon_1 k_{2z} + (\sigma/(\varepsilon_0\omega))k_{1z}k_{2z}}, \tag{1.16}$$

where ε_1 and ε_2 are the dielectric functions at each side of the graphene layer and k_1 and k_2 are the corresponding wavevectors. The plane-wave is incident from medium 1. The components of the wavevectors normal to the interface in the two media can be written as $k_{z1} = \sqrt{\varepsilon_1 k^2 - q^2}$ and $k_{z2} = \sqrt{\varepsilon_2 k^2 - q^2}$, where q is the component of the wavevector parallel to the interface and wave number $k = \omega/c$, c being the velocity of light in vacuum. q is preserved at both sides of the interface. The in-plane conductivity of 2D materials can be calculated within different approaches. One of the possibilities is to use many body theory to express the conductivity as detailed in Chapter 4.

An additional advantage of graphene is the possibility to change the Fermi energy, E_F, by intrinsic doping or via applying an external electric bias [33]. This allows for the spectral tuning of the plasmonic response [34, 35].

The surface plasmon dispersion can be obtained from the pole of the reflection coefficient in Eq. (1.16). Using the approximation $q \gg k$ the dispersion relationship for the surface plasmons at the interface can be obtained as [33]:

$$q_{SP} \approx \frac{i\omega\varepsilon_0(\varepsilon_2 + \varepsilon_1)}{\sigma}, \tag{1.17}$$

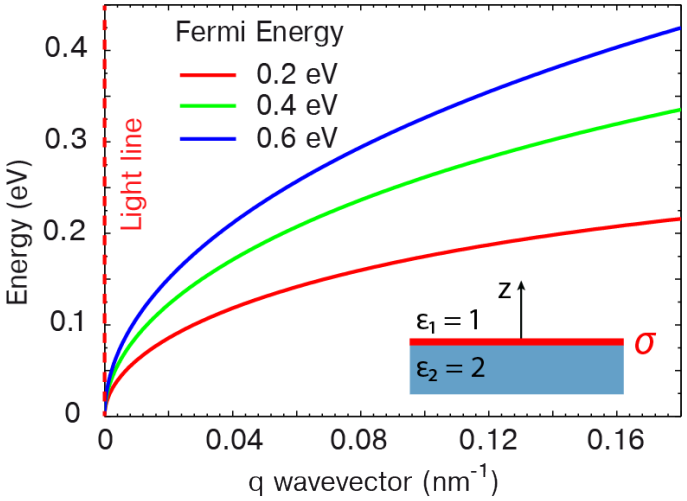

FIGURE 1.13: Dispersion of surface plasmons in graphene deposited on a substrate of dielectric constant $\varepsilon_2 = 2$, with vacuum as surrounding medium, for Fermi energies varying from 0.2 eV to 0.6 eV, obtained from Eq. (1.17) with use of many-body calculations of the graphene conductivity σ. The red dashed line shows the dispersion of light in vacuum.

where q_{SP} is the wavevector of the surface plasmon parallel to the interface. The dispersion relationship calculated for graphene deposited on a substrate of dielectric constant $\varepsilon_2 = 2$ can be observed in Fig. 1.13 for different Fermi energies, $E_F = 0.2$ eV, 0.4 eV and 0.6 eV.

The values of q_{SP} in Fig. 1.13 are very large compared with the wavelength of the photon in vacuum at these frequencies. For example, at far-infrared wavelengths, graphene supports surface plasmons with wavelengths of a few hundreds of nanometers, dramatically smaller than the wavelength of incident light. These plasmons are very strongly confined in the direction perpendicular to the sample and are expected to propagate over long distances, for ideal systems [33].

Graphene is a canonical material supporting two-dimensional plasmons at THz frequencies. Topological insulators are also interesting alternative materials with strong response to THz radiation. A 2D electron gas that naturally appears at the surface of three-dimensional topological insulators supports surface plasmons with very tight confinement and potentially long propagation distance. The spectral position of these plasmons are also tunable via electric bias or intrinsic doping of the material. In addition, an interesting property of plasmons in topological insulators is the intrinsic angular momentum (spin) carried by the charge carriers [128]. The charge and spin properties of plasmons in topological insulators are discussed in Chapter 4.

This thesis explores the fundamental optical properties in a variety of materials and structures that involve most of the concepts and excitations described in this introduction. The advancement of fabrication techniques, improved characterization tools and a deeper theoretical understanding of different systems presenting interesting optical response at the nanoscale has promoted Nanophotonics to a rapidly growing branch of science and nanotechnology, providing valuable contributions to chemical and physical sciences, biological, medical and health sciences and also to the fundamental understanding of light-matter interaction [9, 129, 130].

Chapter 2

Plasmonic Sensing of Hydrogen in Palladium Nanodisks

As discussed in the Introduction, the optical properties of metals have been widely studied owing to their strong response to electromagnetic radiation. Within the different metals, gold and silver are typically used for plasmonic applications, because of their comparatively low loss and because their response falls in the visible and near-infrared region of the spectrum. Nevertheless, there are other metals as, for example palladium, platinum, aluminium and nickel, whose optical properties are also interesting for several technological applications [24–26, 131]. Palladium is a transition metal with a significant plasmonic response in the visible and near-infrared region. Even though Pd shows large loss compared to gold and silver, its optical properties are actively studied because of the potential applications in various fields of science and technology, as in catalysis, fuel storage or gas sensing [63, 66, 132], among others.

Palladium shows the interesting property that it can dissociate hydrogen molecules at its surface, absorbing the H atoms and accommodating them in the lattice in a reversible way. The presence of H in the Pd lattice results in a change in the electronic [133, 134] and optical [134] properties of the palladium matrix, as well as in a modification of the crystal structure [132, 135]. This change in electronic and optical properties has been explored in the design of hydrogen sensors using Pd [54, 136]. The dissociation of H_2 by Pd is possible because of the high catalytic nature of the Pd surface, which has been widely explored to facilitate the control of chemical reactions [62, 63]. Another area where the fast H absorption and desorption kinetics of Pd [137] is explored is in fuel

storage, as metal hydrides have been identified as an efficient and safe mean for storing H in solid form [68, 132, 135, 138].

In this chapter we analyse the change of the optical properties of Pd when it is progressively modified by the presence of H, which modifies the dielectric response of the resulting Hydride. The presence of H in the Pd lattice will modify the dielectric response of the composite material [139]. In the case of Pd nanostructures, the change in the dielectric response will be particularly reflected in its LSPR response, an effect of interest to design fast and efficient plasmonic H sensors [66, 140–142]. Indeed, detecting minute amounts of atmospheric H, based on LSPR sensing has been recently achieved [54]. Perfect absorption of visible radiation by Pd nanostructures has been also explored in the design of hydrogen sensors [143].

Here, we explore how to interpret the changes on the plasmonic response of palladium nanodisks in hydrogen sensing application [144]. In experiments, it is possible to trace the change in the LSPR response of Pd as the material is modified by the progressive presence of hydrogen. Interpreting these experiments in detail requires to know how the hydrogen is absorbed and how the absorption affects the optical response. However, the theoretical description of the optical properties of PdH-like systems is challenging because of the different length scales involved in the response of the system. Substantial changes occur at the atomic and structural level, such as lattice expansion, requiring a quantum mechanical framework to calculate the resulting dielectric function for different PdH_x compositions. On the other hand, the presence of α and β phases of various H concentrations x in the PdH_x, as well as the size, shape and environmental factors affecting LSPRs resonances in nanostructures [20] that were discussed in the Introduction, need to be addressed in a nano/macroscopaic level. Therefore we follow a multiscale theoretical approach to tackle this problem. Using ab initio quantum mechanical calculations we first obtain the dielectric permittivity of PdH_x as a function of H concentration. In the next step, this permittivity is introduced into the full electrodynamical calculations of the plasmonic response of the hydrogen-modified palladium nanodisks. In this calculations, we employ an appropriate effective medium approximation to address the mixed phase structure of the complex metal hydride. This multiscale theoretical framework provides a solid background to describe plasmonic sensing of the presence of structural domains, as well as for identifying H saturation conditions in metal hydride systems.

2.1. Dielectric response of palladium hydride

The atomic number of Pd is 46 and it crystallises into a FCC structure. When absorbed into the Pd lattice, H atoms reside in the octahedral sites of the lattice, as shown schematically in Fig 2.1(a). This process is accompanied by an increase of the lattice parameter of Pd [136, 145, 146]. An increase in the lattice constant from 3.889 Å to 4.025 Å was experimentally reported when pure Pd is hydrogenated to 70% [136]. Since the optical properties of metals are mainly governed by the free electron plasma oscillations, and the absorption of H by Pd to form PdH_x alters the electron density distribution, the optical properties of palladium hydride depend on the concentration of H atoms in the PdH_x lattice.

We first obtain the dielectric response of PdH_x, ε_{PdH_x}, as a function of the H concentration. Ab initio Time-Dependent Density Functional Theory (TDDFT) calculations of the dielectric permittivity of bulk PdH_x for different H concentration x=H/Pd, are performed by the first-principle calculations group lead by V. M. Silkin at the DIPC [137, 139, 147]. This quantum mechanical calculations consider a homogeneous distribution of H atoms in the energetically favorable interstitial sites (octahedral sites) in the PdH_x lattice. The calculations include the increase in the lattice parameters of the metal during the absorption of H [148]. The lattice parameters for each PdH_x system with different H concentration have been obtained from total energy calculations and the values have been found to be close to experimental data [149]. The internal relaxation of the Pd atoms around H atom positions [150] for ratios $x \neq 1$ is neglected because of the weak influence of this effect in the optical properties.

The dielectric loss function of a material is the negative of the imaginary part of the inverse of its dielectric function, -Im$[1/\varepsilon]$, and the peaks of the loss function correspond to excitation of bulk plasmons. Figure 2.1(b) shows the loss function obtained though the ab initio calculations for the bulk of the stoichiometric homogeneous PdH_x for different H concentrations x (solid lines). A value of x=H/Pd=0 corresponds to pure palladium, whereas H/Pd=1 means a palladium hydride lattice with all octahedral interstitial sites occupied by H atoms. The dashed line in the figure shows the loss function of pure Pd as obtained from optical measurements [61], which agrees well with the energy loss obtained from the ab initio calculations. We also compared our loss functions for pure Pd and PdH_x with values from other ab initio calculations [151–154] as well as with experimental values obtained from energy loss measurements [133, 155–157] and other optical measurements [158], and obtained a good agreement. The prominent peak in

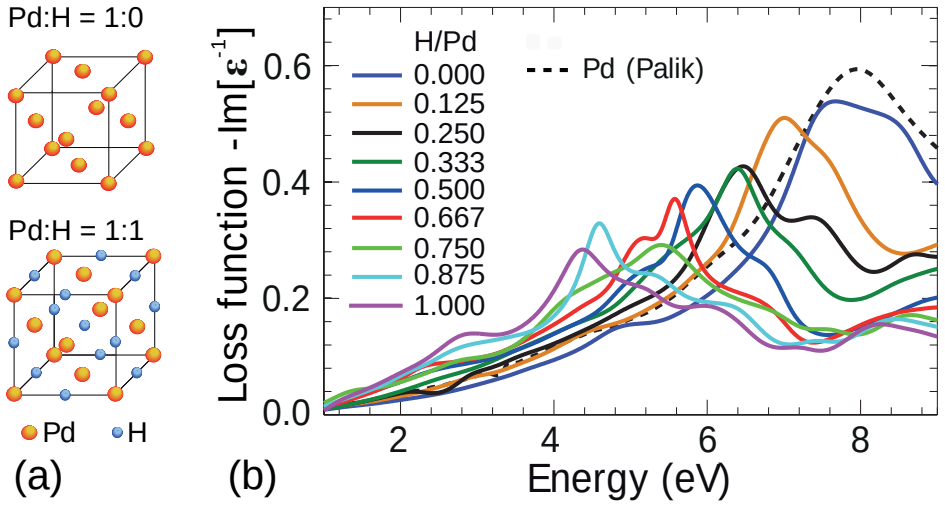

FIGURE 2.1: (a) Crystal lattice of pure Pd (Pd:H = 1:0) and fully hydrogenated Pd (Pd:H = 1:1) used in the ab initio calculations. H atoms occupy the octahedral interstitial sites in the face-centered cubic lattice of palladium to form PdH. (b) Dielectric loss function for bulk PdH_x obtained from ab initio TDDFT calculations performed by Silkin *et. al.* at DIPC, [137] and plotted for different H/Pd concentration values (solid lines). The loss function of pure Pd obtained from optical measurement [61] is also shown (black dashed line).

the loss function, which is a function of H/Pd, indicates the bulk plasmon energy ω_P of PdH_x. The bulk plasmon for pure palladium is observed at 7.78 eV. As the concentration of hydrogen in the lattice is increased the plasmon energy decreases and finally reaches 4.25 eV for a fully hydrogenated sample, where all the octahedral interstitial sites are occupied by H atoms.

The spectral shift of the bulk plasmon peak as a function of H concentration in Fig. 2.1 is almost linear. Although bulk plasmons are not excited by light and the ultraviolet frequencies discussed up to now are not advantageous to perform optical sensing, a similar linear shift has previously been observed in visible and near-infrared spectroscopy experiments using nanodisks (see Fig. 2.8) and, more clearly, nanorings of palladium [67]. In the following subsection we explore in detail the possibilities of different geometries of PdH_x, to bring the energy of the collective oscillations in PdH_x to the optical range, thus allowing for LSPR-based sensing.

2.2. Effect of H concentration on plasmonic resonances

We explore now suitable systems for H sensing in the optical region. With this aim, we analyze the change in the plasmon energy of PdH_x brought by the morphology of the nanosystems: we explore (i) the bulk plasmon (ii) the surface plasmon and (iii) dipolar localized surface plasmon resonances (LSPRs) in spherical particles and disks. At this stage, we consider a homogenous concentration of H in the whole sample and consider the electrostatic limit for the spheres.

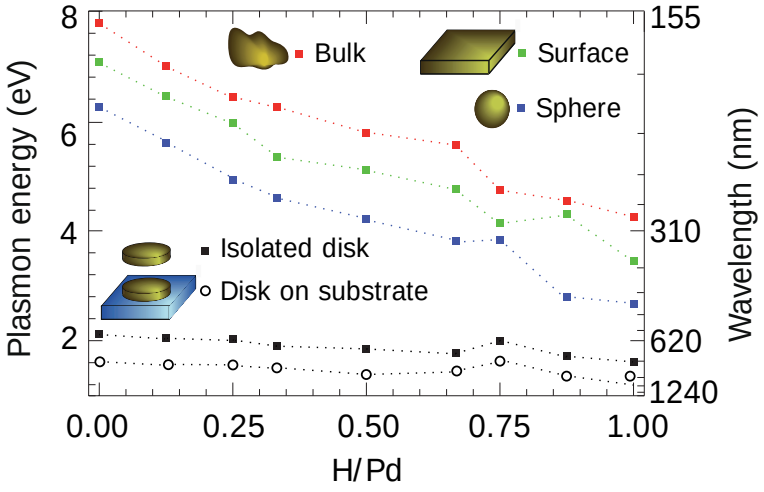

FIGURE 2.2: Energy of the plasmonic resonance of PdH_x systems having uniform stoichiometry for (i) the bulk material, (ii) a flat surface, (iii) a spherical particle in the electrostatic limit, (iv) an isolated disk that is 20 nm thick and 190 nm in diameter, and (v) the same disk deposited on a SiO2 substrate. All values are obtained using the dielectric functions calculated through the TDDFT as a function of the x=H/Pd ratio. In the case of spheres, the electrostatic limit is considered and the resonances studied in the disks and the spheres are dipolar. The dotted lines are guides to the eye.

Figure 2.2 shows the the obtained resonant energies as a function of H concentration, calculated using the corresponding ab initio bulk dielectric functions. The red squares represent the bulk plasmon energies for PdH_x for each x=H/Pd concentrations, extracted from the peaks of the dielectric loss function shown in Fig. 2.1(b). As mentioned in the previous section, the bulk plasmon energy shifts almost linearly with H concentration, but remains in the ultraviolet for all H concentrations.

The energy of the surface plasmon response of a metal-dielectric flat interface always falls below the bulk response of the metal. For the PdH_x-vacuum interface, we obtain the surface plasmon energy from peaks of the surface energy loss function, $g(\omega)$, given

by

$$g(\omega) = Im\left\{\frac{\varepsilon_{PdH_x} - 1}{\varepsilon_{PdH_x} + 1}\right\}, \tag{2.1}$$

where ε_{PdH_x} is the dielectric function of PdH_x for the different H concentrations x. More exactly, the surface plasmon energy (green squares of Fig. 2.2) are obtained as the energy at which Re[ε_{PdH_x}] = -1. For all hydrogen concentrations, the surface plasmon energies are approximately 1 eV less than the bulk plasmon energies. Nevertheless, they still fall in the ultraviolet region of the spectrum, and thus continue being unfavorable for optical sensing.

We can further reduce the energy of the plasmonic response by choosing a sphere in vacuum. The absorption cross section of a spherical nanoparticle in the electrostatic limit is proportional to Im$\{(\varepsilon_{PdH_x} - 1)/(\varepsilon_{PdH_x} + 2)\}$. The dipolar plasmonic mode approximately falls at energies when ε_{PdH_x} = -2, which are also plotted in Fig. 2.2 as a function of H concentration using blue squares. The energies of these dipolar excitations fall between 6 eV for pure Pd and 2.5 eV for a $PdH_{x=1}$ sphere with equal number of Pd and H atoms. Even though the dipolar resonances fall at lower energies than the surface excitations, their energy remains mainly in the ultraviolet region for the different H concentrations.

An effective way of further lowering the energy of the LSPR in the particle is to use PdH_x nanodisks. The coupling of the induced charges at the top and bottom surfaces of the disk produces a substantial redshift of the coupled optical response [159]. To track the evolution of the dipolar LSPR as the H concentration in disks is increased, we perform rigorous electrodynamical calculations using the Boundary Element Method [64, 65] of the far-field optical response of the disks. We first choose a Pd disk of diameter 190 nm and thickness 20 nm in vacuum and a linearly polarized plane-wave illumination incident from the top, and plot in Fig. 2.2 the energy of the lowest energy extinction maximum. The localized dipolar plasmon resonance of the pure Pd disk falls at 2.2 eV, thus considerably reducing the energy of the plasmon excitation down to the visible range. In the presence of an increasing hydrogen concentration in the ambience, the H is absorbed by the disks, changing the dielectric properties of the newly formed PdH_x as described by the ab initio permittivity ε_{PdH_x}. As the H concentration is increased, the plasmon peak redshifts and reaches 1.6 eV for a 100% hydrogenated disk of $PdH_{x=1}$. The gradual shift of LSPR peak is plotted in Fig. 2.2 (black squares) as a function of H concentration.

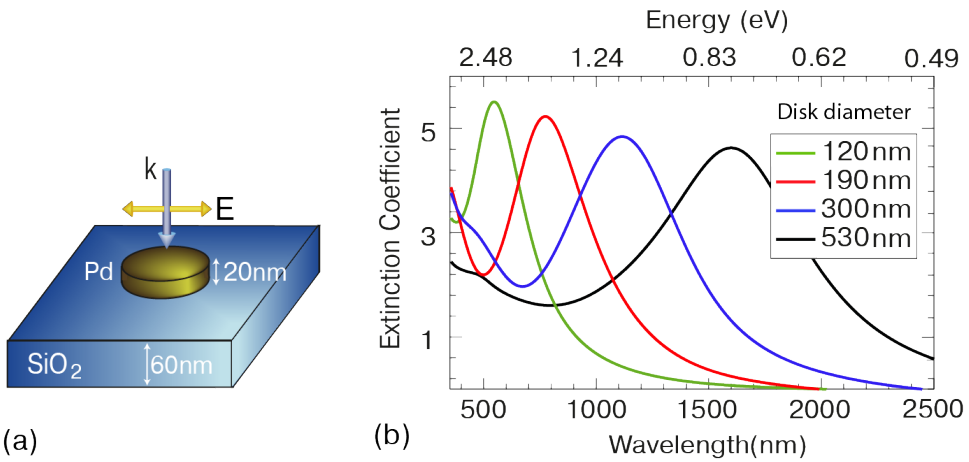

FIGURE 2.3: (a) Schematic of the system used in the electrodynamic calculations to obtain the far-field optical response of the Pd nanodisks. Disks of thickness 20 nm are deposited on a SiO_2 substrate of thickness 60 nm and illuminated by a linearly polarized plane-wave incident normally from the top. (b) Extinction spectra of the Pd disks for different diameters, calculated using the ab initio dielectric function.

In a realistic situation, the disks are usually deposited on a dielectric substrate, which causes a further reduction of the LSPR energy of the disks. Therefore, we consider next the same PdH_x disks deposited on a SiO_2 substrate, under identical plane-wave illumination. The substrate has a disk geometry with dimensions three times that of the Pd disk. The energies of the resonance peaks of this situation for various H concentrations are also shown in Fig. 2.2 as open circles. The interaction of the disk with the substrate reduces the LSPR energy by approximately 0.5 eV for all H concentrations.

The properties of localized plasmons supported by a nanoparticle strongly depend on the size and geometry of the system [159]. This allows for further tuning of the LSPR in the disk by varying the size and thickness of the disk. To demonstrate this tunability, we choose the system schematically shown in Fig. 2.3(a), where a pure Pd disk of 20 nm thickness is deposited on a SiO_2 substrate of thickness 60 nm and diameter three times that of the disk. Figure 2.3(b) shows the extinction spectra of the system calculated for different sizes of the Pd disks varying from 120 nm to 530 nm. The redshift of the spectral peak as the diameter is increased demonstrates the tunability of the LSPR response with a peak that redshifts from $\lambda = 542$ nm resonant wavelength for the smaller disk to λ=1597 nm for the larger one, demonstrating the tunability of the system.

By carefully choosing the morphology of PdH_x structures, we are thus able to bring the LSPR energies of the PdH_x disks to the visible-near infrared range. While the disks of smaller radius show LSPR in the visible region, increasing the diameter brings the

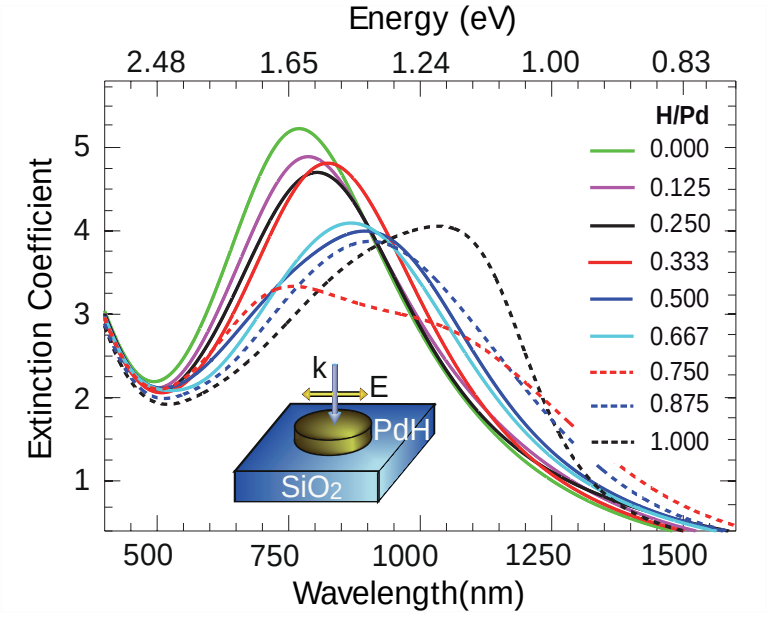

FIGURE 2.4: Extinction spectra of PdH_x disks of 20 nm thickness and 190 nm in diameter with uniform stoichiometry, placed on a SiO_2 substrate of thickness 60 nm and illuminated with linearly polarized plane-wave (inset), evaluated for different $x =$ H/Pd values. The disks are characterized by the dielectric functions as obtained from the TDDFT calculations in Fig. 2.1(b).

resonance into the IR region. This tunability provides an opportunity to use nanodisks of PdH_x in remote optical sensing of H at easily accessible wavelengths, by first choosing an adequate size and then following the LSPR shift of the disks as a function of H concentration. Having identified a suitable system for LSPR sensing, we proceed to analyse in more detail the response of the Pd structure as H is absorbed.

We focus in the rest of this chapter on the configuration giving the lowest energy in Fig. 2.2, a Pd disk of diameter 190 nm and thickness 20 nm, deposited on a SiO_2 substrate, under the same linearly polarized illumination from the top. Fig. 2.4 shows the extinction spectra for different H concentrations.

It can be observed from the figure that even though the concentration of hydrogen in the system is increased gradually, the corresponding LSPR shift is not monotonous with H concentration. A similar behaviour of LSPR shift can be also appreciated in the case of the disk completely surrounded by vacuum (Fig. 2.2). This result does not correspond to our expectation from the experimentally observed linear LSPR shift for related systems [67].

So far in the description of the PdH_x, the inhomogeneities arising in the medium as a result of H absorption have not been taken into account. The concentration of H in

the PdH_x lattice was assumed to be perfectly homogeneous, with the hydrogen atoms distributed in the octahedral sites of the Pd lattice in the complete structures. In reality, similar to other metal hydrides, PdH_x systems with $x > 0$ are not single-domain crystals. Instead, they present a mixture of two phases called α and β. The α phase is characterized by a very small concentration of H atoms and can be considered to present the same dielectric properties as pure Pd. As a result, the dielectric properties of the α phase are very similar to pure Pd. The β phase, on the other hand, has comparatively larger concentration of H [135, 160, 161] and the corresponding ε_{PdH_x} needs to be used.

The optical response of composite materials that contain an admixture of two or more components with different dielectric responses are usually addressed with the use of an effective dielectric function. There are different effective medium theories to derive the effective dielectric function of such systems. A brief overview of commonly used effective medium theories are given in Appendix C.

2.3. Effective medium description for the two-phase PdH_x composite

To take the structural inhomogeneities in PdH_x into consideration, we treat the bulk material as a mixture of α and β phases. We consider that the α phase with plasmon energy $\omega_P^\alpha \approx 8$ eV, occupyies a $(1 - f_\beta)$ fraction of the volume and the β phase, with plasmon energy $\omega_P^\beta \approx 4.2$ eV, the remaining f_β. f_β is thus the fraction of β phase. In a very simple approach, the dielectric properties of such a composite medium can be characterized by an effective dielectric function $\varepsilon_{\text{eff}}(z)$ defined as

$$\varepsilon_{\text{eff}}^{-1}(z) = (1 - f_\beta)\varepsilon_\alpha^{-1} + f_\beta \varepsilon_\beta^{-1}, \tag{2.2}$$

where z is the fraction of H in the whole sample, given by $z = x\, f_\beta$. Figure 2.5 displays the result of the effective loss function calculated using Eq. (2.2). Here, the material forming the β domains is assumed to be $PdH_{x=1}$, i.e., equal number of H and Pd atoms.

A comparison of the effective loss function in Fig. 2.5 with the loss function shown in Fig. 2.1(b) shows that the evolution of the bulk plasmon peak as a function of H concentration when using Eq. (2.2) to describe an inhomogeneous PdH_z medium composed of α and β domains is very different from what is observed when the medium is assumed to be homogeneous. In the latter case [Fig. 2.1(b)], the energy of the bulk

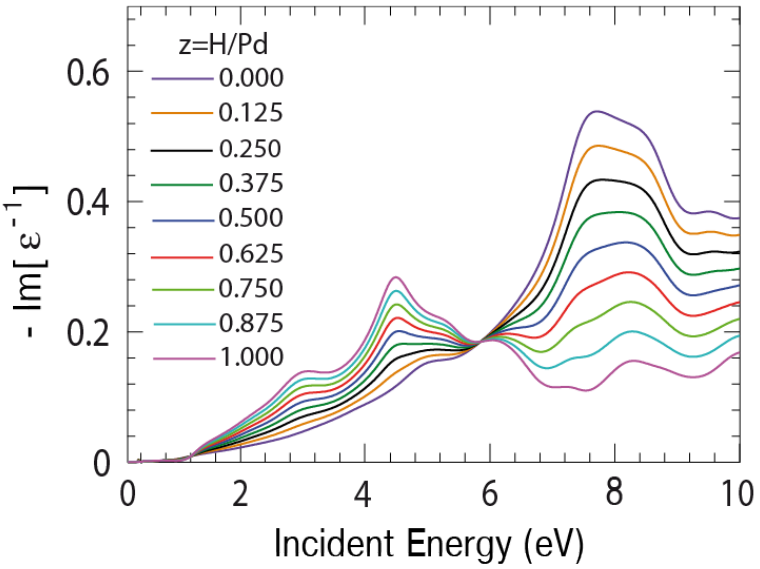

FIGURE 2.5: Evolution of the loss function -Im$[1/\varepsilon]$ and resulting bulk plasmon peaks of PdH_z with the effect of H absorption described by a dielectric function derived from a simple effective medium following Eq. (2.2). The f_β phase composed of $PdH_{x=1}$.

plasmon is decreased and the strength of the loss function peak is reduced gradually as the concentration of H is increased. In contrast, for the inhomogeneous medium (Fig. 2.5), as the concentration of H is increased, the intensity of the bulk plasmon peak corresponding to the pure Pd (at $\omega_P^\alpha \approx 8$ eV) gradually diminishes, without any apparent change of its energy. This effect is accompanied by the appearance and gradual strengthening of a new plasmon peak at low energy ($\omega_P^\beta \approx 4.2$ eV), which corresponds to the plasmon peak position for the homogeneous $PdH_{x=1}$ material. The peaks at large and low energies can thus be directly associated to the α and β phases in the effective medium respectively, and the strengthening of the lower energy peak can be related to the gradual growth of the β phase as the H absorption in the medium is increased. This scenario has been already discussed by Bennett *et al.* [133] based on the experimental plasmonic spectra of bulk PdH_x systems.

We have discussed above a simple approach to define the dielectric response of palladium hydride based on a simple averaging of the responses of pure Pd and PdH_x of certain concentration of H. Nevertheless, there are standard theoretical methods, called effective medium approximations, to define more rigorously the dielectric response of composite materials, formed by the mixing of two or more materials (phases). In this thesis, we focus on Bruggeman's effective medium.

2.3.1. Bruggeman's effective medium approximation

Bruggeman's effective medium approximation is often used to describe the response of materials, like PdH_x, characterized by two different phases, both occupying a large fraction of the volume [162–165]. In the implementation of this effective medium, we also take into account another important aspect of metal hydride formation, the H saturation in PdH_x. Recent experiments on PdH_x nanoparticles which explore their plasmonic response to sense the storage of H, show that Pd metal gets saturated at fractions of H of about $x \approx$ 0.6-0.7 [66, 67]. In the case of nanoparticles, the exact saturating point depends on the morphological aspect of the particles. We assume a 66.7% of H saturation, which is reasonable for the system we are investigating. As the concentration of H is increased in the system, the volume of the β phase is increased and for a fully saturated sample, the sample will be filled with β phase domains having 66.7% of H. The Bruggeman's effective medium, is obtained from the equation

$$f_\beta \frac{\varepsilon_\beta - \varepsilon_{\text{eff}}(z)}{\varepsilon_\beta + 2\varepsilon_{\text{eff}}(z)} + (1 - f_\beta) \frac{\varepsilon_\alpha - \varepsilon_{\text{eff}}(z)}{\varepsilon_\alpha + 2\varepsilon_{\text{eff}}(z)} = 0, \tag{2.3}$$

where the effective medium is described by the effective dielectric function $\varepsilon_{\text{eff}}(z)$. The total z =H/Pd number ratio, z, corresponds in this case to $z = x \cdot f_\beta$, with $x = 0.667$ the saturation level. In Appendix C we provide a brief overview of Bruggeman's effective medium approximation. The effective medium consists again of α and β phases, consisting respectively of pure Pd and $PdH_{x=0.667}$. Their corresponding dielectric permittivities are $\varepsilon_{PdH_{x=0}}$ and $\varepsilon_{PdH_{x=0.667}}$ respectively, and f_β is the fraction of the β phase. By definition, the Bruggeman's effective medium approximation incorporates the electromagnetic interaction between the domains dispersed in the effective medium. Equation (2.3) is solved to obtain the effective dielectric function $\varepsilon_{\text{eff}}(z)$ and the resultant loss function of this effective media is shown in Fig. 2.6(a) when the β phase is characterized by $PdH_{x=0.667}$. It can be seen from the figure that as the concentration of hydrogen is increased the bulk plasmon peak at energies around 7 eV starts redshifting and for higher concentrations a new bulk plasmon peak appears at low energies.

In order to get more information on the H saturation and domain distribution in the medium, we also test a higher level of H saturation for β phase in the construction of the effective medium response. This is done by characterizing the β phase using the ab initio dielectric function for $PdH_{x=1}$, which assumes a 100% hydrogenation of this phase. Fig. 2.6(b) shows the corresponding loss function. The evolution of the bulk plasmon peak as a function of hydrogen, in this case, also presents redshifting peaks, but

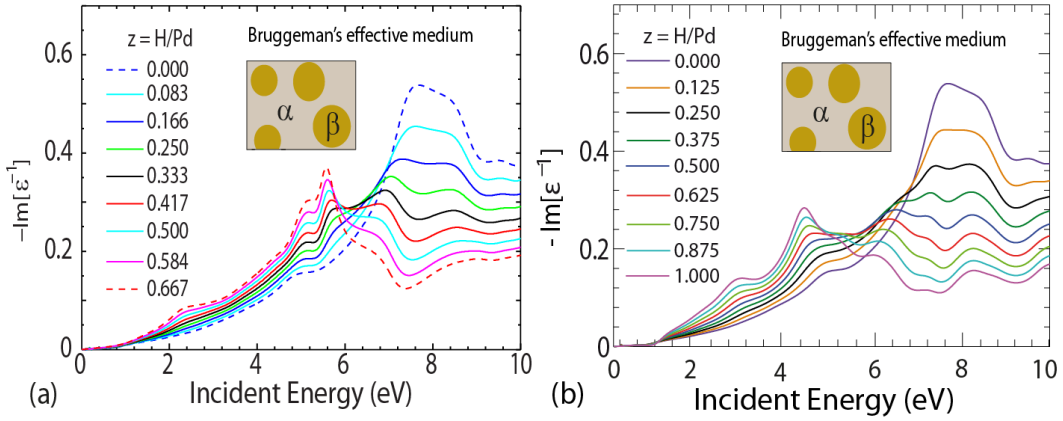

FIGURE 2.6: The evolution of the bulk plasmon peaks of PdH_z as a funcion of H absorption z=H/Pd, obtained from a dielectric function derived using Bruggeman's effective medium approximation [Eq. (2.3)], with the β phase assumed to be characterized by (a) $PdH_{x=0.667}$ and (b) $PdH_{x=1}$.

it is qualitatively different from the case where hydrogen saturation occurs at $x = 0.667$ [Fig. 2.6(a)].

We proceed with the full electrodynamical calculations of the 20 nm thick disks of 190 nm diameter deposited on SiO_2, as in Fig. 2.4 but using the Bruggeman effective dielectric function to characterize the PdH_z nanodisk. The calculated extinction spectra is shown in Fig. 2.7, where we consider both x=0.667 and x=1 for the β phase. An increase of H concentration in the system is modelled by an increase of the β phase fraction f_β in the entire two-phase system and this results in a redshift of the dominant dipolar resonance of the system. The LSPR shift calculated for disks of larger sizes also shows a similar trend, as shown later in Fig. 2.8.

To better compare the results obtained using the two different levels of H saturation, we plot in Fig. 2.8, the LSPR shifts for the case with larger (blue dots) and smaller (red dots) H concentration at saturation (β phase $PdH_{x=1}$ and $PdH_{x=0.667}$, respectively) and compare them with experimental results (green dots). Here we choose a disk of diameter 300 nm and thickness 20 nm for direct comparison with the experimental results. The experimental data is provided by Prof. Igor Zorić at Chalmers University of Technology. For completeness, the LSPR shift obtained for a disk of homogeneous PdH_x, as obtained from Fig. 2.4, is also plotted (black squares).

It can be observed from Fig. 2.8 that the calculated LSPR shift using a H saturation of $x = 0.667$ for the β phase (red dots) shows excellent agreement with the experimental values. This result supports our assumption that two different phases are formed by

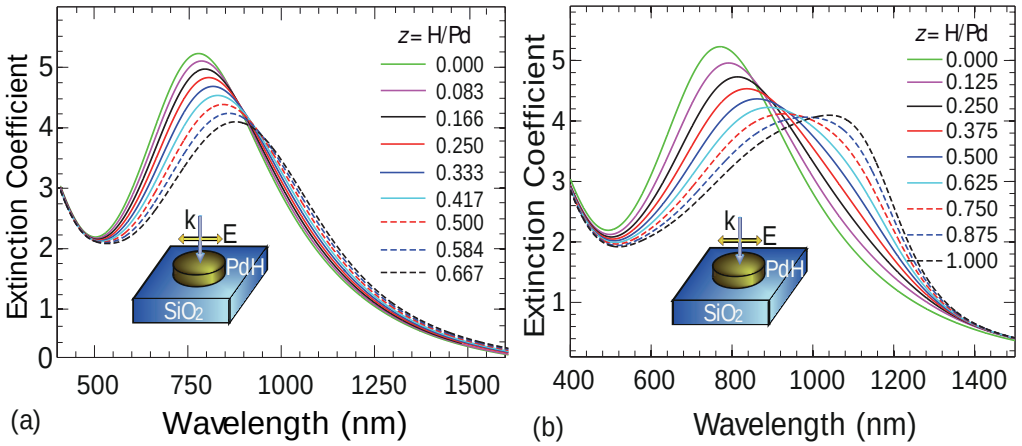

FIGURE 2.7: Extinction spectra calculated for a disk of 20 nm thickness and 190 nm diameter deposited on a 60 nm thick SiO_2 substrate. The disks are characterized using Bruggeman's effective dielectric functions with β phase domains characterized as (a) $PdH_{x=0.667}$ and (b) $PdH_{x=1}$ for different z = H/Pd ratios of the entire system.

the absorption of H, one of them Pd and the other saturated to x near 0.667. In this case, when the PdH_x system is saturated, the H/Pd ratio for the whole medium is equal to 0.667. On the other hand, when the H saturation in the β domains is set at $x = 1$ the LSPR shift (blue dots), or when a homogeneous PdH_x (only one phase) is considered, the results significantly deviates from the experimentally observed shift. In this case, when the whole medium is filled with β phase domains, the value of z = H/Pd reaches 1. The deviation of the LSPR shift when considering 100% H saturation is an evidence against the possibility of full hydrogenation of the β phase domains. These results show that analyzing the LSPR shift can provide valuable information about the dynamics of domain formation in hydrogen uptake by Pd nanodisks. Nonetheless, an exact comparison would require to consider a more complete description of the system, including effects such as temperature, the evolution of boundaries and surface roughness caused by the hydrogenation of the Pd disks [66, 166].

Last, we notice that the results presented above show that by properly choosing the H saturation and by proper weighted-averaging of the α and β phase domains we obtain a linear LSPR shift as the H concentration is increased. At the same time, no linear shift in the bulk plasmon energy ω_P is seen in Fig. 2.6. However, a close analysis of the dielectric loss functions derived using Bruggeman's effective medium approximation (Fig. 2.6) shows that the loss function varies almost linearly with x in the spectral region of LSPR resonances (1-3 eV), explaining the linear LSPR shift.

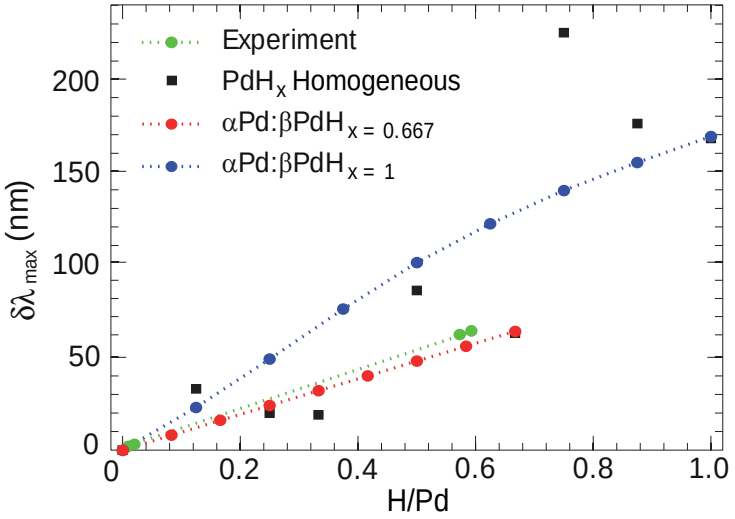

FIGURE 2.8: LSPR shifts calculated for a Pd-H disk of 20 nm thickness and 300 nm diameter plotted as a function of the hydrogen concentration z=H/Pd averaged over the full system. The resonance shifts obtained for the Bruggeman's effective dielectric function [Eq. (2.3)] are shown for the β phase taken as PdH$_{x=0.667}$ (red dots), and as PdH$_{x=1}$ (blue dots). The black squares correspond to the LSPR shift of an homogeneous disk shown in Fig. 2.4. The green dots are taken from experimental results in Ref. [67].

2.4. Summary

In this chapter we explored the optical response and hydrogen absorption properties of palladium, a non-conventional plasmonic metal, for hydrogen sensing applications. We developed a theoretical method which combines ab initio quantum mechanical calculations with classical electrodynamics to study the optical response of nanometer sized metal hydride systems. This multiscale theoretical approach allows to address the atomic scale as well as mesoscopic scale changes occurring in a metal hydride due to the absorption of hydrogen. We first discuss how the choice of a simple morphology, nanodisks deposited on SiO_2 substrate, can be favourable for performing optical sensing of hydrogen in PdH. Later, it is demonstrated using PdH nanodisks that plasmonic sensing techniques can be used as a valuable tool for studying the dynamics of H absorption in metal hydride nano-systems, including the presence of different phases. By a proper choice of the effective medium approximation, our theoretical results assuming saturation of the β phase to x=H/Pd=0.667 are in good agreement with the experimentally observed plasmon shifts. More generally, the methodology developed and presented in this chapter establishes a promising path to treat hydrogen absorption and related processes in different metallic nanoscale systems. From the technological point of view, the

results presented here can help to advance the understanding of hydrogen storage and to develop nanodevices for sensing.

Chapter 3

Optical Response of High Refractive Index Nanostructures

The interaction of electromagnetic radiation with micron-sized dielectric structures has been a subject of active research for several decades. A significant portion of the attention in this field was devoted, for example, to electromagnetic resonances in structures such as Fabry-Perot cavities, photonic crystals and whispering gallery mode resonators [11, 13, 167, 168]. Some of these structures can confine light to a sub-wavelength regions, but their typical physical size is usually significantly larger.

Here we are interested in resonances of dielectric structures of small size, comparable to the wavelength of the illuminating radiation, i.e., in low-loss dielectric dimers with dimensions of a few hundreds of nanometers (sub-micron sizes). These structures can be advantageous for controlling the emission from molecules and quantum dots and in directional emission of radiation [29, 88, 169, 170]. In the Introduction Chapter we discussed briefly the electric and magnetic antenna properties of a sub-micron silicon sphere, as proposed in Ref. [28]. A silicon sphere of 150 nm shows distinct electric and magnetic dipolar resonances at $\lambda = 864$ nm and 1108 nm respectively, which present strong enhancement, not only of the electric but also magnetic near-fields, which can be exploited for probing magnetic transitions in materials [86, 87, 171].

In this chapter we discuss the scattering properties and the electric and magnetic near-field enhancement in a dimer antenna made of two identical silicon spheres. The polarization of the incident light controls the orientation of the dipolar electric and magnetic modes excited in the individual spheres and thus the resulting coupling between the

two particles and the optical response obtained. To better understand the coupling, we also develop a numerical model in which each sphere is represented by equivalent electric and magnetic dipoles. This model allows us to identify the contributions to the response from the electric-electric, magnetic-magnetic and electric-magnetic interactions between the particles. The model also explains the emergence of a new feature in the far-field spectra for small dimer gaps due to a strong interaction between the electric and magnetic modes at each sphere.

3.1. The system

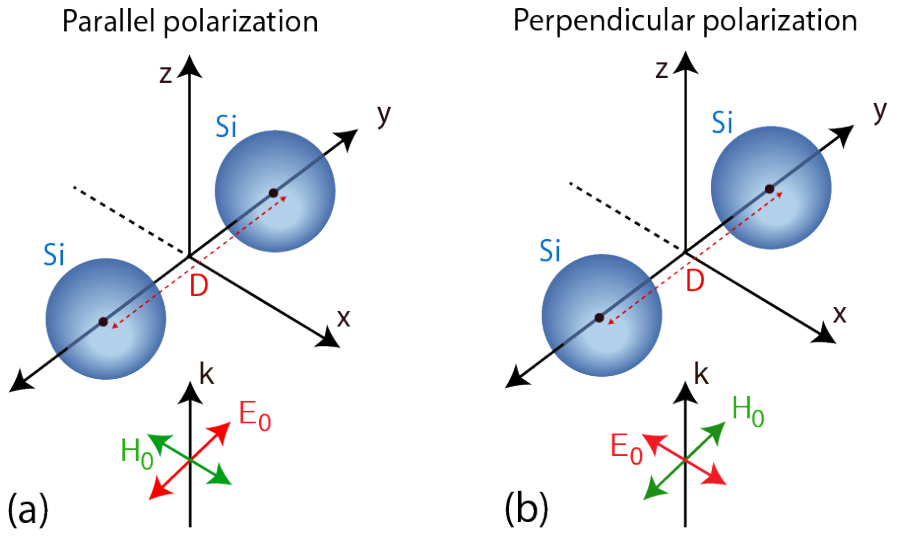

FIGURE 3.1: Schematic representation of the silicon sphere dimer, under a linearly polarized plane-wave for (a) parallel and (b) perpendicular illuminations, with electric field parallel and perpendicular to the dimer axis, respectively, and incident along the z direction. The spheres are identical with radius $a = 150$ nm, and are located at $(0, D/2, 0)$ and $(0, -D/2, 0)$, respectively, such that the gap distance is given by $D-2a$, i.e., separated by a center to center distance D along the y axis. The same scheme is valid also for the gold dimer studied in this chapter.

We investigate the optical response of dimers made of two identical silicon spheres of radius $a = 150$ nm. The dimer axis is the common axis of the spheres, which is chosen as the y axis, as shown in Fig 3.1 (a) and (b). We consider as illumination source, a plane-wave that is incident along the z direction normal to the dimer axis, and that has electric field polarized parallel or perpendicular to the dimer axis, referred to in the following as parallel and perpendicular polarization, respectively (Fig. 3.1). All the near-field maps shown in this chapter are calculated in the $z = 0$ plane, with the center of the spheres corresponding to $(0, D/2, 0)$ and $(0, -D/2, 0)$. The electric and magnetic

field enhancements are defined as the ratio of the total field to the incident fileld, given by $|E_{tot}|/|E_0|$ and $|H_{tot}|/|H_0|$ respectively. The same illumination scheme is used also in simulations of gold sphere dimers of radius 150 nm, performed for comparison. The dielectric functions of silicon and gold are obtained from Ref. [61]. We use the Lumerical FDTD software to perform the numerical simulations to solve Maxwell's equations [172].

3.2. Parallel electric polarization

In order to use the silicon dimers to perform field enhanced spectroscopy, it is desirable to have strong near-field enhancement [47]. In the case of metallic dimers when the incident electric field is parallel to the axis, it is well known that the field enhancement is maximum in the gap [53]. Therefore, we first study the response of a silicon sphere dimer for parallel polarization to explore the possibilities of the low loss materials in this configuration. We first analyse the far-field response, and later focus on the near-field response.

3.2.1. Far-field response

An individual sub-micron silicon sphere can present strong electric and magnetic response [28]. When a dimer made of two of such spheres is illuminated by a linearly polarized plane-wave, the optical response is dominated by the self-consistent electromagnetic interaction between the modes of the individual particles. Figure 3.2(a) shows the extinction spectra of the dimer calculated for different gap distances ranging from 4 nm to 300 nm. The spectrum of a single sphere of radius 150 nm, shown in Fig. 1.7 is also shown here for easy comparison (dashed line).

The spectrum for large dimer gaps, as for example when the two spheres are 300 nm apart (black line), is very similar to the spectrum presented by a single isolated sphere (dashed line). Since the spheres are sufficiently apart from each other, the interaction between the dipoles excited at each sphere is weak. Therefore, according to the discussion in the introduction, the strong and distinct peak at $\lambda = 1090$ nm corresponds to the magnetic dipolar mode in each sphere. The broad peak at $\lambda = 844$ nm corresponds to the electric dipolar mode and the small peak at $\lambda = 803$ nm to the magnetic quadrupolar mode of the spheres. As the dimer gap is reduced to a few tens of nanometers, the induced electric and magnetic dipoles at both spheres, interact more strongly, resulting in a gradual shift of the spectral peaks. For example, when the gap is 50 nm, the magnetic

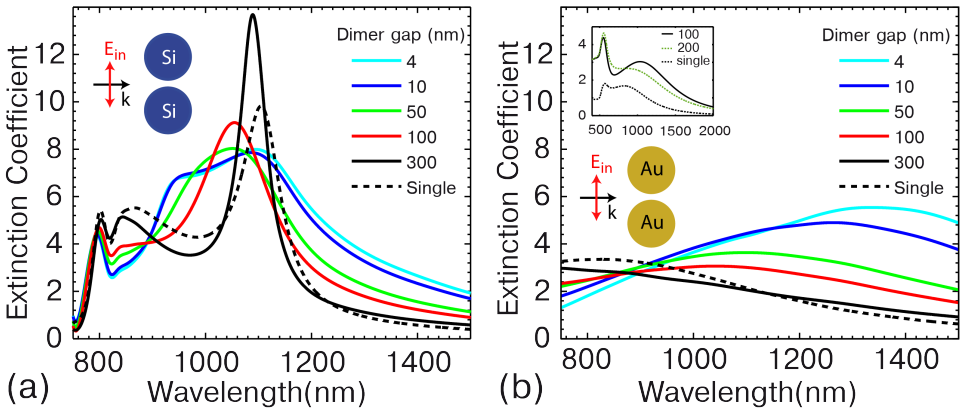

FIGURE 3.2: (a) Extinction spectra of a silicon dimer composed of spheres of radius 150 nm calculated for different dimer gaps (solid lines) for parallel polarization, as shown in the inset. The spectrum presented by an isolated single silicon sphere of radius 150 nm is also shown (dashed dark line). (b) Extinction spectra calculated for a gold single sphere (dashed dark line) and a gold dimer (solid lines) of the same geometry and gap distances as in (a). The inset in (b) shows the result for a broader spectral range for the single gold sphere and the gold dimer with 100 and 200 nm gap distances.

dipolar peak is blueshifted and it appears at $\lambda = 1051$ nm. Since the incident electric field is along the y direction, the induced magnetic dipoles in each sphere are oriented along the x direction in a side-by-side configuration. As a result of the repulsive force between the dipoles, the resonant energy of this system increases as the dimer gap is decreased below ~ 300 nm, which results in the observed blueshift. Interestingly, as the gap is further decreased below 50 nm, a redshift is observed, and for a distance of 4 nm, the peak appears at $\lambda = 1095$ nm, which we attribute to the influence of other resonant modes as we will explain in Section 3.4.1.

On the other hand, in the case of the peak due to the interaction of the electric dipoles ($\lambda \approx 860$ nm), a redshift is observed as the dimer gap is reduced below 300 nm (this is observed more clearly in Fig. 3.9). The exact peak position becomes difficult to distinguish in the far-field for a gap distance smaller than 50 nm. Since the incident electric field is polarized along the y axis of the dimer, the induced electric dipoles are oriented in the same direction, in a colinear configuration. The energy of this system decreases as the dimer gap is reduced (assuming retardation can be neglected) because of the attractive force between the dipoles, resulting in the observed redshift. We refer to this situation as a coupled dipolar electric resonance.

Interestingly, for gap distances below 50 nm, a new peak appears at $\lambda \approx 960$ nm at an intermediate wavelength between the electric and magnetic dipolar peaks of an isolated sphere. To explain this mode, we need to take into account a secondary electric dipole

at each sphere, oriented along the z direction, induced by the magnetic dipole in the neighbouring sphere. The new peak is the result of the coupling between the secondary electric modes and the magnetic modes. For large gap distances, the strength of the field of each magnetic dipoles at the position of the neighbouring sphere is too weak to efficiently couple with the secondary electric dipolar mode. The interaction between the different modes of the individual spheres is explained in more detail in Section 3.4.

We also notice that, for all the gap distances considered, the spectral shift in the magnetic quadrupolar peak is relatively small compared to the shift of the dipolar peaks. This can be attributed to the strong localization of the near-fields of these modes, which results in a weaker interaction between the modes in each sphere.

To compare the strength of the scattering obtained for the silicon dimers, and for similar plasmonic systems typically used in field enhanced spectroscopy, we also consider briefly the far-field response of a gold dimer. The radius of the sphere, the gap distance and the polarization of the illumination are the same as for the silicon dimer system in Fig. 3.1. The resulting extinction spectra of the gold dimer and a single gold sphere are shown in Fig. 3.2(b) in the wavelength range of 750 - 1500 nm. The spectra of the sphere and of the dimer for separations of 100 nm and 200 nm are also shown for a broader spectral range in the inset of Fig. 3.2(b). Notably, the extinction coefficient of the silicon dimers in the spectral range studied here is similar to the values of the gold dimers. Moreover, the gold dimer presents a broader resonance due to the larger losses. Because of this reason, the use of silicon particles could be interesting in photonics due to their well defined resonances.

3.2.2. Near-field enhancement

We study next the near-field enhancement in the dimer for parallel polarization. Figure 3.3(a) shows the electric field enhancement at the center of the gap. Since the incident electric field is polarized along the axis of the dimer, the electric dipoles are arranged in a colinear configuration, and oscillate in phase, leading to field enhancement in the gap. For sufficiently small gap distances the interaction between these induced dipoles becomes strong, which results in a strong electric field in the dimer gap.

In order to compare the enhancement obtained with that of a standard plasmonic system, we also calculate the electric field enhancement spectra in the middle of a gold dimer of same dimensions and for the same gap distances and polarization. The field enhancement

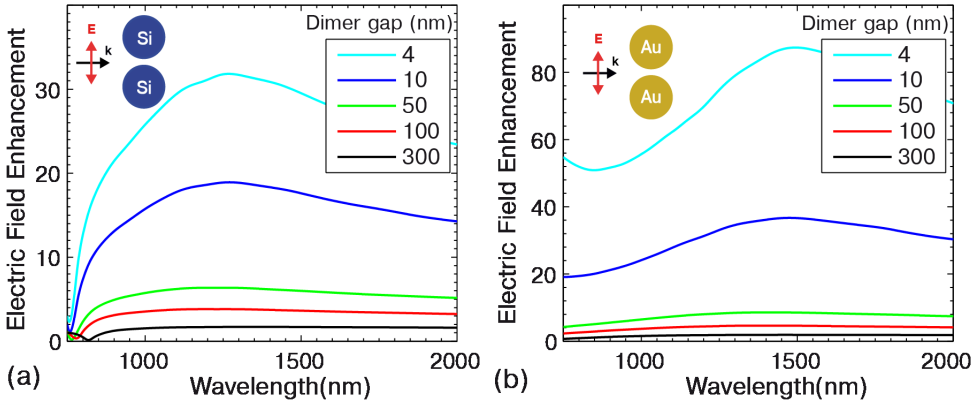

FIGURE 3.3: (a) Electric field enhancement $|E_{tot}|/|E_0|$ spectra for a dimer of silicon spheres of radius 150 nm for different gap distances, and parallel polarization, as shown in the inset. (b) Electric field enhancement spectra for gold dimer for the same size of the spheres, illumination and gap distances. In both cases, the field enhancement is calculated in the center of the gap.

obtained is displayed in Fig. 3.3. For small gap separations, metallic dimers provide around two times more field enhancement in the gap compared to dielectric dimers. Nonetheless, metallic systems have high losses and often result in large signal background [71], which can be undesirable for spectroscopies and emission processes [173, 174]. In the case of dielectric antennas, even though the electric field enhancement is smaller than for their metallic counterparts, the low losses and thus very small quenching of the emitter, together with the spectrally broad response, qualifies them as interesting candidates for field enhanced spectroscopy.

In order to better understand the enhancement and localization of the fields in the dimer, the electric and magnetic field distributions around the dielectric antenna are studied in the following. Figure 3.4 shows the electric and magnetic near-field enhancement maps calculated in the $z = 0$ plane for the spectra in Fig. 3.2(a). The field maps are plotted for $\lambda = 1100$ nm, which is referred to as the coupled electric resonance, although a similar field distribution is seen in a broad spectral range, roughly between 800 nm to 2000 nm. The electric field enhancement is localized in the dimer gap. The obtained field distribution together with the phase of the electric fields in the spheres [see arrows in Fig. 3.4(a)] corresponds to the excitation of two electric dipoles oriented along the dimer axis, indicating that the coupled electric dipolar resonance produces an electric field enhancement in the gap. For a better view of the electric field enhancement, a zoom of the field distribution in the antenna gap is also shown in Fig. 3.4(b).

We concentrate next on the strong magnetic resonances supported by the silicon spheres

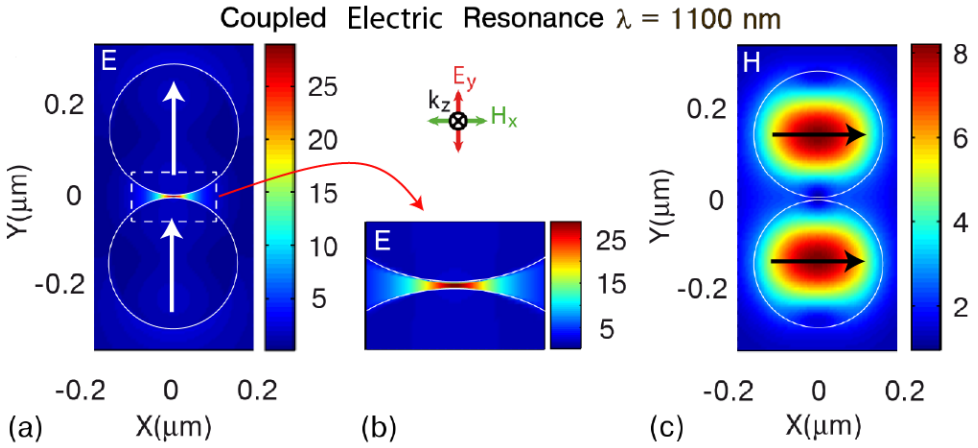

FIGURE 3.4: Electric $|E_{tot}|/|E_0|$ (a) and magnetic and $|H_{tot}|/|H_0|$ (c) field enhancement calculated near a silicon dimer with gap distance 4 nm, illuminated at the resonance wavelength $\lambda = 1100$ nm. The field is calculated in the $z = 0$ plane for a parallel polarization of the light incident along the z axis [see Fig. 3.1(a)]. (b) A zoom of the electric field enhancement in the dimer gap. In (a) and (c), the arrows indicate the orientation of the electric and magnetic dipoles, respectively.

to investigate the possibility of obtaining strong magnetic fields. Figure 3.4(c) shows the magnetic field enhancement for the same conditions as before. A relatively strong magnetic field is found but it is distributed inside the spheres, which is not favourable for accessing magnetic fields, for example to enhance magnetic transitions [86, 175]. This magnetic field is the result of the electric current loop in each sphere in the $y-z$ plane, which has a normal along the x direction. The electric and magnetic field maps address the simultaneous excitation of the electric and magnetic dipolar modes in the spheres.

It is desirable to get strongly localized and enhanced magnetic field in the dimer antennas which could facilitate stronger coupling between the antenna and sample. Since the incident electric field is parallel to the dimer axis, the resultant magnetic dipoles are aligned side-by-side and parallel to the x axis [see the arrows in Fig. 3.4(c)]. Outside the spheres, we can observe very weak magnetic fields, which is opposite to what is desired. Moreover, the strength of the magnetic fields inside the spheres is even smaller than the field inside an isolated single sphere at magnetic resonance [see Fig. 1.7(d)]. The reason for this decrease is that the magnetic field induced by each sphere in the dimer interferes destructively with the magnetic field in the neighbouring sphere.

On the other hand, the result for the electric enhancement [Fig. 3.4(a)] allow us to expect an enhanced magnetic field in the gap for a polarization of the incident light favouring the alignment of the magnetic dipoles along the axis of the dimer. We thus study in the next section, the response of the dimer for perpendicular polarization.

3.3. Parallel magnetic polarization

3.3.1. Far-field response

In order to explore the possibilities of the magnetic response in dielectric dimers, we first study the far-field response for electric polarization perpendicular to the dimer axis. For this illumination, the electric dipoles excited in both spheres are aligned in the same direction, side-by-side along the x axis and oscillating in phase. More interestingly, the orientation of the induced magnetic dipoles are oriented colinearly along the dimer axis aiming at providing magnetic field enhancement in the gap. We refer to the mode resulting from the coupling between the magnetic dipoles as the coupled magnetic resonance.

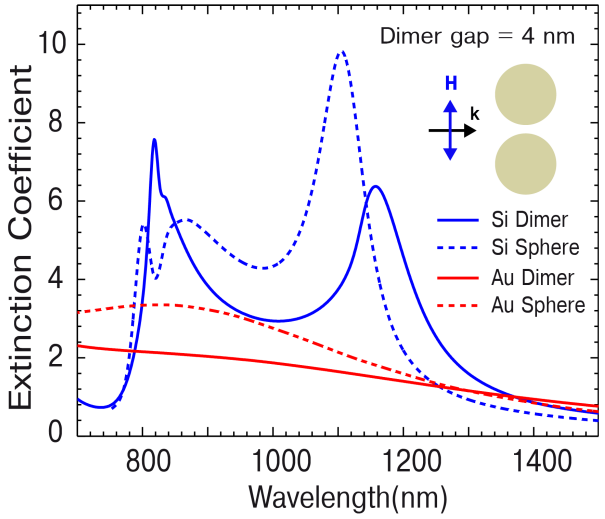

FIGURE 3.5: Extinction spectra for a silicon dimer (blue solid line) of gap distance 4 nm and a for a single silicon sphere of radius 150 nm (blue dashed line), for perpendicular polarization of the incident electric field, as shown in the inset. The extinction calculated for a dimer (red solid line) and a sphere (red dashed line) of gold, under otherwise identical conditions as for Si, are also shown for comparison.

Figure 3.6(a) shows the extinction spectra of a silicon dimer for a gap distance of 4 nm (blue line), together with the response of a single silicon sphere (blue dashed line). The spectra of the single sphere (blue dashed line) undergoes two main modifications when they are brought together to form the dimer. The magnetic dipolar resonance peak of the single sphere at $\lambda = 1108$ nm is redshifted and becomes the coupled magnetic resonance at $\lambda = 1164$ nm. In contrast, the electric dipolar peak of the single sphere at $\lambda = 864$ nm is blueshifted and overlaps with the magnetic quadrupolar peak around $\lambda \approx 820$ nm.

Since the spheres are very close to each other and retardation is small, the strong interaction between the induced magnetic dipoles aligned along the dimer axis reduces the total energy of the coupled magnetic resonance, and redshifts the corresponding peak. This behaviour is similar to the redshift of the coupled electric dipoles observed for small dimer gaps and parallel polarization [Fig. 3.2(a)]. In contrast, the electric dipoles are oriented paralelly along the x direction, similarly to the magnetic resonance in Fig. 3.2(a), and the resulting resonance is blue-shifted, as has also been demonstrated for plasmonic spheres at sufficently short distances [176].

In Fig. 3.6(a) we also display the extinction spectra of a gold sphere of radius 150 nm (red dashed) and a gold dimer of two such spheres separated by 4 nm (red line) for perpendicular polarization. The obtained spectra show broad resonances with a maximum comparable but smaller than for the peak values of the dielectric dimer.

3.3.2. Near-field enhancement

We study next the magnetic field enhancement $|H_{tot}|/|H_0|$ provided by the silicon dimers for perpendicular polarization. Figure 3.6 shows $|H_{tot}|/|H_0|$ in the middle of the silicon dimer for a gap distance of 4 nm and for this polarization (blue line). The peak at λ=1164 nm corresponds to the coupled magnetic resonance, where the resonant magnetic dipoles in both spheres are aligned along the dimer axis. As a consequence, Fig. 3.6 shows a relatively strong magnetic field enhancement ($\approx$ 9) in the dimer gap. This peak is spectrally broad but significantly sharper than the electric enhancement in the case of parallel polarization, which indicates that the magnetic mode might be less radiative compared to the electric mode. The sharp peak at higher energy (λ = 815 nm) is the result of the coupling between the magnetic quadrupolar resonances supported by the individual spheres, with a maximum magnetic field enhancement $\approx$ 14.

In Fig. 3.6 we also plot $|H_{tot}|/|H_0|$ (red line) for a gold dimer of the same size and gap distance under perpendicular polarization to emphasize the good performance of dielectric structures for magnetic applications. Metallic spheres do not present any considerable magnetic response (with an enhancement smaller than 1, implying weaker values than that of the incoming plane-wave).

Furthermore, Fig. 3.7 shows the electric and magnetic near-field enhancement maps calculated at the coupled magnetic resonance (λ=1164 nm) of the dimer. The field maps show an electric current loop inside the spheres [circles in Fig. 3.7(a)] and the magnetic

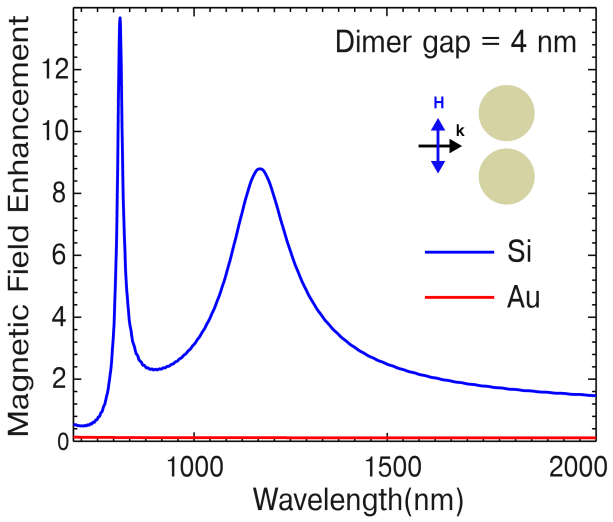

FIGURE 3.6: Magnetic near-field enhancement $|H_{tot}|/|H_0|$ spectra in the middle of a silicon (blue) and gold (red) dimer for a gap distance of 4 nm and perpendicular polarization, as shown in the inset. A strong magnetic field is found at the coupled magnetic resonance $\lambda = 1164$ nm. The narrow peak ($\lambda = 815$ nm) arises from the coupling between magnetic quadrupoles.

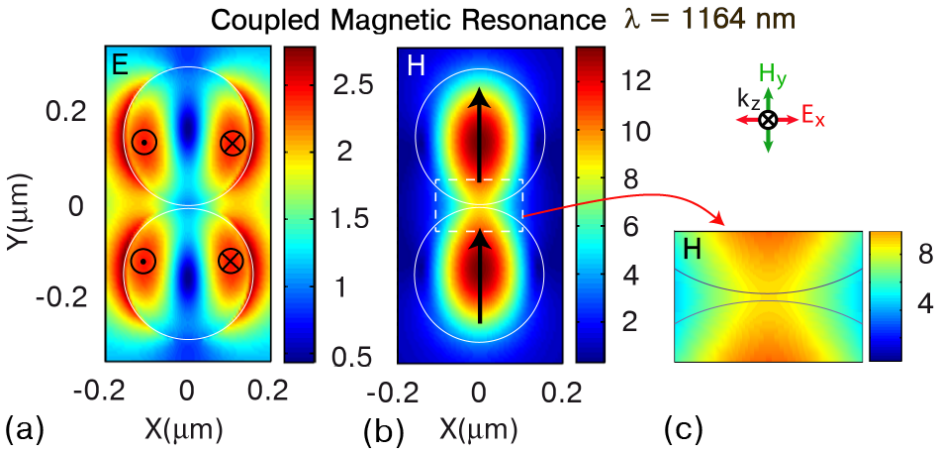

FIGURE 3.7: Electric $|E_{tot}|/|E_0|$ (a) and magnetic $|H_{tot}|/|H_0|$ (b) field enhancements for a silicon dimer of gap distance 4 nm at the coupled magnetic resonance, $\lambda = 1164$ nm. The fields are calculated in the $z = 0$ plane for perpendicular polarization of the incident field [see Fig. 3.1(b)]. The circles in (a) show the electric current loop. The arrows in (b) show the orientation (phase) of the magnetic dipoles. A zoom of the magnetic field enhancement in the dimer gap is also shown in (c).

dipoles oriented along the y direction [arrows in Fig. 3.7(b)]. The field distributions support the excitation of the coupled magnetic mode. While the magnetic field enhancement and the electric field inside the sphere are associated mostly to the excitation of magnetic dipoles in each sphere, the electric field enhancement outside the sphere is extended in a direction perpendicular to the magnetic dipoles. This component is also present due to the broad spectral nature of the electric mode that is also manifested at this wavelength.

This mode is characterized by electric dipoles oriented along the x direction and is not favourable for electric field enhancement in the gap. The magnetic field distribution in Fig. 3.7(b) is of special interest because of the strong and localized field in the antenna gap. Therefore, exciting colinear configuration of magnetic dipoles (oriented along the dimer axis) helps to extract the strong magnetic field from the inner region of the spheres to the gap. For a better view, a zoom of the magnetic field enhancement in the dimer gap is also shown in Fig. 3.7(c), giving relatively large values of magnetic field enhancement ($|\mathrm{H_{tot}}|/|\mathrm{H_0}| \approx 10$).

3.4. Electric-magnetic dipole-dipole interaction model

To understand better the origin and the evolution of the complex spectral features of the silicon dimer as a function of gap distance, a simple electrodynamical model is developed based on dipole-dipole interactions. This model is developed in collaboration with Prof. Juan José Sáenz at the Universidad Autónoma de Madrid (UAM). We focus on parallel polarization [Fig. 3.1(a)]. The model takes into account the electric-electric, magnetic-magnetic and electric-magnetic self-consistent interactions between dipoles induced in the silicon dimer, both in and out of resonance, to identify the different contributions to the total far-field response.

In the dipole-dipole model, both particles in the dimer are represented by equivalent electric and magnetic dipoles induced in each particle, as schematically shown in Fig. 3.8 for parallel polarization. Two silicon spheres of radius a are situated at $\mathbf{r}_1$ and $\mathbf{r}_2$, separated by a distance $D = \mathbf{r}_1 - \mathbf{r}_2$ along the y axis between the particle centers. The spheres are characterized by the complex dielectric function of silicon [61]. The system is immersed in an infinite homogeneous lossless medium of relative dielectric permittivity ε_1 and relative magnetic permeability μ_1.

We assume that the sub-wavelength silicon spheres can be characterized by equivalent electric and magnetic polarizabilities, $\alpha_e = (6\pi i/k^3)a_1$ and $\alpha_m = (6\pi i/k^3)b_1$ respectively, a_1 and b_1 being the electric and magnetic dipolar coefficients in the Mie expansion of the particle response [52]. This assumption is valid as long as the condition $ka \lesssim 1$ is satisfied, where $k = \sqrt{\varepsilon_1\mu_1}\omega/c$ is the wave number in the medium ($c = 1/\sqrt{\varepsilon_0\mu_0}$ is the speed of light in vacuum, ε_0 is the vacuum permittivity, μ_0 is the magnetic permeability of vacuum and ω is the angular frequency).

The total electric and magnetic fields at any point $\mathbf{r}$ are given by the sum of the incident fields $\mathbf{E}_0$ and $\mathbf{H}_0$, and the field scattered by the two dipoles ($j = 1, 2$), $\mathbf{E}_{\text{scat}}$ and $\mathbf{H}_{\text{scat}}$. The fields scattered by two electric $\mathbf{p}$ and magnetic $\mathbf{m}$ dipoles can be written as

$$\mathbf{E}_{\text{scat}}(\mathbf{r}) = \sum_{j=1,2} \left\{ \frac{k^2}{\varepsilon_0\varepsilon_1} \overleftrightarrow{\mathbf{G}}_{\text{E}}(\mathbf{r}-\mathbf{r}_j).\mathbf{p}_j + iZk^2 \overleftrightarrow{\mathbf{G}}_{\text{M}}(\mathbf{r}-\mathbf{r}_j).\mathbf{m}_j \right\}, \tag{3.1}$$

$$\mathbf{H}_{\text{scat}}(\mathbf{r}) = \sum_{j=1,2} \left\{ -i\frac{1}{Z}\frac{k^2}{\varepsilon_0\varepsilon_1} \overleftrightarrow{\mathbf{G}}_{\text{M}}(\mathbf{r}-\mathbf{r}_j).\mathbf{p}_j + k^2 \overleftrightarrow{\mathbf{G}}_{\text{E}}(\mathbf{r}-\mathbf{r}_j).\mathbf{m}_j \right\}, \tag{3.2}$$

where $\overleftrightarrow{\mathbf{G}}_{\text{E}}(\mathbf{r})$ and $\overleftrightarrow{\mathbf{G}}_{\text{M}}(\mathbf{r})$ are the free-space electric and magnetic dyadic Green's functions, respectively [177, 178] and $Z \equiv \sqrt{\mu_0\mu_1/(\varepsilon_0\varepsilon_1)}$ is the impedance of the medium. In Eq. (3.1) and (3.2) the first and second terms in the right hand side express the fields due to the electric and magnetic dipoles, respectively. From these equations, the electric and magnetic fields at any position due to an electric dipole $\mathbf{p}$ can be obtained using the respective Greens's function as [177, 178]

$$\overleftrightarrow{\mathbf{G}}_{\text{E}}(\mathbf{r}).\mathbf{p} = \left\{ \left(1 + \frac{i}{kr} - \frac{1}{k^2r^2}\right)\mathbf{p} + \left(-1 - \frac{3i}{kr} + \frac{3}{k^2r^2}\right)(\hat{\boldsymbol{e}}_r \cdot \mathbf{p})\hat{\boldsymbol{e}}_r \right\} g(r), \tag{3.3}$$

$$\overleftrightarrow{\mathbf{G}}_{\text{M}}(\mathbf{r}).\mathbf{p} = \left(\hat{\boldsymbol{e}}_r \times \mathbf{p}\right)\left(i - \frac{1}{kr}\right) g(r), \tag{3.4}$$

where $\mathbf{r}$ is the vector from the dipole to the position where the field is evaluated, $\hat{\boldsymbol{e}}_r$ and r are the corresponding unit vector and distance, respectively, and $g(r) = e^{ikr}/(4\pi r)$ is the scalar Green's function. The fields of a magnetic dipole can also be obtained in a similar way by inserting $\mathbf{m}$ instead of $\mathbf{p}$ in Eqs. (3.3) and (3.4). We notice that $\overleftrightarrow{\mathbf{G}}_{\text{M}}$ can also be written as

$$\overleftrightarrow{\mathbf{G}}_{\text{M}} \equiv \frac{1}{k}\nabla \times \overleftrightarrow{\mathbf{G}}_{\text{E}}. \tag{3.5}$$

The induced electric dipole $\mathbf{p}_j$ in sphere j at position $\mathbf{r}_j$ is proportional to the total electric field $\mathbf{E}_{\text{tot}}(\mathbf{r}_j)$ at this position, as given by the electric polarizability α_e. More

exactly,

$$\mathbf{p}_j = \varepsilon_0\varepsilon_1\alpha_e\mathbf{E}_{\rm tot}(\mathbf{r}_j), \tag{3.6}$$

and similarly for the induced magnetic dipole $\mathbf{m}_j$,

$$\mathbf{m}_j = \alpha_m\mathbf{H}_{\rm tot}(\mathbf{r}_j) \tag{3.7}$$

where α_m is the magnetic polarizability of the sphere j situated at $\mathbf{r}_j$.

The influence of the field scattered by the dipoles in one sphere on the dipoles in the neighbouring sphere is incorporated in Eqs. (3.6) and (3.7). This mutual interaction of dipoles with each other and also with the incident field results in a set of self-consistent electric and magnetic dipoles in each sphere. The actual value of the dipole moments are given by the solutions of the self-consistent equations given by

$$\mathbf{p}_1 = \varepsilon_0\varepsilon_1\alpha_e\mathbf{E}_0(\mathbf{r}_1) + \alpha_e k^2 \overleftrightarrow{\mathbf{G}}_{\rm E}(\mathbf{r}_1-\mathbf{r}_2).\mathbf{p}_2 + i\varepsilon_0\varepsilon_1\alpha_e Z k^2 \overleftrightarrow{\mathbf{G}}_{\rm M}(\mathbf{r}_1-\mathbf{r}_2).\mathbf{m}_2 \tag{3.8}$$

$$\mathbf{m}_1 = \alpha_m\mathbf{H}_0(\mathbf{r}_1) - i\frac{\alpha_m}{Z}\frac{k^2}{\varepsilon_0\varepsilon_1} \overleftrightarrow{\mathbf{G}}_{\rm M}(\mathbf{r}_1-\mathbf{r}_2).\mathbf{p}_2 + \alpha_m k^2 \overleftrightarrow{\mathbf{G}}_{\rm E}(\mathbf{r}_1-\mathbf{r}_2).\mathbf{m}_2 \tag{3.9}$$

$$\mathbf{p}_2 = \varepsilon_0\varepsilon_1\alpha_e\mathbf{E}_0(\mathbf{r}_2) + \alpha_e k^2 \overleftrightarrow{\mathbf{G}}_{\rm E}(\mathbf{r}_2-\mathbf{r}_1).\mathbf{p}_1 + i\varepsilon_0\varepsilon_1\alpha_e Z k^2 \overleftrightarrow{\mathbf{G}}_{\rm M}(\mathbf{r}_2-\mathbf{r}_1).\mathbf{m}_1 \tag{3.10}$$

$$\mathbf{m}_2 = \alpha_m\mathbf{H}_0(\mathbf{r}_2) - i\frac{\alpha_m}{Z}\frac{k^2}{\varepsilon_0\varepsilon_1} \overleftrightarrow{\mathbf{G}}_{\rm M}(\mathbf{r}_2-\mathbf{r}_1).\mathbf{p}_1 + \alpha_m k^2 \overleftrightarrow{\mathbf{G}}_{\rm E}(\mathbf{r}_2-\mathbf{r}_1).\mathbf{m}_1 \tag{3.11}$$

On the right hand side of Eq. (3.8) the first term describes the response of the first sphere to the electric field of the incident plane-wave. The second and third terms correspond to the electric field produced by the electric and magnetic dipoles induced in the second sphere, respectively, at the position of the first sphere. Similarly in Eq. (3.9) on the right hand side, the first term describes the response of the first sphere to the magnetic field of the incident plane-wave. The second and third terms correspond to the magnetic field produced by the electric and magnetic dipoles induced in the second sphere, respectively, at the position of the first sphere. Equations (3.10) and (3.11) follow the same logic for the induced electric and magnetic dipole moments in the second sphere, respectively.

3.4.1. Far-field calculation

3.4.1.1. Self-consistent dipoles

We now proceed to obtain the expressions for the self-consistent electric and magnetic dipole moments when the dimer is illuminated with parallel polarization. In Fig. 3.8 we schematically show the self-consistent dipoles induced at each particle of the dimer. Particle 1 and particle 2 are located at $\mathbf{r}_1 = (0, +D/2, 0)$ and $\mathbf{r}_2 = (0, -D/2, 0)$ respectively. The plane-wave is incident along the z direction with electric field polarized along the y axis and magnetic field along the x axis. According to the polarization of the incident plane-wave, an electric dipole is induced in each sphere along the y direction, to be called p_{1y} and p_{2y}, together with magnetic dipoles along the x direction, m_{1x} and m_{2x}. In addition to these dipoles, the induced magnetic dipoles in each sphere induce a new electric dipole in the neighbouring sphere along the z axis. These new dipoles represented as p_{1z} and p_{2z}, oriented along the direction of the incident radiation, cannot be directly induced by the incident illumination and therefore they are referred to as secondary dipoles.

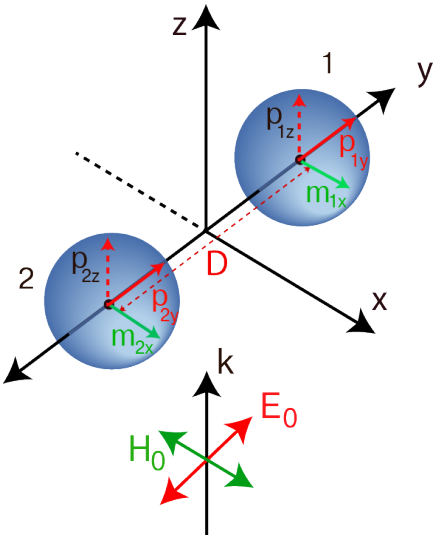

FIGURE 3.8: Schematic representation of the self-consistent dipoles used in the modelling of the electromagnetic response of the silicon particle dimer for parallel illumination. The red and green arrows in each particle represent respectively, the electric (p_{1y} and p_{2y}) and magnetic (m_{1x} and m_{2x}) dipoles directly induced by the incident plane-wave along the direction of the electric and magnetic fields of the plane-wave. The electric dipole p_{1z} along the z direction represented by dashed red arrow in sphere 1 is induced due to the presence of the magnetic dipole m_{2x} in sphere 2, and vice versa for p_{2z}.

To simplify Eqs. (3.8) - (3.11) for this polarization, we first write the expression for the incident electric $\mathbf{E}_0(\mathbf{r})$ and magnetic $\mathbf{H}_0(\mathbf{r})$ fields as

$$\mathbf{E}_0(\mathbf{r}) = \mathrm{E}_0 e^{ikz}\hat{\mathbf{e}}_y, \tag{3.12}$$

$$\mathbf{H}_0(\mathbf{r}) = -\frac{\mathrm{E}_0}{Z}e^{ikz}\hat{\mathbf{e}}_x \equiv -\mathrm{H}_0 e^{ikz}\hat{\mathbf{e}}_x, \tag{3.13}$$

where $\hat{\mathbf{e}}_x$, $\hat{\mathbf{e}}_y$ and $\hat{\mathbf{e}}_z$ are the unit vectors along the x, y and z directions, respectively. Furthermore, the induced dipoles in particle 1 can be written as $\mathbf{p}_1 = p_{1y}\hat{\mathbf{e}}_y + p_{1z}\hat{\mathbf{e}}_z$ and $\mathbf{m}_1 = m_{1x}\hat{\mathbf{e}}_x$ and correspondingly for the second particle, which allows us to write Eqs. (3.3) and (3.4) for the fields induced by the dipoles in particle 1 at the position of particle 2 as

$$\overleftrightarrow{\mathbf{G}}_{\mathrm{E}}(\mathbf{r}_2-\mathbf{r}_1)\cdot m_{1x}\hat{\boldsymbol{e}}_x = \left(1+\frac{i}{kD}-\frac{1}{k^2D^2}\right)g(D)m_{1x}\hat{\boldsymbol{e}}_x \equiv -g_{xx}m_{1x}\hat{\boldsymbol{e}}_x, \tag{3.14}$$

$$\overleftrightarrow{\mathbf{G}}_{\mathrm{M}}(\mathbf{r}_2-\mathbf{r}_1)\cdot m_{1x}\hat{\boldsymbol{e}}_x = -\left(i-\frac{1}{kD}\right)g(D)m_{1x}\hat{\boldsymbol{e}}_z \equiv g_{zx}m_{1x}\hat{\boldsymbol{e}}_z, \tag{3.15}$$

$$\overleftrightarrow{\mathbf{G}}_{\mathrm{E}}(\mathbf{r}_2-\mathbf{r}_1)\cdot p_{1y}\hat{\boldsymbol{e}}_y = \left(-\frac{2i}{kD}+\frac{2}{k^2D^2}\right)g(D)p_{1y}\hat{\boldsymbol{e}}_y \equiv g_{yy}p_{1y}\hat{\boldsymbol{e}}_y, \tag{3.16}$$

$$\overleftrightarrow{\mathbf{G}}_{\mathrm{M}}(\mathbf{r}_2-\mathbf{r}_1)\cdot p_{1y}\hat{\boldsymbol{e}}_y = 0, \tag{3.17}$$

$$\overleftrightarrow{\mathbf{G}}_{\mathrm{E}}(\mathbf{r}_2-\mathbf{r}_1)\cdot p_{1z}\hat{\boldsymbol{e}}_z = \left(1+\frac{i}{kD}-\frac{1}{k^2D^2}\right)g(D)p_{1z}\hat{\boldsymbol{e}}_z \equiv -g_{xx}p_{1z}\hat{\boldsymbol{e}}_z, \tag{3.18}$$

$$\overleftrightarrow{\mathbf{G}}_{\mathrm{M}}(\mathbf{r}_2-\mathbf{r}_1).p_{1z}\hat{\boldsymbol{e}}_z = \left(i-\frac{1}{kD}\right)g(D)p_{1z}\hat{\boldsymbol{e}}_x \equiv -g_{zx}p_{1z}\hat{\boldsymbol{e}}_x, \tag{3.19}$$

where for simplicity we use the terms g_{xx}, g_{zx} and g_{yy}. Taking advantage of the symmetry of the system, the fields at position $\mathbf{r}_1$ can be obtained using the following relationships:

$$\overleftrightarrow{\mathbf{G}}_{\mathrm{E}}(\mathbf{r}_1-\mathbf{r}_2) = \overleftrightarrow{\mathbf{G}}_{\mathrm{E}}(\mathbf{r}_2-\mathbf{r}_1), \tag{3.20}$$

$$\overleftrightarrow{\mathbf{G}}_{\mathrm{M}}(\mathbf{r}_1-\mathbf{r}_2) = -\overleftrightarrow{\mathbf{G}}_{\mathrm{M}}(\mathbf{r}_2-\mathbf{r}_1), \tag{3.21}$$

and we finally obtain

$$p_{1y} = \varepsilon_0\varepsilon_1\alpha_e\mathrm{E}_0 + \alpha_e k^2 g_{yy}p_{2y}, \tag{3.22}$$

$$p_{2y} = \varepsilon_0\varepsilon_1\alpha_e\mathrm{E}_0 + \alpha_e k^2 g_{yy}p_{1y}, \tag{3.23}$$

$$p_{1z} = -\alpha_e k^2 g_{xx}p_{2z} + i\varepsilon_0\varepsilon_1\alpha_e Z k^2 g_{zx}m_{2x}, \tag{3.24}$$

$$p_{2z} = -\alpha_e k^2 g_{xx}p_{1z} - i\varepsilon_0\varepsilon_1\alpha_e Z k^2 g_{zx}m_{1x}, \tag{3.25}$$

$$m_{1x} = -\frac{\alpha_m}{Z}\mathrm{E}_0 + i\frac{\alpha_m}{Z}\frac{k^2}{\varepsilon_0\varepsilon_1}g_{zx}p_{2z} - \alpha_m k^2 g_{xx}m_{2x}, \tag{3.26}$$

$$m_{2x} = -\frac{\alpha_m}{Z}\mathrm{E}_0 - i\frac{\alpha_m}{Z}\frac{k^2}{\varepsilon_0\varepsilon_1}g_{zx}p_{1z} - \alpha_m k^2 g_{xx}m_{1x}. \tag{3.27}$$

In Eqs. (3.22) and (3.23) the first term on the right hand side corresponds to the electric dipole induced by the incident electric field and the second term is the contribution due to the electric dipole in the neighbouring sphere. Therefore the electric dipoles along the y direction are coupled to each other. Equations (3.24) and (3.25) describe how the electric dipole in the z direction depends on two of the dipoles in the other sphere, the electric dipole along z and the magnetic dipole along x. Equations (3.26) and (3.27) reveal that the magnetic dipoles, oriented along the x direction, are the result of three contributions. The first term comes from the incident electric field, the middle term is induced by the electric dipole oriented along z in the neighbouring sphere and the last term is produced by the neighbouring magnetic dipole along the x direction.

Now we define the dressed polarizabilities $\tilde{\alpha}$ as

$$\tilde{\alpha}_{ey} \equiv \frac{\alpha_e}{1-\alpha_e k^2 g_{yy}}, \qquad \tilde{\alpha}_{ez} \equiv \frac{\alpha_e}{1-\alpha_e k^2 g_{xx}}, \qquad \tilde{\alpha}_{mx} \equiv \frac{\alpha_m}{1+\alpha_m k^2 g_{xx}}. \tag{3.28}$$

From Eqs. (3.22) - (3.27) we obtain

$$p_{1y} = \frac{\varepsilon_0\varepsilon_1\alpha_e(1+\alpha_e k^2 g_{yy})\mathrm{E}_0}{1-\alpha_e^2 k^4 g_{yy}^2} = \varepsilon_0\varepsilon_1\tilde{\alpha}_{ey}\mathrm{E}_0 = p_{2y}, \tag{3.29}$$

$$p_{1z} = i\varepsilon_0\varepsilon_1\tilde{\alpha}_{ez}Zk^2 g_{zx}m_{2x} = -p_{2z}, \tag{3.30}$$

$$m_{1x} = -\frac{\tilde{\alpha}_{mx}}{Z}\mathrm{E}_0 + i\frac{\tilde{\alpha}_{mx}}{Z}\frac{k^2}{\varepsilon_0\varepsilon_1}g_{zx}p_{2z} = m_{2x}. \tag{3.31}$$

Eqs. (3.30) and (3.31) can be also expressed as

$$p_{1z} = -p_{2z} = -i\varepsilon_0\varepsilon_1\mathrm{E}_0\frac{\tilde{\alpha}_{mx}\tilde{\alpha}_{ez}k^2 g_{zx}}{1-\tilde{\alpha}_{mx}\tilde{\alpha}_{ez}k^4 g_{zx}^2} \equiv -i\varepsilon_0\varepsilon_1\mathrm{E}_0\tilde{\alpha}_{e-m} \tag{3.32}$$

$$m_{1x} = m_{2x} = -\frac{\tilde{\alpha}_{mx}}{Z}\mathrm{E}_0 - \left(\tilde{\alpha}_{e-m}k^2 g_{zx}\right)\frac{\tilde{\alpha}_{mx}}{Z}\mathrm{E}_0, \tag{3.33}$$

which allows to express the relation between p_{1z} and m_{2x} via $\tilde{\alpha}_{e-m}$ given by

$$\tilde{\alpha}_{e-m} = i\varepsilon_0\varepsilon_1\mathrm{E}_0\frac{\tilde{\alpha}_{mx}\tilde{\alpha}_{ez}k^2 g_{zx}}{1-\tilde{\alpha}_{mx}\tilde{\alpha}_{ez}k^4 g_{zx}^2}. \tag{3.34}$$

Equations (3.28), (3.29) and (3.32) - (3.34) summarize the self-consistent calculation of induced dipoles schematically shown in Fig. 3.8. From Eq. (3.29), the electric dipoles p_{1y} and p_{2y} only couple to each other, via the dressed polarizability $\tilde{\alpha}_{ey}$. The magnetic

dipoles are similarly coupled via Eq. (3.33). Moreover, the electric p_{1z} and p_{2z} and magnetic m_{1x} and m_{2x} dipoles are coupled to each other by $\tilde{\alpha}_{e-m}$ in Eq. (3.34).

3.4.1.2. Extinction

In order to evaluate the far-field response of the dimer, we now proceed to derive the expression for the extinction cross section. The electric $\mathbf{E}_{\text{scat}}(\mathbf{r})$ and magnetic $\mathbf{H}_{\text{scat}}(\mathbf{r})$ fields scattered by a small object situated at $\mathbf{r}_1$, at a point $\mathbf{r}$ far away from the object, can be written in terms of the vectorial scattering amplitude dyadic $\boldsymbol{\mathcal{F}}(\mathbf{k}_{\text{in}}, \mathbf{k}_{\text{out}})$ [179], which is defined as the function that verifies

$$\begin{aligned} \lim_{r\to\infty} \mathbf{E}_{\text{scat}}(\mathbf{r}-\mathbf{r}_1) &\approx E_0 \frac{e^{ikr}}{r} \boldsymbol{\mathcal{F}}(\mathbf{k}_{\text{in}}, \mathbf{k}_{\text{out}}) \cdot \hat{\boldsymbol{e}}_{\text{in}}, \\ \lim_{r\to\infty} \mathbf{H}_{\text{scat}}(\mathbf{r}-\mathbf{r}_1) &\approx \frac{1}{kZ} (\mathbf{k}_{\text{out}} \times \mathbf{E}_{\text{scat}}), \end{aligned} \tag{3.35}$$

where $\mathbf{k}_{\text{in}}$ and $\hat{\boldsymbol{e}}_{\text{in}}$ are the wave vector and the polarization direction of the incident field, respectively, and $\mathbf{k}_{\text{out}}$ is the wave vector of the scattered field along $\mathbf{r}-\mathbf{r}_1$. The scattering cross section σ_{scat}, obtained by integrating over all scattered plane-waves, can be expressed in terms of the amplitude dyadic as

$$\sigma_{\text{scat}} = \int d\Omega_{\text{out}} \left| \boldsymbol{\mathcal{F}}(\mathbf{k}_{\text{in}}, \mathbf{k}_{\text{out}}) . \hat{\boldsymbol{e}}_{\text{in}} \right|^2 . \tag{3.36}$$

The extinction cross section σ_{ext} is related to the imaginary part of $\boldsymbol{\mathcal{F}}(\mathbf{k}_{\text{in}}, \mathbf{k}_{\text{out}})$ in the forward direction ($\mathbf{k}_{\text{in}} = \mathbf{k}_{\text{out}}$) as

$$\sigma_{\text{ext}} = \frac{4\pi}{k} \text{Im} \left\{ \hat{\boldsymbol{e}}_{\text{in}} \cdot \boldsymbol{\mathcal{F}}(\mathbf{k}_{\text{in}}, \mathbf{k}_{\text{in}}) \cdot \hat{\boldsymbol{e}}_{\text{in}} \right\}, \tag{3.37}$$

which is referred to as the optical theorem. In the case of the dimer, the scattered fields and thus $\boldsymbol{\mathcal{F}}(\mathbf{k}_{\text{in}}, \mathbf{k}_{\text{out}})$ are given by the sum of the contributions of the field scattered by the electric and magnetic dipoles, expressed in Eqs. (3.1) and (3.2). Taking into account that only terms in $1/r$ in Eqs. (3.3) and (3.4) remain in the far-field and that we are considering $\hat{\boldsymbol{e}}_{\text{in}} = \hat{\boldsymbol{e}}_y$, $\mathbf{k}_{\text{in}} = k\hat{\boldsymbol{e}}_z$ and $\mathbf{r}_1 = -\mathbf{r}_2 = (D/2)\hat{\boldsymbol{e}}_y$, we write

$$\begin{aligned} k^2 \overleftrightarrow{\mathbf{G}}_{\text{E}}(\mathbf{r}-\mathbf{r}_j)\mathbf{p}_j &\approx \frac{e^{ikr}}{4\pi r} \left\{ k^2 \mathbf{p}_j - (\mathbf{k}_{\text{out}} \cdot \mathbf{p}_j)\mathbf{k}_{\text{out}} \right\} e^{-i\mathbf{k}_{\text{out}}\cdot\mathbf{r}_j}, \\ &= \frac{e^{ikr}}{4\pi r} \left\{ (\mathbf{k}_{\text{out}} \times \mathbf{p}_j) \times \mathbf{k}_{\text{out}} \right\} e^{-i\mathbf{k}_{\text{out}}\cdot\mathbf{r}_j}, \end{aligned} \tag{3.38}$$

and

$$k^2 \overleftrightarrow{\mathbf{G}}_{\mathrm{M}}(\mathbf{r}-\mathbf{r}_j)\mathbf{p}_j \approx ik\frac{e^{ikr}}{4\pi r}\left\{\mathbf{k}_{\mathrm{out}}\times\mathbf{p}_j\right\}e^{-i\mathbf{k}_{\mathrm{out}}\cdot\mathbf{r}_j}, \tag{3.39}$$

where $j = 1, 2$ refers to the first or second particle, respectively.

Adding all different contributions from both spheres, using Eq. (3.37) - (3.39) we finally arrive at

$$\sigma_{\mathrm{ext}} = \frac{4\pi}{k\mathrm{E}_0}\mathrm{Im}\left(2\frac{k^2}{4\pi\varepsilon_0\varepsilon_1}p_{1y} - 2Z\frac{k^2}{4\pi}m_{1x}\right), \tag{3.40}$$

$$= 2k\ \mathrm{Im}\left\{\tilde{\alpha}_{ey} + \tilde{\alpha}_{mx} + \left(\tilde{\alpha}_{e-m}k^2 g_{zx}\right)\tilde{\alpha}_{mx}\right\}. \tag{3.41}$$

The first and the second terms in the right hand side of Eq. (3.41) are associated to the excitation of the electric dipoles along the y axis (electric-electric contribution) or the magnetic dipoles along the x axis (magnetic-magnetic contribution), respectively. The third term corresponds to the coupling between the secondary electric dipoles oriented along the z direction and the magnetic dipoles. Notice that p_{1z} and p_{2z} do not scatter along $\mathbf{k}_{\mathrm{in}}$, $\boldsymbol{\mathcal{F}}(\mathbf{k}_{\mathrm{in}}, \mathbf{k}_{\mathrm{in}}) = 0$, but they affect σ_{ext} via its coupling with the magnetic dipoles.

We now apply Eq. (3.41) to obtain the far-field response of the silicon dimer of two 150 nm radius spheres under parallel polarization (Fig. 3.1). Figure 3.9 shows the resulting extinction coefficient for different gap distances. The model reproduces well the spectral features corresponding to the coupling between the electric and magnetic dipolar resonances in Fig. 3.2(a), which were obtained for decreasing gap distance from the full electrodynamical calculations. The narrow peak corresponding to the quadrupolar mode in the low-wavelength region (observed in the full calculation) is not present in Fig. 3.9, because the model used to derive Eq. (3.41) considers only dipole-dipole interactions in the system.

The main aim of our analytical model is to identify the contribution from the different interactions between the electric and magnetic dipoles to the total optical response of the dimer. Thus, besides the total extinction shown in Fig. 3.9 we can also obtain the contribution to the extinction from the electric-electric, magnetic-magnetic and electric-magnetic interactions in the dimer, as given by the three terms in Eq. (3.41).

In Fig. 3.10 (a) and (b), we show these different contributions for 10 nm and 50 nm gap distances respectively. In both cases, the total extinction from the dipolar model (blue solid line) and calculated by solving the full electrodynamical equations using FDTD

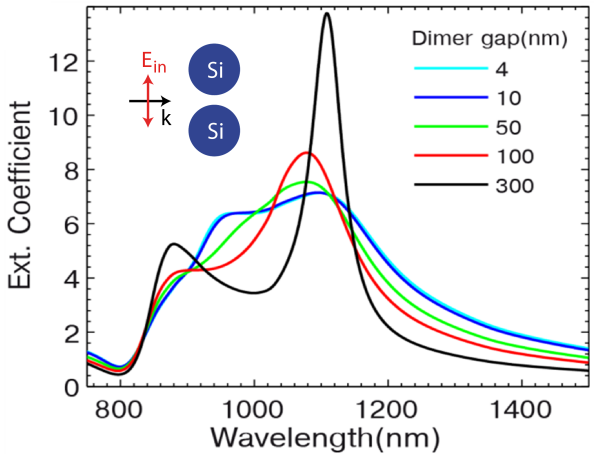

FIGURE 3.9: Extinction spectra of a silicon dimer of 150 nm sphere radius for parallel polarization of the incident field, as shown in the inset, calculated for different dimer gap distances using the dipole-dipole model.

software (blue dashed line) are plotted for comparison. As discussed, the total extinction calculated using the model shows good agreement, for both small and large gap distances, except for the small wavelength region where the quadupolar mode appears.

The red dashed curve in Fig. 3.10(a) and (b) gives the contribution to the extinction by the term proportional to $\tilde{\alpha}_{ey}$ [first term in Eq. (3.41)]. This contribution presents a peak around $\lambda = 900$ nm [clearly seen in Fig. 3.10(b)] for the two gap distances, which can thus be identified as arising due to the interacting electric dipoles p_{1y} and p_{2y} along the y direction. The green dashed curves represent the contribution from the term proportional to the dressed polarizability $\tilde{\alpha}_{mx}$ describing the interaction between the magnetic dipoles m_{1x} and m_{2x} [second term in Eq. (3.41)]. This interaction results in the spectral peak observed around $\lambda = 1100$ nm for both gap distances. The black curve, given by the final term in Eq. (3.41), is a function of $\tilde{\alpha}_{e-m}$, and thus of the coupling between electric and magnetic dipoles oriented along the z and the x directions, respectively. This contribution leads to a peak at $\lambda = 964$ nm for 10 nm gap distance [Fig. 3.10(a)], which disappears as the dimer gap is increased [Fig. 3.10(b)]. For small gap distances [Fig. 3.10(a)], the strength of the near-field of, for example, m_{1x} at the position of the second sphere is strong enough to induce p_{2z}. Therefore we refer to the gap distances smaller than 50 nm as strong interaction regime. As the dimer gap increases, this near-field interaction becomes weak in comparison to the tail of the peak at $\lambda = 1085$ nm, resulting in the disappearance of the peak at $\lambda = 964$ nm [Fig. 3.10(b)]. Therefore, we identify the situation with a dimer gap larger than 50 nm as a weak interaction regime.

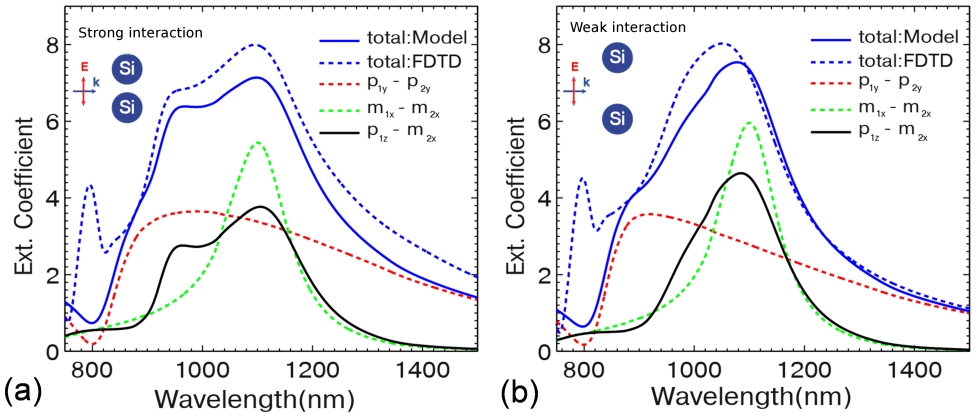

FIGURE 3.10: Extinction spectra of a silicon dimer particle radius 150 nm, calculated using the dipole-dipole model (blue solid line) for strong (a) and weak (b) interaction regimes, corresponding to gap separations of 10 nm and 50 nm, respectively. The model allows to study the interactions responsible for the far-field spectra in Fig. 3.2(a) by separating the contributions of each interactions. The red (green) dashed line gives the contributions from the electric-electric $p_{1z} - p_{2z}$ (magnetic-magnetic $m_{1x} - m_{2x}$) dipolar coupling, respectively. The black solid lines give the electric-magnetic dipolar contribution due to the coupling between magnetic dipoles and the secondary electric dipoles induced by the magnetic dipoles. The blue dashed lines are the extinction spectra obtained from full electrodynamical calculations shown in Fig. 3.2(a).

Finally, we discuss the blueshift of the magnetic dipolar peak as the dimer gap is decreased below 50 nm, which is observed in the full electrodynamical calculations (Fig. 3.1) and reproduced within the dipole-dipole model (Fig. 3.9). For large gap distances, the energy received by the magnetic dipoles is radiated to the far-field via scattering. When the gap distance is reduced below 50 nm, in addition to this scattering, part of the energy of each magnetic dipole is transferred to the secondary electric dipole in the neighbouring sphere, which is then radiated by the electric dipoles. Therefore this coupling between the magnetic dipoles and the secondary electric dipoles introduces an additional mechanism of interaction for the system of dipoles, which in turn results in the reduction of the total energy of the magnetic dipoles. This reduction in the energy is the cause of the redshift of the magnetic dipolar peak as the dimer gap is decreased below 50 nm.

3.5. Summary

In this chapter we presented our study on the electromagnetic response of low-loss high-refractive index dielectric dimer antennas made of two identical silicon spheres. The intensity of scattering from the dimer is comparable to that of plasmonic antennas.

Moreover, by choosing proper illumination condition, strong enhancement of electric and magnetic fields can be achieved. When plane-waves with electric field polarized parallel to the dimer axis are used for illumination, a strong electric field enhancement is observed in the gap, which enables to use the silicon dimer for field enhanced spectroscopy. Even though the electric field enhancement in this system is small compared to standard plasmonic antennas, the low loss of dielectric antennas can be an advantage compared to their metallic counterparts for field enhancement and sensing of emitters that show magnetic transitions, or for spectroscopy of magnetic dipolar moments. A more distinctive aspect of the dielectric dimer antenna is observed when the incident illumination shows magnetic field parallel to the dimer axis, as the resulting strong magnetic field at the gap facilitates efficient coupling of magnetic emitters with the dielectric antennas [30], for example, for spectroscopy of magnetic dipole moments.

In order to better analyze the complex spectra presented by the dimer antenna, we also developed a dipole-dipole interaction model. Using this model we identified the different electric-electric, magnetic-magnetic and electric-magnetic dipole contributions to the total far-field response of the dimer under parallel illumination, as a function of the dimer gap distance.

These results can help in the path towards further understanding of the electric and magnetic resonances in sub-wavelength dielectric structures. The enhancement of the magnetic field, together with directional scattering properties [29, 80, 88] and low loss, make dielectric antennas a promising counterpart to plasmonic antennas for nanophotonic applications.

Chapter 4

Topological Insulator Plasmonics

In Chapters 2 and 3, we considered plasmons in three dimensional materials. Interestingly, two-dimensional atomic systems can also support plasmon oscillations. Possibly, the most studied example of such systems is graphene [33–35, 180]. Plasmons in graphene result from the collective oscillation of the 2D Dirac electrons, and therefore are often referred to as Dirac plasmons [181]. The Dirac plasmons behave as free charges in a positive background, similar to the description of the Drude model of plasmons in a metal. These 2D plasmons show very interesting features in optics like strong confinement and long propagation distance[33]. A significant advantage of graphene plasmons with respect to usual plasmons in metallic systems is their spectral tunability by intrinsic doping of the material or by applying external bias [34, 35, 182]. The frequency of graphene plasmons extends from the optical to the terahertz range of the electromagnetic spectrum.

Three-dimensional topological insulators are a different class of novel materials that also support two-dimensional Dirac plasmons [183–188]. The gap energy of the insulating bulk states corresponds to infrared frequencies, so that the bulk is transparent for low energy radiation [187, 189]. The two dimensional distribution of Dirac electrons making plasmon excitation possible is found at the surfaces of the bulk material. Bi_2Se_3 and Bi_2Te_3 are typical examples of three-dimensional topological insulators [186]. There are also two-dimensional topological insulators with one-dimensional edge states [128]. As we do not consider two-dimensional topological insulators, we often refer to our system in the following simply as topological insulator.

The 2D conducting states determine the electronic and optical properties of topological insulators. Recent experiments have demonstrated [190] the presence of the surface Dirac

Plasmons in topological insulators in the therahertz range of the spectrum. Similar to the case of graphene, theoretical studies show that plasmons in topological insulators are also tightly confined and show long propagation distance (several wavelengths) [191]. The carrier concentration of the surface states in topological insulators can also be controlled via intrinsic doping or by applying an external voltage, allowing for spectral tuning of the plasmons.

A key property of topological insulators is that, in contrast with other 2D systems such as graphene, the electrons moving in a given direction have spin with well defined orientation. Surface plasmons in topological insulators are thus associated with a collective oscillation of spins, called spin plasmons [128, 183, 184, 192, 193]. Notably, as we will discuss in detail, hybridized plasmons in thin-film topological insulators are characterized by having either charge or spin effective nature, making in principle possible to manipulate separately either spin or charge [194].

In this chapter we discuss how to control the nature of the excited thin-film topological plasmons. We use a localized electromagnetic source to excite propagating plasmons in thin films, and either localized sources or plane-waves to couple with localized modes in thin disks. We are thus able to demonstrate that we can control the spin and the charge properties of plasmons in topological insulators by properly choosing the geometry and illumination conditions. It is also possible to further tune the response by applying a voltage, making topological insulators a versatile material for spintronics and optoelectronics.

We describe the properties of the thin-films and the disks to be studied in Subsection 4.1.1, followed by the theoretical approach combining many-body theory and classical electrodynamics, in Subsections 4.1.2 and 4.1.3. Many-body theory calculations are performed to obtain the 2D conductivity, σ, resulting from the 2D Dirac electrons in the surface of topological insulators. This conductivity is then used in classical electrodynamical calculations to obtain the optical response. We discuss in Section 4.2 the excitation of propagative Dirac plasmons in semi-inifinite surfaces by an electric dipole, as well as the excitation of acoustic and optical modes in thin films, which show effective spin and effective charge character, respectively. Section 4.3 discusses the far-field and near-field response of acoustic and optical localized plasmon modes excited by a plane-wave or a dipole on a topological insulator disk.

4.1. System and methods

4.1.1. Geometries

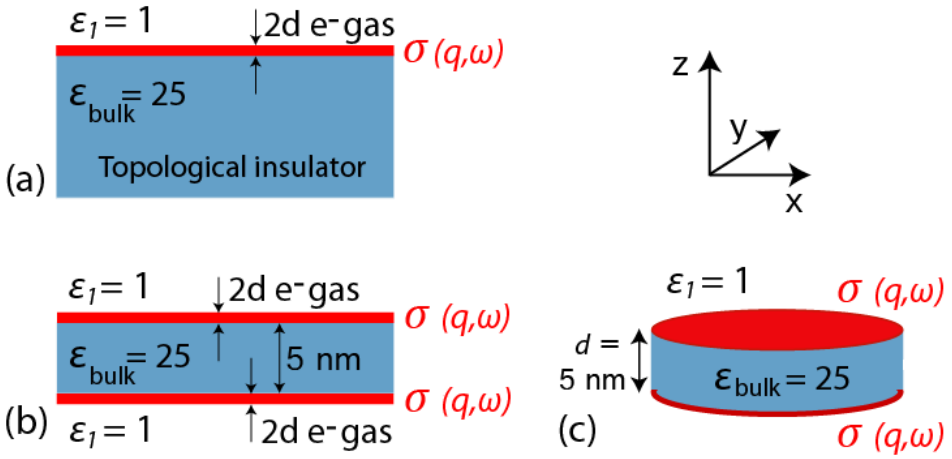

FIGURE 4.1: Schematic of the structures considered. (a) Semi-infinite topological insulator substrate supporting a 2D electron gas at the interface with the surrounding vacuum, (b) an infinite topological insulator film of thickness d=5 nm (suspended in vacuum) with two interacting 2D electron layers at both interfaces and (c) a finite topological insulator thin disk of thickness d=5 nm surrounded by vacuum with two interacting 2D electron layers at the top and bottom interfaces. The 2D layers (in red) are treated as an in-plane conductivity $\sigma(q,\omega)$. We consider Bi_2Se_3 topological insulator with relative dielectric permittivity of the bulk, ε_{bulk}=25. The center of the disk is at (0,0,0), with central horizontal plane at z=0. The top interfaces in (a) and (b) correspond to z=0. The different directions are indicated at the top right of the figure.

Figure 4.1 shows the schematics of the systems considered, illuminated at vacuum wavelength λ (angular frequency ω). We study the optical response for three different topological insulator systems: a semi-infinite substrate, an infinite thin-film and a finite thin disk. The semi-infinite topological insulator in Fig. 4.1(a) supports a 2D electron gas system at the interface between the topological insulator and the outside vacuum ($\varepsilon_1 = 1$). In the case of the infinite thin-film [Fig. 4.1(b)] and thin disks [Fig. 4.1(c)] made of topological insulator, we need to consider two 2D electron systems [characterized by $\sigma(q,\omega)$], which interact electromagnetically, at each interface (top and bottom) with the surrounding medium. The flat surfaces of the film and the disk are perpendicular to the z direction and parallel to the $x-y$ plane (see axes in the inset). z=0 is defined at the interface of the substrate for the semi-infinite situation, at the top interface of the film and at the central plane (parallel to the flat interfaces) of the disks. The latter are centered at (0,0,0). The optical response of the 2D electron layer is treated as

an in-plane conductivity $\sigma(q,\omega)$ calculated using many body theory (Subsection 4.1.2). $\sigma(q,\omega)$ corresponds to the conductivity experienced by an incoming plane-wave of parallel wave-vector q and angular frequency ω. σ is a function of q to account for the non-local effects due to the dependence of the induced polarization at a given position on the electric field at surrounding positions [195].

In this work we consider Bi_2Se_3 as the topological insulator, surrounded by vacuum, but the concepts and the results presented here should be valid for other materials as well. The Fermi energy of the 2D system is chosen to be E_F=250 meV, unless otherwise specified. The bulk dielectric constant of the topological insulator is taken as ε_{bulk}=25, which is a reasonable approximation for Bi_2Se_3 in the THz region [196, 197].

4.1.2. Many-body calculations

In the electrodynamic calculations, the in-plane conductivity σ is derived from the response function of the 2D system using many-body theory. The many-body theory calculations of the 2D electron layers are performed by our collaborator Ilya Nechaev at the Donostia International Physics Center in Donostia-San Sebastián. Unless otherwise stated, atomic units are used throughout this subsection, i.e., $e^2 = \hbar = m_e = 1$, where e is the electronic charge, $\hbar$ is the reduced plank constant and m_e is the mass of electron. The q and ω dependent conductivity $\sigma(q,\omega)$ follows

$$\sigma(q,\omega) = -i\omega \, \frac{\chi^0_\tau(q,\omega)}{q^2}, \tag{4.1}$$

$\chi^0_\tau(q,\omega)$ being the non-interacting response function of a 2D layer defined in the relaxation-time approximation as [198]

$$\chi^0_\tau(q,\omega) = \frac{(1+i/\omega\tau)\,\chi^0(q,\omega+i/\tau)}{1+(i/\omega\tau)\chi^0(q,\omega+i/\tau)/\chi^0(q,0)}, \tag{4.2}$$

where τ is the relaxation time, which we choose as τ = 500 fs [199–202]. Within the random phase approximation, the response function $\chi^0(q,\omega)$ has the same expression as in the case of doped graphene [203], but without degeneracy neither in valley nor in spin.

$$\chi^0(q,\omega) = \chi^0_{intrinsic}(q,\omega) + \delta\chi^0_\mu(q,\omega), \tag{4.3}$$

where

$$\chi^0_{intrinsic}(q,\omega) = -i\pi\frac{F(q,\omega)}{v_F^2}, \tag{4.4}$$

$$\begin{aligned}\delta\chi^0_\mu(q,\omega) = &-\frac{\mu}{2\pi v_F^2} + \frac{F(q,\omega)}{v_F^2}\left\{G\left(\frac{\omega+2\mu}{v_F q}\right) - \theta\left(\frac{2\mu-\omega}{v_F q} - 1\right)\right. \\ &\left.\left[G\left(\frac{2\mu-\omega}{v_F q}\right) - i\pi\right] - \theta\left(\frac{\omega-2\mu}{v_F q} + 1\right) G\left(\frac{\omega-2\mu}{v_F q}\right)\right\}\end{aligned} \tag{4.5}$$

with $F(q,\omega) = \frac{1}{16\pi}\frac{v_F^2 q^2}{\sqrt{\omega^2 - v_F^2 q^2}}$, $G(x) = x\sqrt{x^2-1} - ln(x+\sqrt{x^2-1})$ and θ the step function. v_F is the Fermi velocity and μ is the chemical potential. We consider temperature T=0, so that $\mu = E_F$.

For our results in the following sections, we will use the σ calculated for a single 2D electron layer, and incorporate the electromagnetic coupling between the two 2D layers in thin-films and disks via the classical calculations described in the following subsection. Nonetheless, the many-body calculations can also be directly extended to obtain the dispersion relationship of N coupled 2D electron subsystems. These results will be useful to check the dispersion relationship obtained through the electrodynamical calculations (method described in Subsection 4.1.3) shown in Figs. 4.3 and 4.5. We consider that the 2D layers are far enough from each other to neglect inter-system transitions, but are close enough to take into account the Coulomb interaction between them. Each $i-$th two-dimensional subsystem is localized in the vertical z-direction and surrounded by a medium with a certain dielectric constant. The localization is characterized by $|\lambda_i(z)|^2$, which for the $i-$th 2D-subsystem takes the following form:

$$|\lambda_i(z)|^2 = \frac{2}{h_i}\sin^2\left(\frac{\pi(z_i^0 - z)}{h_i}\right)\theta(h_i - (z_i^0 - z))\theta(z_i^0 - z), \tag{4.6}$$

where h_i is the width in the z direction used to model each (quasi)2D subsystem for the calculation of the Coulomb coupling and z_i^0 sets the upper plane of the 2D electron system (see Fig. 4.2). We use thickness $h = 8\mathring{A}$.

If we consider first the non-interacting response function χ^0_τ of the whole 3D system, it reads as

$$\chi^0_\tau(\mathbf{q},\omega;z,z') = \sum_{i=1}^{N}|\lambda_i(z)|^2\chi^0_{\tau i}(\mathbf{q},\omega)|\lambda_i(z')|^2, \tag{4.7}$$

where $\chi^0_{\tau i}(q,\omega)$ is the non-interacting response function of the $i-$th 2D subsystem, already introduced in Eq. (4.2) and in this case characterized by μ_i of the i-the subsystem. The total interacting response function is then

$$\chi_\tau(\mathbf{q},\omega;z,z') = \sum_{i,j}^{N} |\lambda_i(z)|^2 \chi_{\tau\, ij}(\mathbf{q},\omega)|\lambda_j(z')|^2, \tag{4.8}$$

with

$$\chi_{\tau\, ij}(\mathbf{q},\omega) = \chi^0_{\tau i}(\mathbf{q},\omega)\delta_{ij} + \chi^0_{\tau i}(\mathbf{q},\omega)W_{ij}(\mathbf{q},\omega)\chi^0_{\tau j}(\mathbf{q},\omega). \tag{4.9}$$

δ_{ij} is the Kronecker delta and the screened Coulomb interaction $W_{ij}(\mathbf{q})$ between $i-$th and $j-$th subsystems is defined as

$$W_{ij}(\mathbf{q},\omega) = \left[\left(\mathbf{1} - \mathbf{U}\boldsymbol{\chi}^{\mathbf{0}}_{\tau}\right)^{-1}\mathbf{U}\right]_{ij}. \tag{4.10}$$

Here $\boldsymbol{\chi}^{\mathbf{0}}_{\tau}$ is a diagonal matrix with the elements $\chi^0_{\tau i}\delta_{ij}$. The elements of the matrix $\mathbf{U}$ are given by

$$[\mathbf{U}]_{ij} \equiv U_{ij} = \int dz dz' |\lambda_i(z)|^2 \phi^c(\mathbf{q};z,z')|\lambda_j(z')|^2. \tag{4.11}$$

In this equation the function $\phi^c(\mathbf{q};z,z')$ is the Coulomb interaction between a source charge at vertical position z' and a test charge at z, obtained directly from the Poisson equation, which in q-space corresponds to

$$\frac{d}{dz}\left[\varepsilon(z)\frac{d\phi^c(\mathbf{q};z,z')}{dz}\right] - \varepsilon(z)q^2\phi^c(\mathbf{q};z,z') = -4\pi\delta(z-z').$$

Whithin a layer α corresponding to the surrounding medium or the region between two 2D electron layers, the relative dielectric constant $\varepsilon(z)$ is characterized by a constant permittivity ε_α. For each region, the Poisson equation equation admits a solution of the form

$$\phi^c_\alpha(\mathbf{q};z,z') = \frac{2\pi}{\varepsilon_\alpha q}e^{-q|z-z'|} + A_\alpha e^{qz} + B_\alpha e^{-qz}.$$

The coefficients A_α and B_α are found from the requirement that the general solution should be continuous, remain finite and its derivative has a jump of 4π at $z = z'$, which is consequence of Gauss's theorem.

We consider next the particular case of a thin layer as shown in Fig. 4.2. The bulk topological insulator and the material above and below the film are characterized by ε_2, ε_1 and ε_3 respectively ($\varepsilon_1 = \varepsilon_3 = 1$ for the systems studied in the following sections). In this case, the total thickness d of the topological insulator is defined as the distance

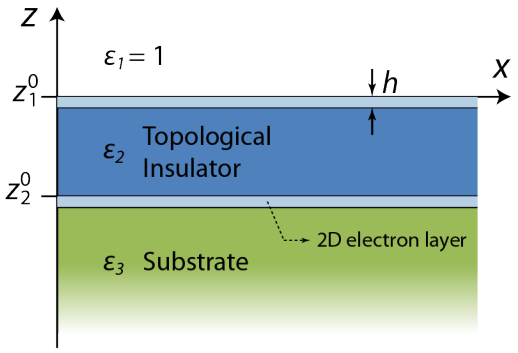

FIGURE 4.2: Schematic representation of a general topological insulator film geometry for the many-body calculations. The topological insulator with a bulk dielectric constant of ε_2 is sandwiched between vacuum and a substrate characterized by dielectric constants ε_1 and ε_3, respectively. The thin-layer regions below $z = z_1^0$ and $z = z_2^0$, having thickness h, represent the 2D electron layers. The thickness of the topological insulator in these calculations corresponds to $d = z_1^0 - z_2^0 = h$.

betweeen the top interface of the upper 2D electron layer and the bottom surface of the lower 2D electron layer, i.e., $d = z_1^0 - z_2^0 + h$ in Fig. 4.2. The Coulomb interactions in the three regions are given by

$$\begin{aligned}
\phi_1^c(\mathbf{q}; z, z') &= \frac{2\pi}{\varepsilon_1 q} e^{-q|z-z'|} + B_1 e^{-qz}, \\
\phi_2^c(\mathbf{q}; z, z') &= \frac{2\pi}{\varepsilon_2 q} e^{-q|z-z'|} + A_2 e^{qz} + B_2 e^{-qz}, \\
\phi_3^c(\mathbf{q}; z, z') &= \frac{2\pi}{\varepsilon_3 q} e^{-q|z-z'|} + A_3 e^{qz}.
\end{aligned} \tag{4.12}$$

In these equations, the coefficients $B_1 = \varepsilon_2(B_2 - A_2)/\varepsilon_1$ and $A_3 = \varepsilon_2(A_2 e^{-qd} - B_2 e^{qd})e^{qd}/\varepsilon_3$ are expressed in terms of A_2 and B_2, which, in turn, are given by

$$A_2 = \frac{\pi}{\varepsilon_2 q} \frac{(\varepsilon_2 - \varepsilon_1)\left[\varepsilon_2\left(e^{q(d-|z'|)} + e^{-q|d+z'|}\right) + \varepsilon_3\left(e^{q(d-|z'|)} - e^{-q|d+z'|}\right)\right]}{(\varepsilon_2^2 + \varepsilon_1\varepsilon_3)\sinh(qd) + \varepsilon_2(\varepsilon_1 + \varepsilon_3)\cosh(qd)},$$

$$B_2 = \frac{\pi}{\varepsilon_2 q} \frac{(\varepsilon_2 - \varepsilon_3)\left[(\varepsilon_2 + \varepsilon_1)e^{-q|d+z'|} + (\varepsilon_2 - \varepsilon_1)e^{-q(d+|z'|)}\right]}{(\varepsilon_2^2 + \varepsilon_1\varepsilon_3)\sinh(qd) + \varepsilon_2(\varepsilon_1 + \varepsilon_3)\cosh(qd)}.$$

The energies of the collective excitations at a given q are defined by poles of the total interacting response function (Eq. 4.8). As previously discussed, we always obtain σ from Eqs. (4.1)-(4.5), derived for single layers, and the Coulomb coupling is incorporated via the classical electromagnetic formalism.

4.1.3. Electrodynamic calculations

We calculate the dispersion relationship for semi-infinite surfaces from the maxima of the reflection coefficient of p-polarized waves incident on the system from the vacuum side. For the semi-infinite substrate, the reflection r_p is given by

$$r_p = \frac{\varepsilon_2 k_{1z} - \varepsilon_1 k_{2z} + (\sigma/(\varepsilon_0 \omega)) k_{1z} k_{2z}}{\varepsilon_2 k_{1z} + \varepsilon_1 k_{2z} + (\sigma/(\varepsilon_0 \omega)) k_{1z} k_{2z}}, \tag{4.13}$$

where ε_1=1 and ε_2 are the dielectric functions of vacuum and the substrate respectively, ω is the angular frequency of the incident plane-wave, σ is the in-plane conductivity [Eq. (4.1)] at the interface ε_0 is the vacuum permittivity and k_{1z} and k_{2z} are the z components of the wavevector of the incident and the transmitted plane-waves, respectively. In a similar way, the dispersion relationship of a thin-film in vacuum (medium 1) characterized by a dielectric function ε_2 and thickness d (medium 2), is obtained from the maxima of the corresponding reflection coefficient, r_p^{film} for an incident plane-wave given by

$$r_p^{film} = r_{12} + \frac{t_{12} r_{21} t_{21} e^{2ik_{2z}d}}{1 - r_{21} r_{21} e^{2ik_{2z}d}}, \tag{4.14}$$

where r_{ij} and t_{ij} are the reflection and transmission coefficients of the plane-waves entering from medium i to medium j respectively and k_{2z} is the z component of the wavevector of the plane-wave inside the film. The derivation of Eqs. (4.13) and (4.14) and the expressions for r_{ij} and t_{ij} are given in Appendix A. The above equations thus incorporate the effect of the 2D electron layers via the conductivity σ calculated according to the previous subsection. σ, and thus the reflection coefficients, are non-local, i.e. they depend on the horizontal component of the incident wavevector q. The local approximation corresponds to considering the value of $\sigma(q, \omega)$ for q=0.

The electric field $\mathbf{E}(\mathbf{r})$ at position $\mathbf{r} = (x, y, z)$ due to a point electric dipole p_z oriented along the z direction, located at $\mathbf{r_0}$=$(0, 0, z_{dip})$ and emitting at angular frequency ω can be evaluated using the plane-wave decomposition method. We use a dipole of strength p_z=$1e$·1nm. For example, when the dipole is situated above a plane interface (z=0), separating medium 1 and medium 2 , the x, y and z components $\mathbf{E}_{rx}$, $\mathbf{E}_{ry}$ and $\mathbf{E}_{rz}$ of the reflected field are given by

$$\begin{aligned}
\mathbf{E}_{rx}(\mathbf{r}) &= -\frac{i\omega^2\mu_0}{8\pi^2 k_1^2} p_z \int_{q=0}^{\infty} r_p(q) q^2 e^{ik_{1z}|z_{dip}+z|} \cos\phi \left[2\pi i J_1(\rho q)\right] dq, \\
\mathbf{E}_{ry}(\mathbf{r}) &= -\frac{i\omega^2\mu_0}{8\pi^2 k_1^2} p_z \int_{q=0}^{\infty} r_p(q) q^2 e^{ik_{1z}|z_{dip}+z|} sin\phi \left[2\pi i J_1(\rho q)\right] dq, \\
\mathbf{E}_{rz}(\mathbf{r}) &= \frac{i\omega^2\mu_0}{8\pi^2 k_1^2} p_z \int_{q=0}^{\infty} r_p(q) \frac{q^3}{k_{1z}} e^{ik_{1z}|z_{dip}+z|} \left[2\pi J_0(\rho q)\right] dq.
\end{aligned} \tag{4.15}$$

where we are integrating over all the parallel components of the wavevector q. $k_1 = 2\pi/\lambda$ is the wave number in vacuum. r_p is the reflection coefficient coefficient from Eq. (4.13), ϕ the polar angle of the position $\mathbf{r}$ with respect to the x axis and μ_0 is the vacuum magnetic permeability. $J_0(\rho q)$ and $J_1(\rho q)$ are the Bessel functions of first kind. The derivation of Eq. (4.15) and the expressions necessary to obtain the transmission in the semi-infinite interface as well as the fields in the thin-film are given in Appendix B. In the following, we distinguish between the total, $\mathrm{E}^{\mathrm{tot}}$, and the induced, $\mathrm{E}^{\mathrm{ind}}$, fields by including and excluding, respectively, the fields from the illumination source itself.

To study the localized Dirac plasmons in the finite disks, under dipolar or plane-wave illumination, we use the Boundary Element Method (BEM) as Maxwell's equations solver [64]. In these calculations, the 2D electron layers at the top and at the bottom surfaces of the disk, schematically shown in Fig. 4.1(c), are modelled as thin finite thickness layers. We obtain the dielectric function $\varepsilon_{2\mathrm{D}}(\omega)$ of this layer from the non-local conductivity using [33]

$$\varepsilon_{2\mathrm{D}}(q,\omega) = 1 + \frac{i\sigma(q,\omega)}{\varepsilon_0 \omega t}, \tag{4.16}$$

where t is the thickness of the 2D system. The in-plane conductivity of the thin layer described by Eq. 4.16 and of the idealized 2D layers is thus identical. We take as a standard reference, a value of $t = 1$ nm, with a circular rounding of the edges to avoid sharp edges. The thickness d of the disks (Fig. 4.1) refers to the bulk part, without including the 2D electron layers. Notice that the many-body calculations of the films of same thickness use the same value of d but in this case including the (quasi) 2D layers (Section 4.1.2 and Fig. 4.2). We describe the implication of the chosen 2D electron layer thickness t and other convergence issues in Subsection 4.3.1.

In principle, $\varepsilon_{2\mathrm{D}}$ depends on the parallel wavevector q, but our BEM calculations cannot introduce the non-locality directly. Nonetheless, for the calculations of disks we study

situations where either optical or acoustic modes are efficiently excited, but not simultaneously, so that we can focus on the wavevector $q_{\rm SP}$ of the modes being excited. For the excitation of the optical mode, the $q_{\rm SP}$ corresponds to values $q_{\rm SP}^{optical}$ obtained from the optical branch of the dispersion relationship. We thus use $\varepsilon_{\rm 2D}^{optical}(\omega) = \varepsilon_{\rm 2D}(\omega, q_{\rm SP}^{optical})$. Similarly, in the case of the acoustic mode, we take $\varepsilon_{\rm 2D}^{acoustic}(\omega) = \varepsilon_{\rm 2D}(\omega, q_{\rm SP}^{acoustic})$, with $q_{\rm SP}^{acoustic}$ from the acoustic branch.

4.2. Excitation of propagating Dirac plasmons in infinite surfaces

4.2.1. Dirac surface plasmons in a semi-infinite substrate

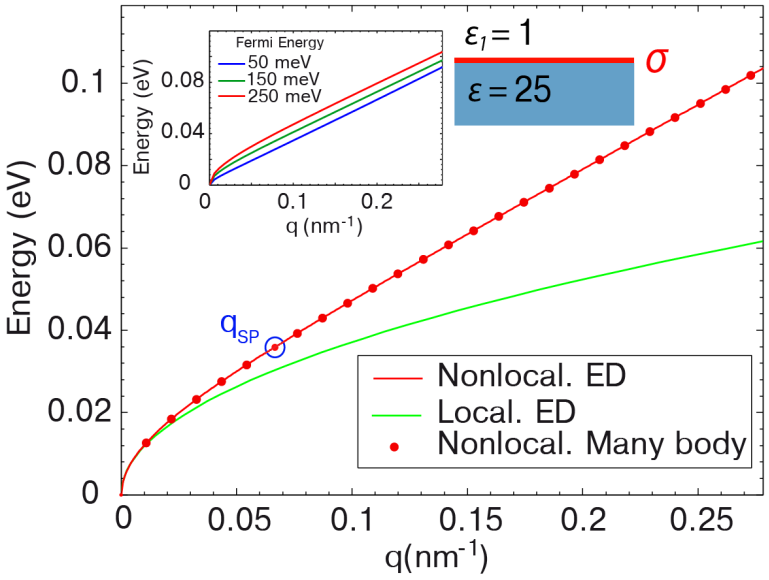

FIGURE 4.3: Dispersion relationship of the propagating plasmons supported by a semi-infinite substrate of the topological material Bi_2Se_3. We show the results from the electrodynamic calculations using local (green line) and non-local (red line) conductivities together with the non-local dispersion obtained directly from the many-body calculations (red dots). The inset shows the tunability of the dispersion as a function of Fermi energy. The bulk dielectric function considered is ε_{bulk}=25.

We first study the optical response of a semi-infinite topological insulator Bi_2Se_3 substrate, schematically shown in Fig. 4.1(a). Figure 4.3 shows the dispersion obtained from the maximum of the calculated reflection [Eq. (4.13)], both for the non-local [$\sigma(q,\omega)$, red line] and for the local [$\sigma(q=0,\omega)$, green line] description. Figure 4.3 also shows the non-local dispersion (red dots) directly obtained from the many-body calculations

[poles of Eq. (4.8)]. Both sets of non-local results shows very good agreement, which indicates the consistency of our approach.

The dispersion relationship reveals the presence of surface plasmons in the THz region of the spectrum, which are characterized by a much larger plasmonic wave number q_{SP} (lower wavelength) than the incident plane-wave. For example, a surface plasmon excited at λ=33 μm ($\approx$ 0.0375 eV) marked by the blue circle in Fig. 4.3 has a (non-local) plasmonic wavelength $\lambda_{SP} = 2\pi/q_{SP} = 90$ nm, showing a squeezing of the wavelength to $\lambda/370$. The field is evanescent and extremely confined in the vertical z direction as can be seen from the corresponding perpendicular wave number in vacuum given by $k_z = ((2\pi/\lambda)^2 - q_{SP}^2)^{1/2} \approx iq_{SP}$. The local (green line) and non-local (red line) dispersions behave similarly for low energies. In contrast, for sufficiently high values of incident energy (above 0.03 eV), the local and non-local dispersion curves significantly differ from each other. The local approximation results in a larger wavevector q_{SP} for the excited plasmon, underlying the importance of using a non-local approach to accurately obtain the optical response of topological insulators in this energy range. The strong dependence of the plasmon dispersion on the Fermi energy is shown in the inset for the non-local case, in the range $E_F = 50$ meV - 250 meV. The dependence of the properties of the plasmonic resonance on the Fermi energy, which can be experimentally controlled by a simple voltage bias, constitutes a major advantage of 2D plasmons [34, 204, 205].

Due to the very large wave number q_{SP}, it is not possible to excite surface plasmons in a perfectly flat, infinite surface using a plane-wave, even for a standard Kretschmann configuration. We use a localized source giving a broad distribution in q-space, consisting of an electric dipole at 5 nm above the Bi_2Se_3 substrate. Fig. 4.4(a) shows the real part of the vertical component of the electric field E_z^{ind} (Vm^{-1}) induced by a dipole of strength $1e{\cdot}1$nm and radiating at $\lambda = 33$ μm (blue circle in Fig. 4.3) and oriented along the z direction. The fields are calculated in the $x - z$ plane. The field is identical for any plane containing the axis z, due to the rotational symmetry of both the substrate and the dipole illumination.

The obtained field distribution is characteristic of a propagating surface plasmon. The tight confinement along the z direction and the extreme sub-wavelength nature of the plasmon, $\lambda_{SP} \approx 90$ nm, can be observed in the figure. It can be also appreciated from Fig. 4.4(a) that the plasmon decays slowly along the x axis. Because of the low losses in the topological insulator [199–202], the plasmon damping is mainly caused by the $1/\sqrt{x}$ decay of the electric field required by energy conservation.

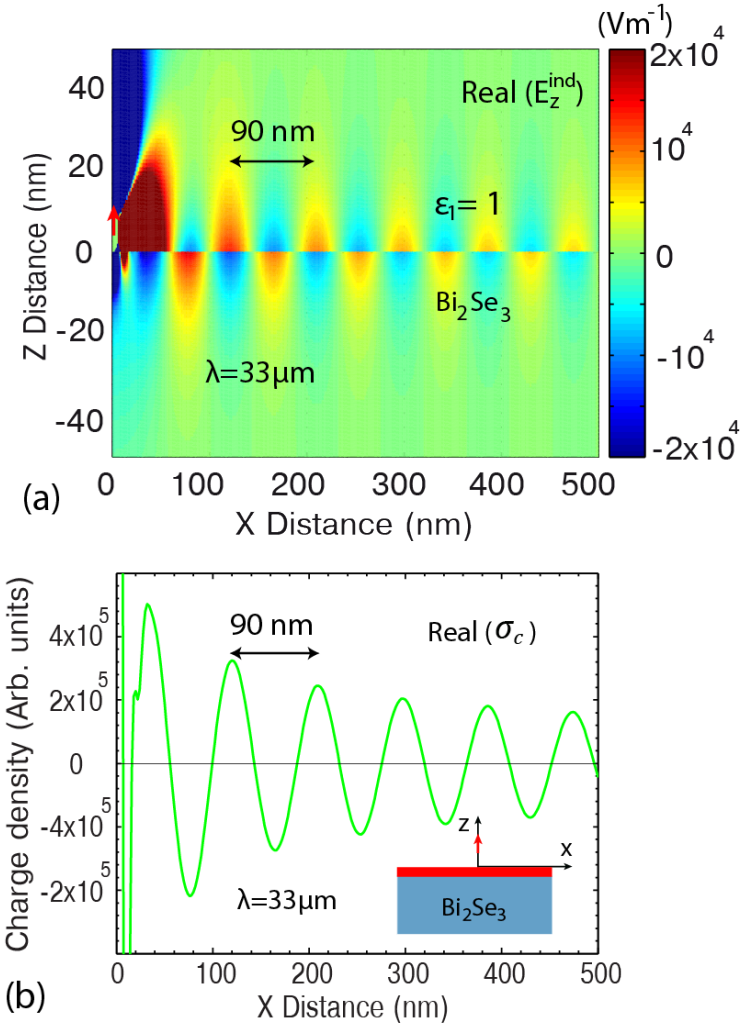

FIGURE 4.4: (a) Map of the real part of the z component of the induced electric field E_z^{ind}, in SI units, calculated in the $x-z$ plane, induced by a dipole oriented perpendicular to the surface along the z direction and placed 5 nm above a semi-infinite substrate of Bi_2Se_3 topological insulator (marked as a red arrow). A dipole of strength $1e{\cdot}1$nm and radiating at $\lambda = 33$ μm is chosen. (b) Real part of the corresponding surface charge density σ_c calculated along the x axis, in arbitrary units.

The surface charge density σ_c can be obtained from the normal components of the electric displacements $\varepsilon_0\varepsilon_1\mathbf{E}_{1z}^{tot}$ and $\varepsilon_0\varepsilon_2\mathbf{E}_{2z}^{tot}$ in medium 1 and medium 2 respectively, as

$$\sigma_c = \varepsilon_0\varepsilon_1\mathbf{E}_{1z}^{tot} - \varepsilon_0\varepsilon_2\mathbf{E}_{2z}^{tot}. \tag{4.17}$$

Figure 4.4(b) shows the real part of the surface charge density calculated along the x axis, $(y = 0, z = 0)$. The oscillation of the charge density follows the profile of the normal component of the electric field at the interface [Fig. 4.4(a)].

4.2.2. Dirac surface plasmons in a thin-film

We now discuss the optical response of a thin-film topological insulator. The plasmon dispersion for a 5 nm thin Bi_2Se_3 film is shown in Fig. 4.5. Two identical 2D electron layers supported at the two interfaces with the surrounding vacuum interact with each other to support two hybridized plasmon modes [194], as manifested by the two branches of the non-local dispersion (blue lines). The low energy and high energy branches of the dispersion, the acoustic and optical modes respectively, fall at each side of the dispersion of the semi-infinite substrate, which is reproduced in this figure (red line, non-local) for straightforward reference. For a given energy, the acoustic plasmon thus has a particularly large wavevector $q_{\rm SP}$ (smaller $\lambda_{\rm SP}$) and therefore it is more tightly confined to the film ($k_z = ((2\pi/\lambda)^2 - q_{\rm SP}^2)^{1/2} \approx iq_{\rm SP}$).

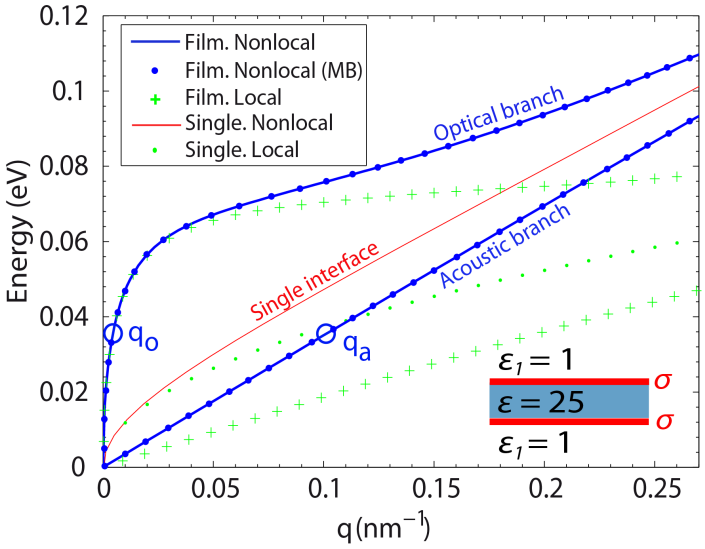

FIGURE 4.5: Optical and acoustic branches of the dispersion relations of surface plasmons in a Bi_2Se_3 topological insulator thin-film. The results from the electrodynamic calculations using non-local (blue curves) and local (green +) conductivities are shown for a film of thickness 5 nm. The non-local results are also compared with the many-body calculations (blue dots, MB). The non-local (red line) and local (green dots) plasmon dispersion from electrodynamical calculations for a semi-infinite substrate of the same material (as in Fig. 4.3) is also shown. q_o and $q_{\rm a}$ mark the points of evaluation of the near-field in Fig. 4.6 and charge density in Fig. 4.7. The bulk dielectric function considered is ε_{bulk}=25.

As for the semi-infinite substrate, the dispersion relationship of the thin-film behaves qualitatively similarly when using a non-local (blue line) and local (green+) treatment. Nonetheless, non-locality can play a quantitatively important role in the response of the acoustic mode supported by the thin film, for which $q_{\rm SP}$ is particularly large. While both

the local and non-local calculations predict an acoustic mode with very large q_{SP}, the exact value is significantly lower for the more precise non-local approach, bringing this mode closer to the dispersion of the semi-infinite substrate. In the case of the optical branch, the discrepancy between the local and non-local results becomes important only for energies larger than $\approx$ 0.06 eV, when the local calculation remains relatively flat as a function of q, with a much weaker slope than the non-local result. It can be observed that the non-local dispersion found within the electrodynamical treatment reproduce the many-body calculation of the thin-film (Fig. 4.5 blue dots), obtained according to Section 4.1.2, with very good accuracy.

We excite next the optical and acoustic plasmon modes supported by the 5 nm thin Bi_2Se_3 film, using a similar dipolar source of strength $1e{\cdot}1$nm located 3 nm away from the film, oriented along the perpendicular z direction and emitting at λ=33 μm. The nature of the plasmonic waves excited by the dipole can be understood by examining the electric field induced near the film. Figures 4.6(a) and (b) show the real part and phase of the z component of the induced electric field E_z in the $x-z$ plane in the vicinity of the film. In Fig. 4.6(a), the real part of the field close to the film shows a fast oscillation of periodicity 60 nm, corresponding to the plasmonic wavelength of the acoustic mode λ^{a}_{SP} $= 2\pi/q_a$ obtained from the dispersion (Fig. 4.5). In this region, the induced field at both sides of the film are generally oscillating in phase, as expected for the excitation of an acoustic mode [194]. Analysing it in more detail, however, the phase of the fields at both sides of the interface [Fig. 4.6(b)] is not always exactly equal. We attribute this effect to the simultaneous excitation of the two plasmonic resonances. The acoustic mode would dominate the signal near the film, but decays very fast as we move far away from the surface due to its strong confinement (large value of $k_z \approx iq_{SP}$). In contrast, the optical mode contributes comparitively weakly near the surface, but it becomes dominant at sufficiently far distances due to its smaller k_z (larger λ_{SP}) compared to the acoustic mode. To explore this behavior in more detail, we calculate E_z at 3 nm and 40 nm away from the film at both sides (marked by the two dark and two red dashed lines in Fig. 4.6(a), respectively). Since the acoustic mode decays faster, the field difference between the smaller and larger distances (for both sides) should be dominated by this mode. The result is shown in Fig. 4.6(c). As expected, we obtain oscillations almost perfectly in phase when comparing the subtracted signal above the film with that below, both with the periodicity ($\approx$60 nm) of the acoustic modes.

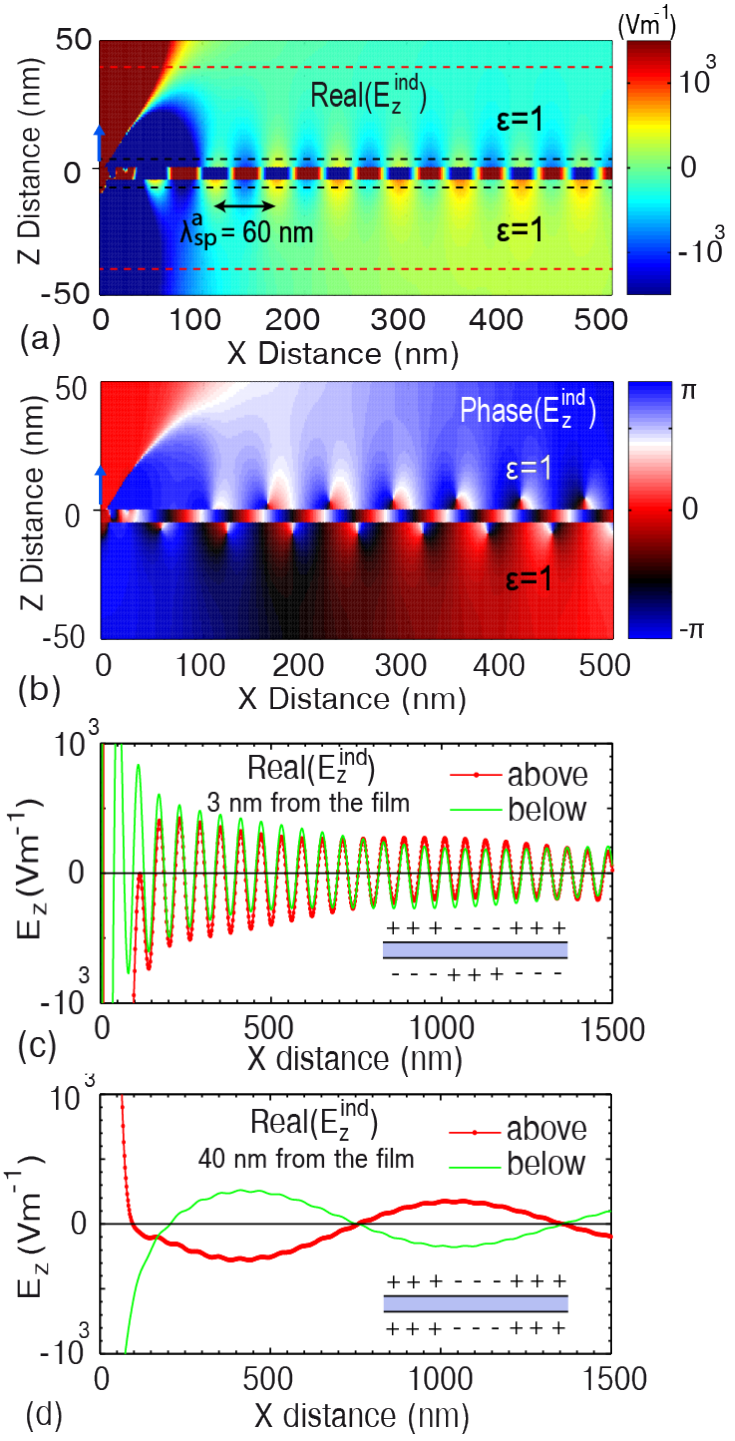

FIGURE 4.6: Maps of the real part (a) and phase (b) of the z component of the electric field E_z^{ind} induced by a dipole emitting at 33 μm, situated 3 nm above the film and oriented along the z direction (marked with blue arrows). (c) Difference between the real part of the field at 3 nm [dark dashes in (a)] and 40 nm [red dashes in (a)] away from the film. The difference is calculated both for the fields above (red line) and below (green line) the thin-film. (d) Real part of the field calculated above (red line) and below (green line) the film at 40 nm distance from the top and bottom surfaces, along the red dashed lines in (a). A dipole of strengh $1e$·1nm is chosen and the field plots are in SI units.

As we move away from the film, the relative weight of the optical modes increase and the z component of the fields in Fig. 4.6(a) at each side of the film shows opposite orientations. We plot in Fig. 4.6(d) the real part of E_z at a distance of 40 nm above and below the film [red dashed lines in Fig. 4.6(a)]. The fields have an opposite sign at each side of the film with a periodicity of the oscillations of $\approx$ 1230 nm that corresponds to the wavelength of the optical mode from the dispersion in Fig. 4.5. The symmetry and periodicity of the fields in Fig. 4.6 are thus consistent with the excitation of both an acoustic and an optical mode, the former predominating in the vicinity of the film and the latter at larger distances.

The field symmetries can be expressed in terms of charge symmetries using Eq. 4.17. As expected and studied in more detail in Fig. 4.7, optical modes show charges of equal sign at both interfaces, which explains its comparatively larger energy in the dispersion relation due to the Coulomb repulsion between equal charges, piled up at the top and bottom interfaces of the film [inset of Fig. 4.6(d)]. In contrast, the acoustic modes at lower energy show charges of opposite sign at the interfaces [inset of Fig. 4.6(c)].

Since the fields near and away from the topological insulator film are dominated by the contributions from the acoustic and optical modes, respectively, the acoustic mode is expected to be effectively excited by a dipolar source (Fig. 4.6) situated near the film, whereas the optical mode will be predominantly excited when the dipole is far away from the film. To further explore the degree of selective excitation possible and its consequences for spin and charge control, we calculate the charge density σ_c in a film for two dipole-film distances. Figure 4.7 shows the real part of the surface charge densities at the top and bottom interfaces induced by a dipolar source radiating at λ=33 μm situated at (a) 3 nm and (b) 100 nm away from the top of the film.

When the dipole is at a distance of 3 nm from the film [Fig. 4.7(a)] the induced charges at the top and bottom surfaces oscillate in anti-phase with a spatial periodicity of $\approx$ 60 nm, consistent with the field distribution in Fig. 4.6(c). Nonetheless, we note that some care is necessary when attempting to visually deduce the charges from field plots, because the charge depends on the displacement outside and inside the film. For example, we found (not shown) that for a dipole 30 nm above the thin-film, the field calculated at the surface is dominated by the optical mode, but the charge distribution show a more predominant signature from the acoustic mode. When the dipole is located 100 nm away from the surface, [Fig. 4.7(b)], the charge densities show the same sign at both interfaces and oscillate with a larger spatial periodicity of $\approx$ 1230 nm. Thus, the charges are dominated by the acoustic mode for 3 nm distance, and by the optical mode at

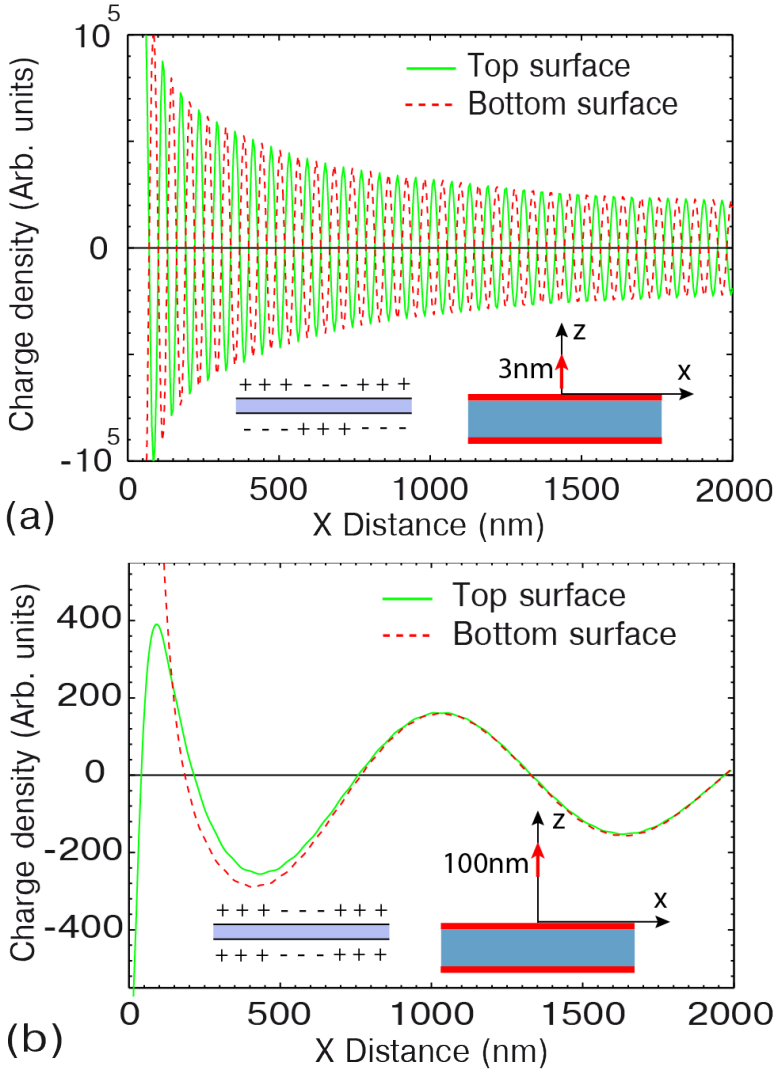

FIGURE 4.7: Real part of the surface charge density calculated at the top and bottom interfaces of a topological insulator thin-film of 5 nm thickness. A dipolar source radiating at wavelength $\lambda = 33\,\mu$m and oriented along the z direction is used to excite the surface plasmons in the film as in Fig. 4.6. A dipole of strength $1e{\cdot}1$nm is chosen and the charge density is plotted in arbitrary units. The charge densities plotted for the dipole placed (a) 3 nm and (b) 100 nm above the film show periodicities close to $\lambda_{SP} \approx 60$ nm and $\lambda_{SP} \approx 1230$ nm, respectively. The insets in (a) and (b) schematically show the corresponding charge distributions at each surface of the film. The fields are calculated for $y = 0$, but they are identical for any radial direction.

100 nm. The dependence of the relative strength of the excited acoustic and optical modes on the dipole distance allows to tune the relative strength of both modes by varying the dipole-film distance. An interesting consequence of this selective excitation of acoustic and optical modes is the possibility to control spin and charge properties, an effect further discussed in the next section.

4.2.3. Charge density and spin-plasmons in a Bi_2Se_3 thin-film

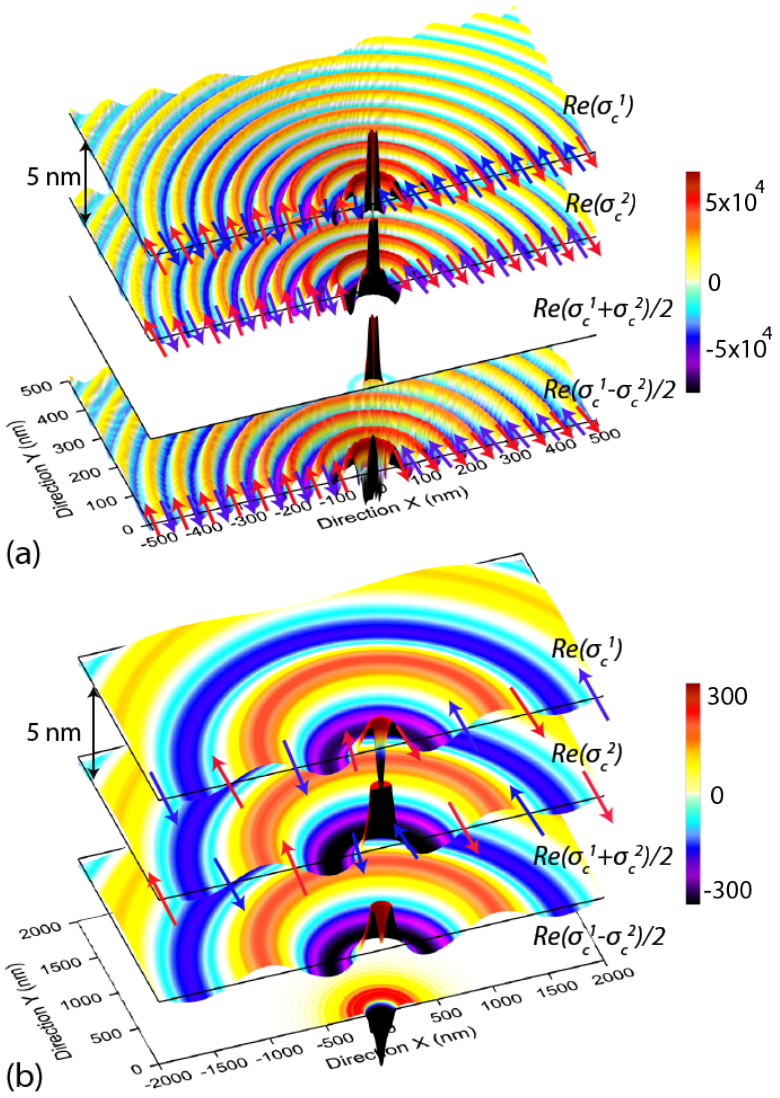

FIGURE 4.8: Real part of the induced charge densities σ_c^1 and σ_c^2, in arbitrary units, calculated in a 5 nm thin-film Bi_2Se_3 topological insulator when a dipole of strength $1e{\cdot}1\text{nm}$ emitting at $\lambda = 33\ \mu$m and oriented along the z direction is placed at a distance 3 nm (a) and 100 nm (b) above the film. In both figures, from the top, the first two panels show the charge densities at the top and the bottom surfaces of the film respectively, and the third and forth panels show the total effective charge density oscillation given by $(\sigma_c^1+\sigma_c^2)/2$ and the total effective spin oscillation given by $(\sigma_c^1-\sigma_c^2)/2$ in the film as a whole. The blue and red arrows indicate the directions of the spins. Plots (a) and (b) corresponds to the same systems showed in Fig. 4.7 (a) and (b), respectively, at a particular instant.

An interesting aspect of collective excitations in topological insulators is the possibility that they offer to control both charge and spin at the nanoscale. Figure 4.8 emphasizes

the different spin and charge behaviour of the acoustic and optical modes, for the same configuration as in Fig. 4.7. From the top, the first two panels in Fig. 4.8(a) show the real part of the induced charge density oscillations at the top (σ_c^1) and bottom (σ_c^2) interfaces of the 5 nm thin-film, when the dipole is situated at 3 nm away from the film. The anti-phase nature of the charge density oscillations at both interfaces results in a near zero total effective charge density oscillation in the film as a whole, as revealed by the sum $\mathrm{Re}(\sigma_c^1 + \sigma_c^2)/2$ shown in the third panel from the top of Fig. 4.8(a). The sum is only comparable to either σ_c^1 or σ_c^2 near the axis, where many evanescent components of the dipole contribute to the response, in addition to those associated with the plasmonic mode.

Another important consequence of the charge density oscillations is expressed in the total spin distribution in the film. At each interface, the direction of the spin is orthogonal to the surface wave propagation direction and the sign of the charge density oscillation depends on the component of the associated field along the normal to the surface. Because of the opposite helicity of the Dirac states at both sides of the film, the spin is thus proportional to $(\sigma_c^1 - \sigma_c^2)/2$, shown in the bottom panel of the figure. The anti-phase nature of the corresponding charge density oscillations in Fig. 4.8(a) results in an in-phase collective oscillation of the spin (effective spin wave), so that the total average spin at the film as a whole corresponds to the value of a single interface. The 60 nm periodicity of this spin oscillation is the same as that of the charge, as in both cases it is given by the periodicity of the acoustic mode.

We examine next in Fig. 4.8(b) the results for the 100 nm distance of the dipole from the film, for which the optical mode dominates the obtained charge. The charge densities at both surfaces of the film oscillate in phase (top two panels), which result in a large total effective charge density oscillation with a 1230 nm periodicity characteristic of the optical mode, as shown in the third panel (from the top) of 4.8(b). This in-phase oscillation of the charge densities induce spin waves of opposite phase at each surface, and thus results in an effective near-zero total spin wave, as shown in the bottom panel. Therefore, by varying the distance between the dipolar source and the film, we can selectively excite either a charge wave or a spin wave in the topological insulator thin-film. Intermediate distances would results in an admixture of both types of waves.

4.3. Localized surface plasmons in Bi_2Se_3 nanodisks

Up to now, we have considered the excitation of propagating plasmons in infinite surfaces. Similar to other finite structures, topological insulator disks of finite size also support localized Dirac plasmons. We consider Bi_2Se_3 disks of thickness $d = 5$nm and two different diameters, $D = 50$ nm and $D = 600$ nm. The disks are oriented normal to the z axis and their center is at x=0, y=0, z=0. Surface plasmons in finite-sized disks can be understood as stationary charge density waves produced by the interference of propagating thin-film plasmons imposed by boundaries of the disk. Propagating plasmons are reflected at the edges of the disk and give rise to localized Fabry-Pérot-like cavity modes in a constructive interference. These resonances occur at frequencies that depend on the geometry of the disk. [206–208].

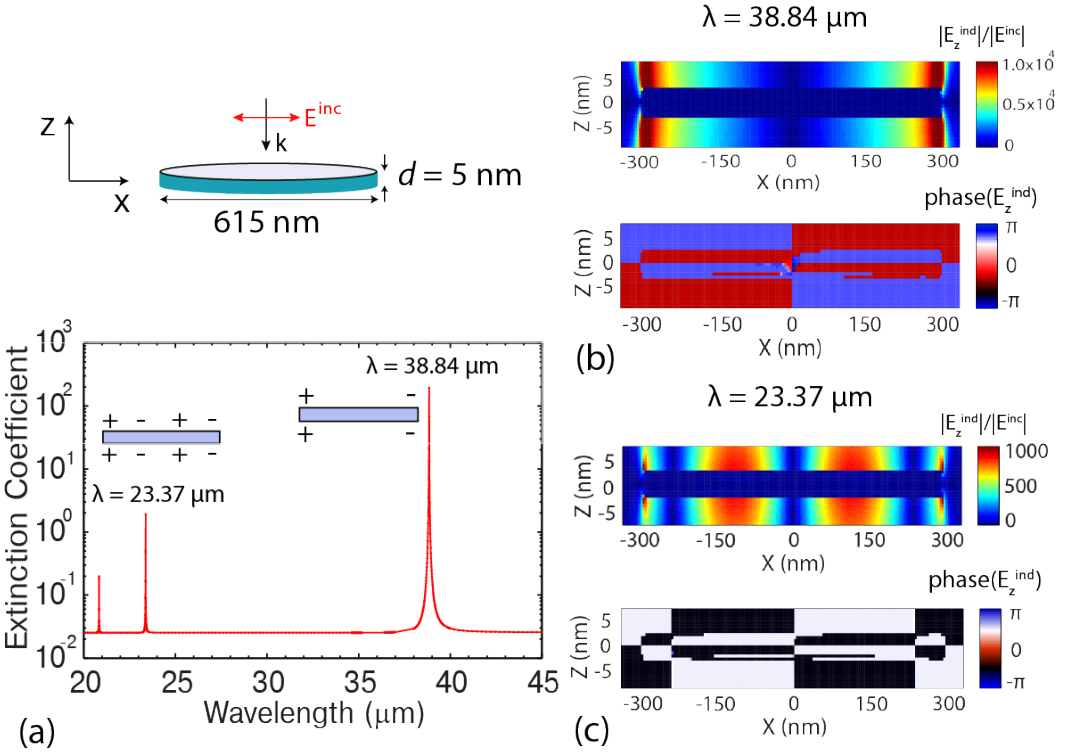

FIGURE 4.9: Optical response of a Bi_2Se_3 thin disk of diameter 600 nm and thickness 5 nm that supports localized optical plasmons, illuminated with a plane wave polarized along the x direction and incident from the top (z axis), as shown in the schematics. The coordinate axis indicates the different directions. The center of the disk is situated at x=0, y=0, z=0. (a) Extinction coefficient of the disk. (b) Map of the absolute value of the z component of the induced electric field normalized to the corresponding value of the incoming wave $|E_z^{ind}|/|E^{inc}|$ (top) and phase (bottom) at the first prominent spectral peak at $\lambda = 38.84$ μm. The fields are obtained in the vertical plane, y=0, passing through the center of the disk and parallel to the incident electric field. (c) as in (b), but for the second lowest-energy peak in the spectrum at $\lambda = 23.37$ μm.

We calculate first the far-field response of the large disk of diameter 600 nm and thickness 5 nm. Figure 4.9(a) shows the extinction coefficient of the disk (extinction cross section normalized by the top surface area of the disk) when illuminated by a plane-wave incident from the top with linear polarization along x, as schematically shown at the top of Fig. 4.9(a). For the small thickness of the disks, the electric field oriented along x of the incident plane-wave can be considered constant (negligible phase retardation), so that only optical modes that show symmetric charge distribution with respect to the z=0 plane are excited (see below). Thus, according to the discussion in Section 4.1.3, we account for the non-locality of the dielectric function by using $\varepsilon^{optical}(\omega) = \varepsilon^{optical}(\omega, q)$ in our BEM calculations. The extinction spectrum shows sharp peaks associated to the localized plasmon resonances at the disk. These peaks are extremely narrow because of low absorption and small radiative losses in the disk. In experiments, the resonances could be broader because of, for example, experimental imperfections or edge effects [209, 210].

In order to better understand the nature of the resonances, we calculate the electric field distribution around the disk at the position of two of the peaks. Figure 4.9(b) shows the amplitude (top) and phase (bottom) of the electric field E_z induced at the disk for the lowest energy peaks in the spectra, at $\lambda = 38.84$ μm. Figure 4.9(c) presents the equivalent results for the peak at $\lambda = 23.37$ μm. The fields are calculated in the vertical plane, y=0, passing through the center of the disk and parallel to the incident electric field. As expected, comparing the fields at the top and bottom surfaces of the disks, we observe an antisymmetric E_z distribution with respect to the central $z = 0$ horizontal plane, or equivalently, the symmetric charge distribution [see insets in Fig. 4.9(a)] characteristic of the optical mode. The amplitude and phase for $\lambda = 38.84$ μm show an antisymmetric field distribution in the horizontal direction (with respect to the $x = 0$ plane) corresponding to a dipolar excitation [see Fig. 4.9(b)]. The peak at $\lambda = 23.37$ μm is the second lowest-energy antisymmetric mode, again with respect to the x=0 plane, presenting 3 nodes along the x axis. Other modes supported by the structure [211], such as those symmetric with respect to x=0, are not excited by the considered incident plane-wave. Last, we notice that the diameter of the disk is of the order of the plasmonic wavelength ($\lambda_{SP}^{optical}/2 \approx 848$ nm at the lowest energy peak) as expected for cavities modes [212].

We consider next a smaller disk of diameter 50 nm and thickness 5 nm. The diameter is comparable to the plasmonic wavelength of the acoustic mode (in the range of energies explored here), and much smaller than the wavelength of the optical mode (except

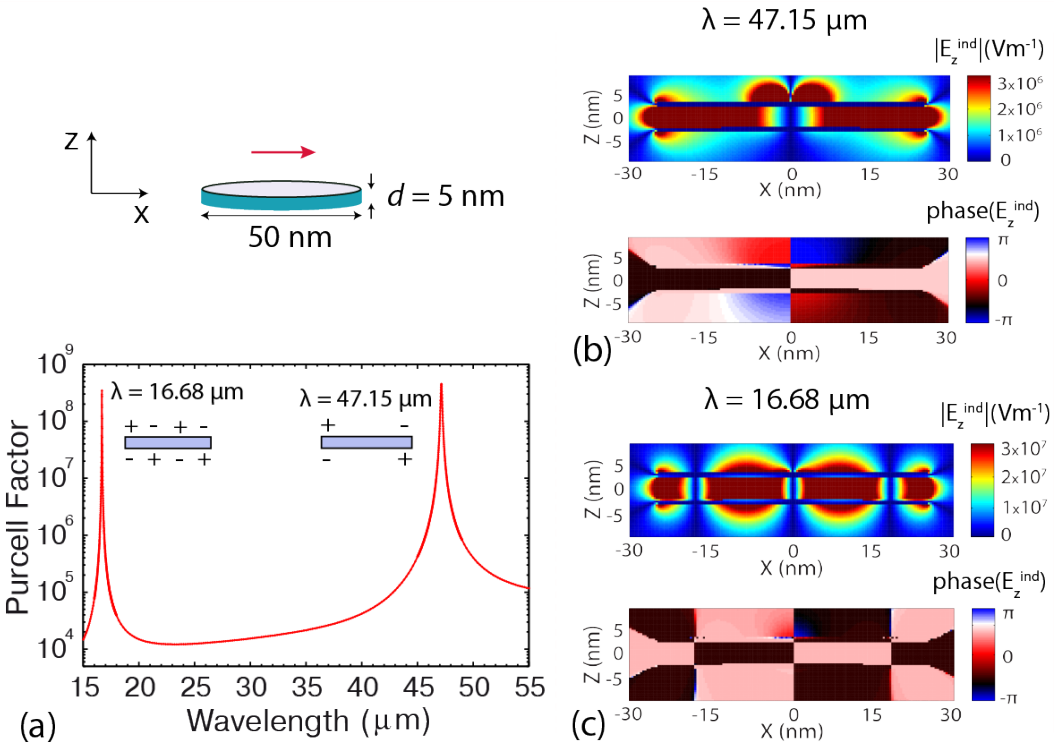

FIGURE 4.10: Optical response of a Bi_2Se_3 thin disk of diameter 50 nm and thickness 5 nm supporting localized acoustic plasmons. (a) Purcell factor calculated for an electric dipole of strengh $1e{\cdot}1$nm situated at a distance $z = 3$ nm above the center of the top surface of the disk and oriented along the x direction, as shown in the schematic. The coordinate axis indicate the different directions and the center of the disk is situated at x=0, y=0, z=0. (b) Maps of the amplitude (top) and phase (bottom) of the z component of the induced electric field at the peak of $\lambda = 47.15$ μm. The field is obtained in a vertical plane, y=0. (c) As in (b), but for the second lowest-energy peak in the spectrum at $\lambda = 16.68$ μm.

at large enough energies). We thus expect the response to be mainly dominated by acoustic resonances, and use $\varepsilon_{2D}^{acoustic}$ to describe the 2D electron layer. As we will see, the field symmetries of the resonances obtained in this situations correspond indeed to that of acoustic modes. We note that a more rigorous non-local approach may reveal the existence of some optical modes in the $\sim$ 15-20 μm wavelength range, but they are not revealed in our approach.

The localized acoustic mode couples very weakly with plane-waves because of the anti-symmetric charge distribution characterizing the thin-film acoustic mode [Fig. 4.6(c) and Fig. 4.7(a)], i.e., opposite signs for opposing interfaces. Therefore in Fig. 4.10 we consider a dipolar source in vacuum and show the Purcell factor, PF, obtained as

$$\mathrm{PF} = 1 + \frac{6\pi c}{\omega^3 \mu_0 p}\mathrm{Imag[E]}, \tag{4.18}$$

where c is the speed of light in vacuum, ω is the angular frequency, $\mu_0 = 4\pi \times 10^{-7}$ Hm^{-1}, p is the dipole moment and E is the induced electric field at the position of the dipole along its polarization direction. The Purcell factor is defined here as the enhancement in the emission rate of the dipole due to its coupling to the localized mode of the disk, compared to the emission in vacuum. The spectrum [Fig. 4.10(a)] is shown for horizontal orientation (parallel to the x axis) of a dipole of strengh $1e{\cdot}1$nm located 3 nm above the center of the top surface of the disk, as shown in the top schematic. Two peaks are observed in the spectra due to the excitation of two plasmonic modes in the disk.

The excited modes can again be further analyzed by plotting the field distribution around the disk at the positions of the spectral peaks. Figure 4.10(b) shows the amplitude (top) and phase (bottom) of the z component of the electric field induced E_z^{ind} (Vm^{-1}) at the $y = 0$ vertical plane passing through the center of the disk and containing the dipole, for the lowest energy spectral peak at $\lambda = 47.15$ μm. Figure 4.10(c) shows the equivalent result for the next lowest energy mode ($\lambda = 16.68$ μm). The amplitude and phase for both modes shows that the excited mode has a similar antisymmetric field distribution in the horizontal direction (with respect to the x=0 plane) as found for the large disks in Fig. 4.9. The main difference with the large disk is that the fields for the small disks are anti-symmetric with respect to the central z=0 horizontal plane, which confirms the excitation of acoustic modes. The peak for the small disk at $\lambda = 47.15$ μm corresponds to the excitation of dipolar-like charge distributions with opposite dipole moment at each interface, leading to the excitation of a quadrupolar mode. The resonance at $\lambda = 16.68$ μm is a higher order mode. The corresponding charge distribution is sketched in the insets of Fig. 4.10(a). Another set of localized acoustic modes showing spherical symmetry in the horizontal $x-y$ plane could be excited if the dipole over the disk center is oriented along the vertical z direction [206].

4.3.1. Convergence

Here we discuss our work to assess the convergence of the disk BEM results shown in this chapter. In the previous calculations, the 2D electron layers are treated as 1 nm thick regions characterized by a thickness-dependant dielectric function (as discussed in Subsection 4.1.3). In the BEM, usually, more boundary points give better converged results. Here, the convergence studies are performed with respect to the number of

boundary points and the thickness of the 2D electron layer. Furthermore, we also compare the BEM results with COMSOL [213] calculations that treat the 2D electron layers as infinitely thin layers of adequate conductivity, in a similar manner as in Section 4.2. The COMSOL calculations thus consider the boundary conditions in the presence of a 2D conductivity (Appendix A) and were performed by our collaborator Alexey Nikitin at Nanogune in Donostia-San Sebastián. We consider the same scenarios for the disks as in the previous discussion.

We first examine how the calculations using the BEM for different number of boundary points compare with the results obtained using COMSOL. We use here the same t =1 nm thickness of the 2D electron layer as in Figs. 4.9 and 4.10. Figure 4.11(a) shows the extinction coefficient of the disk of diameter 600 nm and thickness $d = 5$ nm under plane-wave illumination, for 1098 (red line), 1650 (green line) and 1903 (blue line) boundary points. As the number of boundary points is increased from 1098, the spectral positions of the peaks are redshifted, but the results for 1650 and 1903 boundary points are very similar. The position of the peaks also agrees reasonably well with the results obtained using COMSOL (black line), though the BEM spectra obtained with the larger number of boundary points is slightly redshifted with respect to the COMSOL calculation.

Compared to the BEM results, COMSOL calculations provide a weak background between peaks and a reduced strength of the low-energy spectral peaks. The difference may be due to the intrinsic challenges to obtain converged results for structures with very large aspect ratios. The COMSOL calculations also show worse spectral resolution at large energies, i.e., short wavelengths, which influences the maximum peak strength of such narrow peaks. Last, we notice that the background signal is very weak, so that the larger BEM values could also be partially explained by a relatively small numerical error, or by small edge effects due to the thickness of the 2D electron layer used in the BEM calculations. For this chapter, we are mostly interested on the nature and the spectral position of the localized resonances in the disk. The agreement between the spectral position of the peaks in BEM and COMSOL is overall rather good. For the modes in Fig. 4.9, we also obtained a similar spatial field pattern with COMSOL (not shown) as with BEM, indicating that the physics is correctly reproduced.

The results in Fig. 4.11(b), shows the Purcell Factor of a dipole near the 5 nm thick disk of 50 nm diameter, under the same conditions as in Fig 4.10(a). We observe a very good convergence as the boundary points are increased from 724 (red line) to 1096 (green line) and 1463 (blue line). Furthermore, the agreement with the COMSOL results

(black line) is, in this case, excellent. The main difference is the weaker COMSOL peak at $\lambda \approx 16.6$ μm, most likely due to the use of less wavelength points in the spectra.

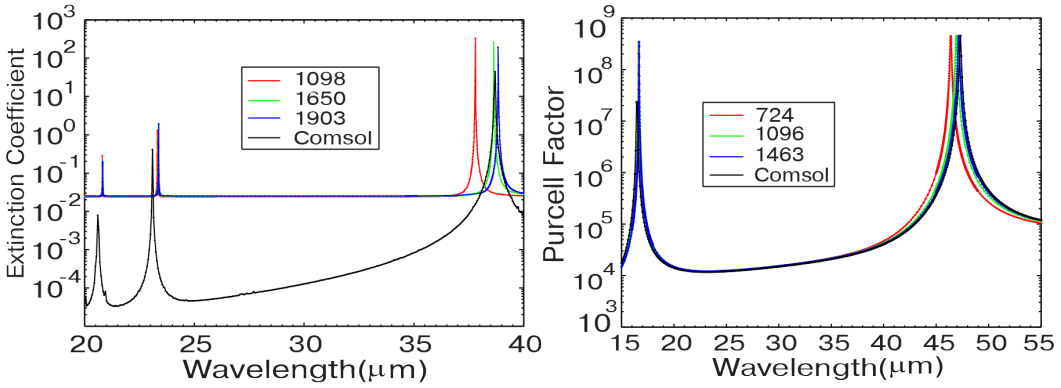

FIGURE 4.11: Numerical convergence of the optical response of topological insulator disks calculated using the BEM for a 2D electron layer thickness of $t = 1$ nm, compared with the results obtained using COMSOL. (a) Extinction coefficient of a disk of diameter 600 nm and thickness d =5 nm under plane-wave illumination coming from the top, calculated with BEM for 1098 (red line), 1650 (green line) and 1903 (blue line) boundary points and with COMSOL (black line). (b) Purcell factor calculated for an electric dipole oriented along the x direction, located at a distance z=3 nm from the middle of the top surface of a disk of diameter 50 nm and thickness d =5 nm, calculated for 724 (red line), 1096 (green line) and 1463 (blue line) boundary points, and with COMSOL (black line).

We next analyze, for both disks and for the same excitation conditions, the convergence of the BEM calculations for different 2D electron layer thicknesses. Figure 4.12(a) shows the results for a 2D electron layer thickness of $t = 0.5$ nm, 1nm, and 1.5 nm for the extinction spectra of the disk of diameter 600 nm and thickness $d = 5$ nm under plane-wave illumination, calculated for 1903 boundary points. Similarly, Fig. 4.12(b) displays the Purcell factor for the disk of diameter 50 nm and thickness $d = 5$ nm, for a 2D electron layer thickness $t = 0.5$ nm and 1 nm, under dipolar illumination as in Fig. 4.10 and calculated for 1463 boundary points.

For large disks [Fig. 4.12(a)], we get roughly the same strength and the same position of the peaks as the 2D electron layer thickness is varied. The largest difference is for the lowest-energy peak, with an apparent shift in the peak position for the different peaks. The shift as the thickness is reduced from $t = 1.5$ nm to $t = 1$ nm is relatively small, $\approx$0.79 μm but when it is further reduced from $t = 1$ nm to $t = 0.5$ nm there is a larger shift of $\approx$2 μm. The larger shift of the peaks for $t = 0.5$ nm is likely due to poorer numerical convergence due to the very small thickness of the 2D electron layer. The choice of $t = 1$ nm is a reasonable equilibrium between the choice of thickness and

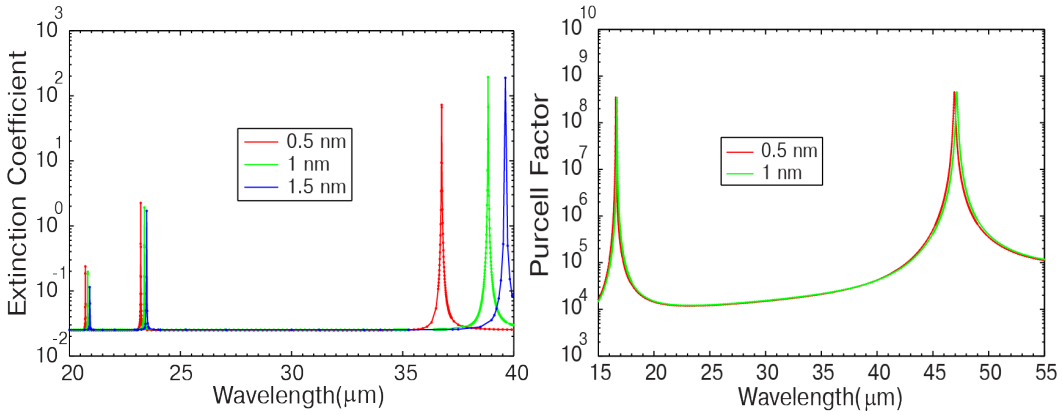

FIGURE 4.12: Convergence of the optical response of topological insulator disks calculated for a fixed number of boundary points using the BEM for different thickness of the 2D electron layer. (a) Extinction coefficient of a disk of diameter 600 nm and thickness $d = 5$ nm under plane-wave illumination incoming from the top calculated using BEM for 1903 boundary points are shown. 2D electron layer thicknesses of 0.5 nm (red line), 1 nm (green line) and 1.5 nm (blue line). (b) Purcell factor for a dipole exciting localized acoustic modes in a disk of diameter 50 nm and thickness $d = 5$ nm calculated using BEM for 1463 boundary points are shown. 2D electron layer thicknesses of 0.5 nm (red line) and 1 nm (green line) are shown.

the convergence with number of boundary points. Notably, this thickness results in a lowest-energy peak very similar to that obtained with COMSOL.

In the case of small disks, we get good convergence, as shown in Fig. 4.12(b). The Purcell factor of the dipole coupled to the small disk is very similar for the two thicknesses $t =$ 0.5 nm and $t = 1$ nm.

Last, we briefly note some aspects of the BEM implementation. In our systems, the 2D electron layer separates the outside vacuum and the dielectric bulk of the topological insulator. Thus, there is a certain freedom to select the value of the background response of the 2D layer [Eq. (4.16)]. We adopted a value of 1, which provided the best convergence.

Furthermore, in the BEM modelling, we have defined the thickness of the disks d as the thickness of the bulk of the topological insulator, without including the finite thickness of the 2D electron layers. This approach also seems to be the favourable for achieving convergence of the results with respect to the 2D electron layer thickness t.

4.4. Summary

We have combined many-body theory and classical electrodynamic calculations to study the excitation of localized and propagating plasmons supported by topological insulator systems. To obtain accurate results we found necessary to take into account the strong non-locality of the response, by considering the dependence of the 2D-conductivity on the wavevector.

Thin topological insulator films support optical and acoustic plasmon modes, and we have studied how the contribution of these two types of modes to the total signal is strongly dependent of the illumination conditions. By changing the distance between a localized source and the film surface, we are able to selectively excite acoustic or optical plasmons in thin-films. Furthermore, we show that, by controlling the geometry and illumination, localized acoustic or optical plasmons can be selectively excited in thin disks of topological insulators at well-defined wavelengths. The low absorption losses in the topological insulator results in very narrow resonance peaks [199–202]. Both charge and spin are strongly confined in the vertical direction and, for the disks, also horizontally, leading to modes of very low volume. Notably, acoustic plasmons are associated with net effective spin and zero charge while net charge and zero spin are found for the optical mode. We thus have demonstrated the large flexibility offered by thin-topological insulators to control spin and charge properties of plasmonic resonances. The very narrow modes supported by the think disks can be easily tuned by changing the geometry or the external voltage, offering an attractive possibility to engineer very compact optoelectronic and spintronic devices.

Appendix A

Fresnel Coefficients for 2-dimensional Systems

In this Appendix we present the derivation of the Fresnel coefficients for two systems supporting 2D electron gases: (i) a plane interface between two dielectric media and (ii) a thin-film.

A.1. A plane interface between two dielectric media supporting a 2D electron gas

We consider a p-polarized plane wave of angular frequency ω incident at a plane interface that supports a 2D electron gas and that separates two dielectric media, medium 1 and medium 2, characterized by relative permittivities ε_1 and ε_2, respectively (Fig. A.1). The 2D electron gas is treated as an in-plane conductivity σ. We consider the interface to be defined by $z = 0$ and the wavevector and electric field to be contained in the $x - z$ plane.

To solve the problem, we consider the incident, reflected and transmitted plane-waves. At any position $\mathbf{r}$ and time t', the incident $\mathbf{E}_i(\mathbf{r}, t')$ and reflected $\mathbf{E}_r(\mathbf{r}, t')$ fields in medium 1 and the transmitted field $\mathbf{E}_t(\mathbf{r}, t')$ in medium 2 are given by

$$\begin{aligned}
\mathbf{E}_i(\mathbf{r}, t') &= \mathrm{E}_i e^{i(-\omega t' + \mathbf{k}_i \cdot \mathbf{r})} \hat{\mathbf{u}}_i = (\mathrm{E}_i \cos\theta_i \hat{\boldsymbol{x}} + \mathrm{E}_i \sin\theta_i \hat{\boldsymbol{z}}) e^{i(-\omega t' + \mathbf{k}_i \cdot \mathbf{r})}, \\
\mathbf{E}_r(\mathbf{r}, t') &= \mathrm{E}_i e^{i(-\omega t' + \mathbf{k}_r \cdot \mathbf{r})} \hat{\mathbf{u}}_r = r_p \left(-\mathrm{E}_i \cos\theta_i \hat{\boldsymbol{x}} + \mathrm{E}_i \sin\theta_i \hat{\boldsymbol{z}}\right) e^{i(-\omega t' + \mathbf{k}_r \cdot \mathbf{r})}, \\
\mathbf{E}_t(\mathbf{r}, t') &= \mathrm{E}_i e^{i(-\omega t' + \mathbf{k}_t \cdot \mathbf{r})} \hat{\mathbf{u}}_t = t_p \left(\mathrm{E}_i \cos\theta_t \hat{\boldsymbol{x}} + \mathrm{E}_i \sin\theta_t \hat{\boldsymbol{z}}\right) e^{i(-\omega t' + \mathbf{k}_t \cdot \mathbf{r})},
\end{aligned} \tag{A.1}$$

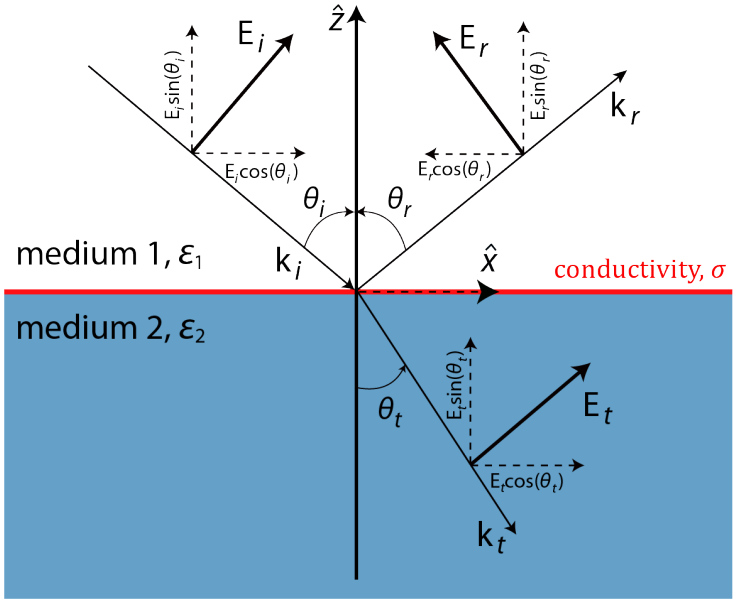

FIGURE A.1: Schematics of the reflection and transmission of a plane wave incident in a plane interface separating two dielectric media characterized by permittivities ε_1 and ε_2 respectively. The interface supports a 2D electron layer of in-plane conductivity σ. E_i, E_r and E_t are the amplitudes and $\mathbf{k}_i$, $\mathbf{k}_r$ and $\mathbf{k}_t$ are the wavevectors of the incident, reflected and transmitted waves respectively. θ_i, θ_r and θ_t are the incident, reflected and transmitted angles, respectively. The amplitudes and the wavevectors can be decomposed into components parallel (along $\hat{\boldsymbol{x}}$) and normal (along $\hat{\boldsymbol{z}}$) to the interface.

where E_i is the amplitude of the incident field and θ_i, θ_r and θ_t are the incident, reflected and transmitted angles respectively. $\hat{\boldsymbol{z}}$ and $\hat{\boldsymbol{x}}$ are the unit vectors normal and parallel to the interface respectively. r_p is the reflection and t_p is the transmission coefficients of the interface. $\hat{\mathbf{u}}_i$, $\hat{\mathbf{u}}_r$ and $\hat{\mathbf{u}}_t$ are the unit vectors along the incident, reflected and transmitted field directions, respectively. The wave number k_j and wavevector $\mathbf{k}_j$ in medium j are given by $k_j = (k_{jx}^2 + k_{jz}^2)^{1/2}$ and $\mathbf{k}_j = k_{jx}\hat{\boldsymbol{x}} \pm k_{jz}\hat{\boldsymbol{z}}$, where k_{jx} and k_{jz} are the x and z components of the wavevector. To verify the boundary conditions for all these equations for all x and t', we need to impose the same k_x and ω for all plane waves. As a consequence, the z component of the wavevector in medium 1, k_{1z}, is the same for the incident and reflected waves and $\theta_i = \theta_r$.

The total field in medium 2, $\mathbf{E}_2(\mathbf{r}, t')$, is the transmitted field. i.e.,

$$\mathbf{E}_2(\mathbf{r}, t') = \mathbf{E}_t(\mathbf{r}, t'). \tag{A.2}$$

In medium 1, the total field can be written as the sum of the incident and the reflected fields as

$$\mathbf{E}_1(\mathbf{r}, t') = \mathbf{E}_i(\mathbf{r}, t') + \mathbf{E}_r(\mathbf{r}, t'). \tag{A.3}$$

The fields at the interface correspond to $z = 0$ and therefore

$$\begin{aligned} \mathbf{E}_1(z = 0, t') &= \mathbf{E}_i(z = 0, t') + \mathbf{E}_r(z = 0, t') \\ &= \mathrm{E}_i[(1 - r_p)\,\cos\theta_i \hat{\boldsymbol{x}} + (1 + r_p)\,\sin\theta_i \hat{\boldsymbol{z}}]\; e^{i(-\omega t' + k_x x)}, \end{aligned} \tag{A.4}$$

and

$$\mathbf{E}_2(z = 0, t') = \mathrm{E}_i t_p\,(\cos\theta_t \hat{\boldsymbol{x}} + \sin\theta_t \hat{\boldsymbol{z}})\;\; e^{i(-\omega t' + k_x x)}. \tag{A.5}$$

On the other hand, the electromagnetic boundary conditions at the interface are [178]

$$\mathrm{E}_1^{\mathrm{x}}(\mathrm{z} = 0, \mathrm{t}') - \mathrm{E}_2^{\mathrm{x}}(\mathrm{z} = 0, \mathrm{t}') = 0, \tag{A.6}$$

$$\mathrm{D}_1^{\mathrm{z}}(\mathrm{z} = 0, \mathrm{t}') - \mathrm{D}_2^{\mathrm{z}}(\mathrm{z} = 0, \mathrm{t}') = \sigma_{\mathrm{c}}, \tag{A.7}$$

where $\mathrm{E}_1^{\mathrm{x}}$ and $\mathrm{E}_2^{\mathrm{x}}$ are the parallel components of the electric fields and $\mathrm{D}_1^{\mathrm{z}} = \varepsilon_0\varepsilon_1\mathrm{E}_1^{\mathrm{z}}$ and $\mathrm{D}_2^{\mathrm{z}} = \varepsilon_0\varepsilon_2\mathrm{E}_2^{\mathrm{z}}$ are the normal components of the electric displacements in medium 1 and medium 2 respectively and σ_c is the surface charge density. ε_0 is the permittivity of vacuum.

Substituting the fields from Eqs. (A.4) and (A.5) in Eq. (A.6) and using $\theta_i = \theta_r$ gives

$$(1 - r_p)\cos\theta_i = t_p \cos\theta_t. \tag{A.8}$$

To evaluate Eq. (A.7) we write σ_c in terms of the fields and the in-plane conductivity σ. The electromagnetic continuity equation is [178]

$$\nabla.\mathbb{J}(\mathbf{r}, t') + \frac{\partial}{\partial t'}\rho(\mathbf{r}, t') = 0. \tag{A.9}$$

where $\mathbb{J}(\mathbf{r}, t')$ and $\rho(\mathbf{r}, t')$ are the volume current and the volume charge densities. At this stage Eq. (A.9) does not need to correspond to monochromatic plane wave illumination. In the case of a 2D conductivity, $\mathbb{J}$ and ρ becomes the surface current $\mathbb{K}$ and surface

charge densities σ_c respectively. Therefore Eq. (A.9) can be written as

$$\nabla.\mathbb{K}(\mathbf{r},t') + \frac{\partial}{\partial t'}\sigma_c(\mathbf{r},t') = 0. \tag{A.10}$$

Since the electric field of the incident plane-wave is confined in the $x-z$ plane, we only need to consider the surface current density along the x direction. For monochromatic plane waves, we write $\mathbb{K}(x,t') = \mathrm{K^x e^{i(k_x\cdot x-\omega t')}}$ and $\sigma_c(x,t') = \sigma_c e^{i(k_x\cdot x-\omega t')}$. We then relate $\mathrm{K^x}$ to the parallel electric field $\mathrm{E^x}$ at the 2D layer as $\mathrm{K^x} = \sigma \mathrm{E^x}$, where σ is a function of k_x for non-local response of the system. Substituting from Eqs. (A.4) and (A.5) in Eq. (A.7) and using $\theta_i = \theta_r$, $\nabla\cdot\mathbf{E}_1 = ik_x\mathrm{E^x e^{-i(\omega t'+kz)}}$ and $\frac{\partial}{\partial t'}\sigma_c = -i\omega\sigma_c$ we obtain

$$\varepsilon_0\varepsilon_1\,(1+r_p)\,\sin\theta_i - \varepsilon_0\varepsilon_2\,t_p\,\sin\theta_t = \frac{\sigma}{\omega}k_x\,(1-r_p)\,\cos\theta_i. \tag{A.11}$$

We could have derived an equation equivalent to Eq. (A.11) by using Eq. (A.5) (medium 2) instead of Eq. (A.4) (medium 1), as $\mathrm{E^x}$ is continuous across the interface.

Eqs. (A.8) and (A.11) can be simplified by substituting the values of $\cos\theta_i = k_{1z}/k_1$, $\cos\theta_t = k_{2z}/k_2$, $\sin\theta_i = k_x/k_1$ and $\sin\theta_t = k_x/k_2$. These equations can be now solved to obtain the reflection r_p and transmission t_p coefficients for the incident p-polarized plane waves incident in a plane interface between two dielectric media characterized by surface conductivity σ as [33]

$$\begin{aligned} r_p &= \frac{\varepsilon_2 k_{1z} - \varepsilon_1 k_{2z} + (\sigma/(\varepsilon_0\omega))k_{1z}k_{2z}}{\varepsilon_2 k_{1z} + \varepsilon_1 k_{2z} + (\sigma/(\varepsilon_0\omega))k_{1z}k_{2z}}, \\ t_p &= \frac{2\varepsilon_1 k_{1z}k_2/k_1}{\varepsilon_2 k_{1z} + \varepsilon_1 k_{2z} + (\sigma/(\varepsilon_0\omega))k_{1z}k_{2z}}. \end{aligned} \tag{A.12}$$

In the case of dielectric media without surface conductivity, Eq. (A.12) reduces to the usual Fresnel coefficients,

$$\begin{aligned} r_p &= \frac{\varepsilon_2 k_{1z} - \varepsilon_1 k_{2z}}{\varepsilon_2 k_{1z} + \varepsilon_1 k_{2z}}, \\ t_p &= \frac{2\varepsilon_1 k_{1z}k_2/k_1}{\varepsilon_2 k_{1z} + \varepsilon_1 k_{2z}}. \end{aligned} \tag{A.13}$$

A.2. Reflection and transmission coefficients in a thin-film supporting two-dimensional electron systems

In this section we derive the reflection and transmission coefficients in a thin-film of thickness d_f that supports a two-dimensional electron system at each interface. A schematic of the different reflection and transmission coefficients is shown in Fig. (A.2). The thin-film of dielectric function ε_2 (medium 2) is sandwiched between two dielectric media characterized by dielectric functions ε_1 (medium 1, top) and ε_3 (medium 3, bottom). The top and bottom interfaces of the thin-film support 2D electron gases, whose optical responses are described by conductivities σ_{12} and σ_{23} respectively. We consider again a p-polarized plane-wave of angular frequency ω and incoming from medium 1 with wavevector components k_x and k_{1z} along the x and z directions respectively.

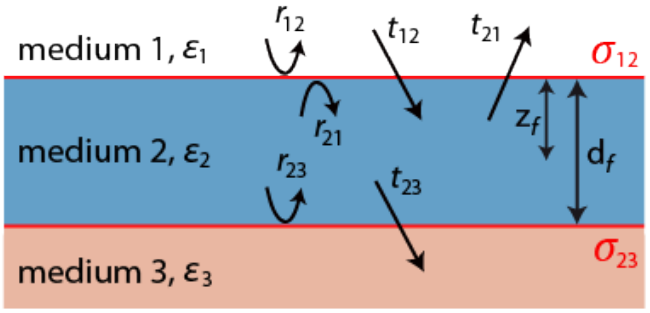

FIGURE A.2: Schematics of the different reflection and transmission coefficients for a plane wave incident on a thin-film. The film has thickness d_f and dielectric constant ε_2 (medium 2) and is sandwiched between medium 1 and medium 3 of dielectric constants ε_1 and ε_3 respectively. r_{mn} is the reflection coefficient and t_{mn} is the transmission coefficient for a planewave travelling from medium m to medium n. The top and the bottom surfaces of medium 2 are characterized by a 2D layer of in-plane conductivities σ_{12} and σ_{23}, respectively. z_f indicates the distance to the top surface when evaluating the fields inside the film.

Following Eq. (A.12), the reflection and transmission coefficients characterizing each interface for a p-polarized plane wave are

$$\begin{aligned}
r_{12} &= \frac{\varepsilon_2 k_{1z} - \varepsilon_1 k_{2z} + (\sigma_{12}/(\varepsilon_0\omega))k_{1z}k_{2z}}{\varepsilon_2 k_{1z} + \varepsilon_1 k_{2z} + (\sigma_{12}/(\varepsilon_0\omega))k_{1z}k_{2z}},\\
r_{21} &= \frac{\varepsilon_1 k_{2z} - \varepsilon_2 k_{1z} + (\sigma_{12}/(\varepsilon_0\omega))k_{1z}k_{2z}}{\varepsilon_1 k_{2z} + \varepsilon_2 k_{1z} + (\sigma_{12}/(\varepsilon_0\omega))k_{1z}k_{2z}},\\
r_{23} &= \frac{\varepsilon_3 k_{2z} - \varepsilon_2 k_{3z} + (\sigma_{23}/(\varepsilon_0\omega))k_{2z}k_{3z}}{\varepsilon_3 k_{2z} + \varepsilon_2 k_{3z} + (\sigma_{23}/(\varepsilon_0\omega))k_{2z}k_{3z}},\\
t_{12} &= \frac{2\varepsilon_1 k_{1z} k_2/k_1}{\varepsilon_2 k_{1z} + \varepsilon_1 k_{2z} + (\sigma_{12}/(\varepsilon_0\omega))k_{1z}k_{2z}},\\
t_{21} &= \frac{2\varepsilon_2 k_{2z} k_1/k_2}{\varepsilon_1 k_{2z} + \varepsilon_2 k_{1z} + (\sigma_{12}/(\varepsilon_0\omega))k_{1z}k_{2z}},\\
t_{23} &= \frac{2\varepsilon_2 k_{2z} k_3/k_2}{\varepsilon_3 k_{2z} + \varepsilon_2 k_{3z} + (\sigma_{23}/(\varepsilon_0\omega))k_{3z}k_{2z}},
\end{aligned} \tag{A.14}$$

where r_{mn} and t_{mn} are the reflection and transmission coefficients for a plane-wave incoming from medium m into the interface with medium n and k_{mz} is the normal component of the plane-waves with wavenumber k_m in the respective medium m. The total reflected field by the film can be written as the sum of the field directly reflected from the top interface and the field components that experience a different number of reflections inside the thin-film before being reflected back to medium 1. At the top interface between medium 1 and medium 2 the amplitude of the reflected field equals

$$\begin{aligned}
\mathrm{E}_{ref} &= r_{12}\mathrm{E}_i + t_{12}r_{23}t_{21}e^{2ik_{2z}d_f}\sum_{n=0}^{\infty}\left(r_{23}r_{21}e^{2ik_{2z}d_f}\right)^n \mathrm{E}_i\\
&= r_{12}\mathrm{E}_i + \frac{t_{12}r_{23}t_{21}e^{2ik_{2z}d_f}}{1 - r_{23}r_{21}e^{2ik_{2z}d_f}}\mathrm{E}_i,
\end{aligned} \tag{A.15}$$

and the corresponding reflection coefficient of the film r_p^{film}, $\mathrm{E}_{ref} = r_p^{film}\mathrm{E}_i$, is

$$r_p^{film} = r_{12} + \frac{t_{12}r_{23}t_{21}e^{2ik_{2z}d_f}}{1 - r_{21}r_{23}e^{2ik_{2z}d_f}}. \tag{A.16}$$

We can write in a similar way, the transmitted field at the bottom interface between medium 2 and 3,

$$\begin{aligned}
\mathrm{E}_3 &= t_{12}t_{23}e^{ik_{2z}d_f}\sum_{n=0}^{\infty}\left(r_{23}r_{21}e^{2ik_{2z}d_f}\right)^n \mathrm{E}_i\\
&= \frac{t_{12}t_{23}e^{ik_{2z}d_f}}{1 - r_{23}r_{21}e^{2ik_{2z}d_f}}\mathrm{E}_i = t_p^{film}\mathrm{E}_i e^{ik_{2z}d_f}.
\end{aligned} \tag{A.17}$$

Therefore, the transmission coefficient of the film t_p^{film} for the p-polarized plane wave incoming from medium 1 is given by

$$t_p^{film} = \frac{t_{12}t_{23}}{1 - r_{23}r_{21}e^{2ik_{2z}d_f}}. \tag{A.18}$$

The fields in medium 1 and medium 3 can then be obtained using Eqs. (A.1) - (A.3) by inserting the corresponding reflection r_p^{film} and transmission t_p^{film} coefficients of the film from Eqs. (A.16) and (A.18).

A.2.1. Electric fields inside the film

We proceed next to calculate the electric field inside the film, $\mathbf{E}_2$.

$$\begin{aligned}\mathbf{E}_2(\mathbf{r},t') &= \mathrm{E}_{layer}^{up}(\mathbf{r},t')e^{i(-\omega t'+\mathbf{k}_{up}\cdot\mathbf{r})}\hat{\mathbf{u}}_{up} + \mathrm{E}_{layer}^{down}(\mathbf{r},t')e^{i(-\omega t'+\mathbf{k}_{down}\cdot\mathbf{r})}\hat{\mathbf{u}}_{down} \\ &= \mathrm{E}_{layer}^{up}(-\cos\theta_t\hat{\boldsymbol{x}} + \sin\theta_t\hat{\boldsymbol{z}})e^{i(-\omega t'+\mathbf{k}_{up}\cdot\mathbf{r})} \\ &+ \mathrm{E}_{layer}^{down}(\cos\theta_t\hat{\boldsymbol{x}} + \sin\theta_t\hat{\boldsymbol{z}})e^{i(-\omega t'+\mathbf{k}_{down}\cdot\mathbf{r})},\end{aligned} \tag{A.19}$$

where θ_t the angle of transmission for a plane wave entering from medium 1 to medium 2 and $\mathbf{k}_{up}$ and $\mathbf{k}_{down}$ are the wavevectors of the planewaves propagating upward in medium 2 (towards medium 1, amplitude E_{layer}^{up}) and downward (towards medium 3, amplitude $\mathrm{E}_{layer}^{down}$) directions respectively. $\hat{\mathbf{u}}_{up}$ and $\hat{\mathbf{u}}_{down}$ are the corresponding unit vectors indicating the polarization of the fields. Both E_{layer}^{up} and $\mathrm{E}_{layer}^{down}$ can be calculated taking into account the possibility of multiple reflection inside the film before the energy is absorbed or emitted towards medium 1 or medium 3.

For the plane-wave propagating upward:

$$\mathrm{E}_{layer}^{up} = \frac{\mathrm{E}_i t_{12}r_{23}\ e^{2ik_{2z}d_f}}{1 - r_{23}r_{21}e^{2ik_{2z}d_f}}e^{-ik_{2z}z_f}, \tag{A.20}$$

where z_f is the distance from the top interface to the point where the field is evaluated (Fig. A.2). Similarly for the field propagating downwards,

$$\mathrm{E}_{layer}^{down} = \frac{\mathrm{E}_i t_{12}}{1 - r_{23}r_{21}\ e^{2ik_{2z}d_f}}e^{ik_{2z}z_f}. \tag{A.21}$$

We then write the total field at any point inside the film as

$$\mathbf{E}_2 = C_{up}\ \mathrm{E}_i\ \hat{\mathbf{u}}_{up} + C_{down}\ \mathrm{E}_i\ \hat{\mathbf{u}}_{down}, \tag{A.22}$$

where

$$C_{up} = \frac{t_{12} r_{23} \ e^{2ik_{2z}d_f}}{1 - r_{23} r_{21} e^{2ik_{2z}d_f}} e^{-ik_{2z}z_f}, \tag{A.23}$$

and

$$C_{down} = \frac{t_{12}}{1 - r_{23} r_{21} \ e^{2ik_{2z}d_f}} e^{ik_{2z}z_f}. \tag{A.24}$$

Appendix B

Plane-wave Decomposition Method

In Chapter 4 we use the plane-wave decomposition method to calculate the electric field induced by a dipole placed on top of a semi-infinite substrate and a thin-film. The field directly emitted by an electric dipole $\boldsymbol{p}$ situated at $\mathbf{r}_0 = (0, 0, z_{dip})$ in a homogeneous medium characterized by dielectric permittivity ε_1 can be calculated at a position $\mathbf{r}(x, y, z)$ from the simple analytical equation [179].

$$\mathbf{E}_{inc}(\mathbf{r}) = \frac{1}{4\pi\varepsilon_0\varepsilon_1}\Bigg\{k^2(\hat{\mathbf{u}}\times\boldsymbol{p})\times\hat{\mathbf{u}}\frac{e^{i\mathbf{k}\cdot(\mathbf{r}-\mathbf{r}_0)}}{|\mathbf{r}-\mathbf{r}_0|}+ \\ [3\hat{\mathbf{u}}(\hat{\mathbf{u}}.\boldsymbol{p})-\boldsymbol{p}]\left(\frac{1}{|\mathbf{r}-\mathbf{r}_0|^3}-\frac{ik}{|\mathbf{r}-\mathbf{r}_0|^2}\right)e^{i\mathbf{k}\cdot(\mathbf{r}-\mathbf{r}_0)}\Bigg\}, \tag{B.1}$$

where ε_0 is the permittivity of free space, $\mathbf{k}$ is the wavevector and $\hat{\mathbf{u}}$ is the unit vector along the direction of propagation. We are interested in the reflected and transmitted fields, and for the case of a thin-film, the field inside the film produced by the dipole. Here we follow Ref. [178] to provide detailed derivations of the expressions for a dipole oriented in the direction normal to the surface.

B.1. Electric field of an electric dipole

According to the plane-wave decomposition method, the electric field radiated by an electric dipole can be expressed as an integral of the fields generated by different plane-wave components. The electric field at position $\mathbf{r}$ due to a point electric dipole located at $\mathbf{r}_0$ and emitting at angular frequency ω is then given by

$$\mathbf{E}(\mathbf{r}) \;=\; \omega^2\mu_0\mu_1\overleftrightarrow{\mathbf{G}}_0(\mathbf{r},\mathbf{r}_0)\boldsymbol{p}, \tag{B.2}$$

where μ_0 and μ_1 are the magnetic permeability and relative magnetic permeability of the medium, respectively, and $\overleftrightarrow{\mathbf{G}}_0(\mathbf{r},\mathbf{r}_0)$ is the Dyadic Green's function, that can be decomposed into plane-waves propagating either upwards or downwards as:

$$\overleftrightarrow{\mathbf{G}}_0(\mathbf{r},\mathbf{r}_0) \;=\; \frac{i}{8\pi^2}\int_{-\infty}^{\infty}\int_{-\infty}^{\infty}\overleftrightarrow{\mathbf{M}}e^{i[k_x x+k_y y+k_{1z}|z-z_{dip}|]}dk_x dk_y \tag{B.3}$$

where k_x, k_y and $k_{1z}=(k_1^2-(k_x^2+k_y^2))^{1/2}$ are the components of the wavevector k_1 along x, y and z directions, in the medium in which the dipole is situated (medium 1) $[\mathbf{k}_1 = k_x\hat{\boldsymbol{x}}+k_y\hat{\boldsymbol{y}}\pm k_{1z}\hat{\boldsymbol{z}}]$. The value of $\overleftrightarrow{\mathbf{M}}$ is given by

$$\overleftrightarrow{\mathbf{M}} = \frac{1}{k_1^2 k_{1z}}\begin{bmatrix} k_1^2-k_x^2 & -k_xk_y & \mp k_xk_{1z} \\ -k_xk_y & k_1^2-k_y^2 & \mp k_yk_{1z} \\ \mp k_xk_{1z} & \mp k_yk_{1z} & k_1^2-k_{1z}^2 \end{bmatrix}, \tag{B.4}$$

where the upper sign is used when considering plane-waves propagating upwards (towards $z > d_{dip}$) and the lower sign is used for components propagating downwards (towards $z < z_{dip}$). We notice that, for our purposes, it will be enough to focus either on only upwards or only downwards propagating plane-waves. When the dipole is oriented along the z direction (p_z), the electric field at any position is purely p-polarized, and is given by

$$\begin{aligned}\mathbf{E}(\mathbf{r}) &= \omega^2\mu_0\mu_1\overleftrightarrow{\mathbf{G}}_0(\mathbf{r},\mathbf{r}_0)\begin{bmatrix}0\\0\\p_z\end{bmatrix} \\ &= \frac{i\omega^2\mu_0\mu_1}{8\pi^2k_1^2}p_z\int_{-\infty}^{\infty}\int_{-\infty}^{\infty}\begin{bmatrix}\mp k_x\\ \mp k_y\\ (k_x^2+k_y^2)/k_{1z}\end{bmatrix}e^{i[k_x x+k_y y+k_{1z}|z-z_{dip}|]}dk_x dk_y.\end{aligned} \tag{B.5}$$

Following Fig. B.1, we substitute in Eq. (B.5), $k_x = q\cos\theta$, $k_y = q\sin\theta$, $x = \rho\cos\phi$, $y = \rho\sin\phi$ and $dk_x dk_y = qdqd\theta$, where θ and ϕ are the angles of the wavevector q and the position vector ρ with the x axis. By doing it, we obtain:

$$\mathbf{E}(\mathbf{r}) = \frac{i\omega^2\mu_0\mu_1}{8\pi^2 k_1^2} p_z \int_{q=0}^{\infty} q^2\, e^{ik_z|z-z_{dip}|} \left(\int_{\theta=0}^{2\pi} \begin{bmatrix} \mp\cos\theta \\ \mp sin\theta \\ q/k_{1z} \end{bmatrix} e^{i\rho q\,\cos(\theta-\phi)} d\theta \right) dq. \tag{B.6}$$

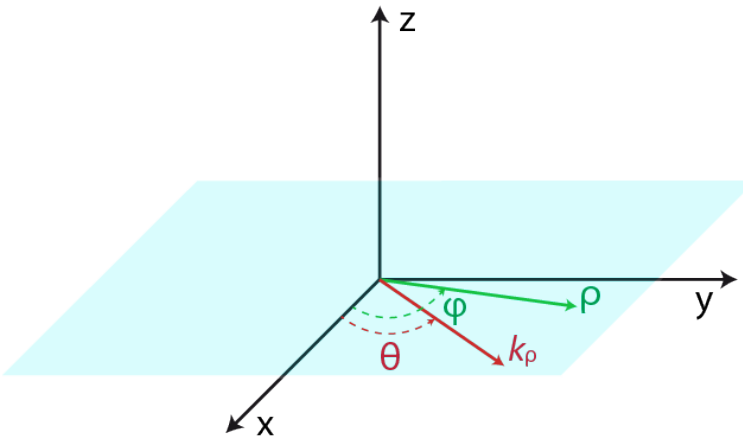

FIGURE B.1: Schematics of the coordinate system used to evaluate the integrals in Eq. (B.5).

After the change of variables $\theta - \phi = \alpha$, Eq. (B.6) becomes

$$\mathbf{E}(\mathbf{r}) = \frac{i\omega^2\mu_0\mu_1}{8\pi^2 k_1^2} p_z \int_{q=0}^{\infty} q^2 e^{ik_z|z-z_{dip}|} \left(\int_{\alpha=-\pi}^{\pi} \begin{bmatrix} \mp\cos(\alpha+\phi) \\ \mp sin(\alpha+\phi) \\ q/k_{1z} \end{bmatrix} e^{i\rho q\,\cos\alpha} d\alpha \right) dq, \tag{B.7}$$

where in the second integral we can take any interval comprising 2π due to the periodicity of the function with α. We use Bessel functions [214] for the numerical integration of Eq. (B.7). As an example, the x component of the field corresponds to

$$\mathrm{E}_x(\mathbf{r}) = \mp\frac{i\omega^2\mu_0\mu_1}{8\pi^2 k_1^2} p_z \int_{q=0}^{\infty} q^2\, e^{ik_z|z-z_{dip}|} \left(\int_{\alpha=-\pi}^{\pi} \cos(\alpha+\phi) e^{i\rho q[\cos\alpha]} d\alpha \right) dq, \tag{B.8}$$

where the integration over α can be simplified as

$$\begin{aligned}\int_{\alpha=-\pi}^{\pi} \cos(\alpha+\phi)\, e^{i\rho q[\cos\alpha]} d\alpha = & \int_{\alpha=-\pi}^{\pi} \cos\alpha\cos\phi\ e^{i\rho q[\cos\alpha]} d\alpha \\ & - \int_{\alpha=-\pi}^{\pi} sin\alpha\, sin\phi\ e^{i\rho q[\cos\alpha]} d\alpha \\ & = \cos\phi \int_{\alpha=-\pi}^{\pi} \cos\alpha\ e^{i\rho q[\cos\alpha]} d\alpha,\end{aligned} \tag{B.9}$$

where integral $\int_{\alpha=-\pi}^{\pi} sin\alpha\, sin\phi\, e^{i\rho q[\cos\alpha]} d\alpha = 0$ because it is antisymmetric with respect to $\alpha = 0$. Equation (B.9) can then be written using the Bessel function of first kind $J_1(\rho q)$ [214], as

$$\int_{\alpha=-\pi}^{\pi} \cos(\alpha+\phi) e^{i\rho q[\cos\alpha]} d\alpha = \cos\phi\,[\,2\pi i J_1(\rho q)\,]\,. \tag{B.10}$$

Substituting Eq. (B.10) in Eq. (B.8) the x component of the field can finally be obtained

$$\mathrm{E}_x(\mathbf{r}) = \mp \frac{i\omega^2\mu_0\mu_1}{8\pi^2 k_1^2} p_z \int_{q=0}^{\infty} q^2 e^{ik_z|z-z_{dip}|} \cos\phi\,[2\pi i J_1(\rho q)]\, dq. \tag{B.11}$$

Following similar steps the y and z components of the dipole can be obtained as

$$\mathrm{E}_y(\mathbf{r}) = \mp \frac{i\omega^2\mu_0\mu_1}{8\pi^2 k_1^2} p_z \int_{q=0}^{\infty} q^2\ e^{ik_z|z-z_{dip}|} sin\phi\ 2\pi i\,[J_1(\rho q)]\, dq, \tag{B.12}$$

$$\mathrm{E}_z(\mathbf{r}) = \frac{i\omega^2\mu_0\mu_1}{8\pi^2 k_1^2} p_z \int_{q=0}^{\infty} \frac{q^3}{k_{1z}}\, e^{ik_z|z-z_{dip}|}\,[2\pi J_0(\rho q)]\, dq, \tag{B.13}$$

where $J_0(\rho q)$ is the Bessel function of first kind [214]. As previously described, the $+$ sign in Eqs. (B.11) and (B.12) applies when integrating over the plane-waves propagating in the $-z$ direction and the $-$ sign corresponds to the plane-waves propagating in the $+z$ direction.

B.2. Fields induced by a dipole placed over a semi-infinite substrate

We now consider the same dipole situated above a plane interface ($z = 0$) separating medium 1 and medium 2. The total field at a given point in medium 1 where the dipole is situated is given by the sum of the incoming field of the dipole and the field reflected by the interface. The incoming field at a position $\mathbf{r}$ is given by Eq. B.1.

The x, y and z components E_{rx}, E_{ry} and E_{rz} of the field reflected by the interface can be obtained by taking into account that each plane-wave integrals is reflected as described in Eqs. (B.11) - (B.13) by the q dependent reflection coefficient r_p [Eq. (A.12)]. Therefore,

$$\begin{aligned}
\mathrm{E}_{rx}(\mathbf{r}) &= -\frac{i\omega^2\mu_0\mu_1}{8\pi^2 k_1^2} p_z \int_{q=0}^{\infty} r_p(q) q^2 e^{ik_{1z}|z_{dip}+z|} \cos\phi \, [2\pi i J_1(\rho q)] \, dq, \\
\mathrm{E}_{ry}(\mathbf{r}) &= -\frac{i\omega^2\mu_0\mu_1}{8\pi^2 k_1^2} p_z \int_{q=0}^{\infty} r_p(q) q^2 e^{ik_{1z}|z_{dip}+z|} sin\phi \, [2\pi i J_1(\rho q)] \, dq, \\
\mathrm{E}_{rz}(\mathbf{r}) &= \frac{i\omega^2\mu_0\mu_1}{8\pi^2 k_1^2} p_z \int_{q=0}^{\infty} r_p(q) \frac{q^3}{k_{1z}} \, e^{ik_{1z}|z_{dip}+z|} \, [2\pi J_0(\rho q)] \, dq.
\end{aligned} \tag{B.14}$$

Notice that here and in the following of this Appendix, we have been able to obtain the desired equations by slight modifications of Eqs. (B.11) - (B.13), which were derived after integrating over alpha, because the extra terms that needs to be included (such as r_p) are independent of α. $z_{dip} + z$ appears in the exponential because it corresponds to the optical path followed by each reflected plane-wave.

In a similar manner to Eq. (B.14), the transmitted field components E_{tx}, E_{ty} and E_{tz} can be written as

$$\begin{aligned}
\mathrm{E}_{tx}(\mathbf{r}) &= \frac{i\omega^2\mu_0\mu_1}{8\pi^2 k_1 k_2} p_z \int_{q=0}^{\infty} \frac{t_p q^2 k_{2z}}{k_{1z}} e^{i(k_{1z}|z_{dip}|+k_{2z}|z|)} \cos\phi \, [2\pi i J_1(\rho q)] \, dq, \\
\mathrm{E}_{ty}(\mathbf{r}) &= \frac{i\omega^2\mu_0\mu_1}{8\pi^2 k_1 k_2} p_z \int_{q=0}^{\infty} \frac{t_p q^2 k_{2z}}{k_{1z}} e^{i(k_{1z}|z_{dip}|+k_{2z}|z|)} sin\phi \, \, [2\pi i J_1(\rho q)] \, dq, \\
\mathrm{E}_{tz}(\mathbf{r}) &= \frac{i\omega^2\mu_0\mu_1}{8\pi^2 k_1 k_2} p_z \int_{q=0}^{\infty} \frac{t_p q^3}{k_{1z}} \, e^{i(k_{1z}|z_{dip}|+k_{2z}|z|)} \, [2\pi J_0(\rho q)] \, dq,
\end{aligned} \tag{B.15}$$

where t_p is the transmission coefficient from Eq. (A.12) and $1/k_1^2$ is replaced by $k_{2z}/(k_1 k_2 k_{1z})$ in Eqs. (B.11) and (B.12) and by $1/(k_1 k_2)$ in (B.13) to account for the change on the direction of the field for each plane-wave due to the different dielectric medium. k_2 is the wavevector of the transmitted component and k_{2z} its z component.

B.3. Fields induced by a dipole placed over a thin-film

The electric fields of the dipole reflected by a thin-film are also given by Eq. (B.14), with the only difference that the reflection coefficient of the film from Eq. (A.16) must be

used. Similarly, the transmitted fields are obtained by modifying Eq. (B.15) to obtain

$$\begin{aligned}
&\mathrm{E}_{tx}(\mathbf{r}) \\
&= \frac{i\omega^2\mu_0\mu_1}{8\pi^2 k_1 k_3} p_z \int_{q=0}^{\infty} \frac{t_p^{film}\, q^2 k_{3z}}{k_{1z}} e^{i(k_{1z}|z_{dip}|+k_{3z}|z+d_f|+k_{2z}d_f)} \cos\phi \, [2\pi i J_1(\rho q)]\, dq, \\
&\mathrm{E}_{ty}(\mathbf{r}) \\
&= \frac{i\omega^2\mu_0\mu_1}{8\pi^2 k_1 k_3} p_z \int_{q=0}^{\infty} \frac{t_p^{film}\, q^2 k_{3z}}{k_{1z}} e^{i(k_{1z}|z_{dip}|+k_{3z}|z+d_f|+k_{2z}d_f)} sin\phi \;\; [2\pi i J_1(\rho q)]\, dq, \\
&\mathrm{E}_{tz}(\mathbf{r}) \\
&= \frac{i\omega^2\mu_0\mu_1}{8\pi^2 k_1 k_3} p_z \int_{q=0}^{\infty} \frac{t_p^{film}\, q^3}{k_{1z}} \, e^{i(k_{1z}|z_{dip}|+k_{3z}|z+d_f|+k_{2z}d_f)} \, [2\pi J_0(\rho q)]\, dq,
\end{aligned} \tag{B.16}$$

where d_f is the thickness of the layer and t_p^{film} is the transmission coefficient of the film given by equation (A.18). The term in the exponential again simply takes into account the phase propagation for each plane-wave ($z < -d_f$).

In Appendix A we consider the total field at a point for a single plane-wave inside the film, at a distance z_f from the top layer, as the sum of the field components propagating upwards and downwards. Here, we can proceed in a similar manner integrating over all the components. The x, y and z components E_x^{up}, E_y^{up} and E_z^{up} of the field propagating upwards is given by

$$\begin{aligned}
\mathrm{E}_x^{up}(\mathbf{r}) &= -\frac{i\omega^2\mu_0\mu_1}{8\pi^2 k_1 k_2} p_z \int_{q=0}^{\infty} \frac{C_{up}\, q^2 k_{2z}}{k_{1z}} e^{ik_{1z}z_{dip}} \cos\phi \, [2\pi i J_1(\rho q)]\, dq, \\
\mathrm{E}_y^{up}(\mathbf{r}) &= -\frac{i\omega^2\mu_0\mu_1}{8\pi^2 k_1 k_2} p_z \int_{q=0}^{\infty} \frac{C_{up}\, q^2 k_{2z}}{k_{1z}} e^{ik_{1z}z_{dip}} sin\phi \;\; [2\pi i J_1(\rho q)]\, dq, \\
\mathrm{E}_z^{up}(\mathbf{r}) &= \frac{i\omega^2\mu_0\mu_1}{8\pi^2 k_1 k_2} p_z \int_{q=0}^{\infty} \frac{C_{up}\, q^3}{k_{1z}} \, e^{ik_{1z}z_{dip}} \, [2\pi J_0(\rho q)]\, dq,
\end{aligned} \tag{B.17}$$

where C_{up}, defined in Eq. (A.23). In a similar way, the components E_x^{down}, E_y^{down} and E_z^{down} of the field due to the plane waves propagating downwards is given by

$$\begin{aligned}
\mathrm{E}_x^{down}(\mathbf{r}) &= \frac{i\omega^2\mu_0\mu_1}{8\pi^2 k_1 k_2} p_z \int_{q=0}^{\infty} \frac{C_{down}\, q^2 k_{2z}}{k_{1z}} e^{ik_{1z}z_{dip}} \cos\phi \, [2\pi i J_1(\rho q)]\, dq, \\
\mathrm{E}_y^{down}(\mathbf{r}) &= \frac{i\omega^2\mu_0\mu_1}{8\pi^2 k_1 k_2} p_z \int_{q=0}^{\infty} \frac{C_{down}\, q^2 k_{2z}}{k_{1z}} e^{ik_{1z}z_{dip}} sin\phi \;\; [2\pi i J_1(\rho q)]\, dq, \\
\mathrm{E}_z^{down}(\mathbf{r}) &= \frac{i\omega^2\mu_0\mu_1}{8\pi^2 k_1 k_2} p_z \int_{q=0}^{\infty} \frac{C_{down}\, q^3}{k_{1z}} \, e^{ik_{1z}z_{dip}} \, [2\pi J_0(\rho q)]\, dq,
\end{aligned} \tag{B.18}$$

where C_{down} corresponds to Eq. (A.24). To derive these equations, we again considered

the different direction of the electric field inside the film compared to that of medium 1. The evolution of the phase inside the film is contained in the expressions of C_{up} and C_{down}. The total field inside the film is thus obtained by the sum of fields given by Eq. (B.17) and (B.18).

Appendix C

Effective Medium Approximations

The optical response of bulk materials is the result of the polarizability of the individual microscopic entities, for example, atoms and molecules. A macroscopic dielectric response of the material can be obtained by defining a bulk dielectric function, which is the result of spatial averaging of the local microscopic response. In this case, since the size of the microscopic entities is much smaller than the wavelength of the electromagnetic radiation, the material can be considered as homogeneous. Therefore the response of the whole medium can be defined by using a homogeneous bulk dielectric function.

In a similar manner, in the case of composite materials consisting of domains of two or more different materials with distinct bulk dielectric responses and of characteristic dimensions sufficiently smaller than the wavelength, the response of the whole medium can be obtained, under adequate circumstances, through statistical averaging of the responses of the individual domains. Depending on the size and shape of the domains and the composition, different statistical averaging techniques, called effective medium approximations or effective medium theories [52, 163, 215] are applied.

In chapter 2, in order to describe the dielectric response of inhomogeneous palladium hydride consisting of α and β phase domains, we employed Bruggeman's effective medium approximation. Here we give a brief overview of this model, and compare it with the widely used Maxwell-Garnett approximation.

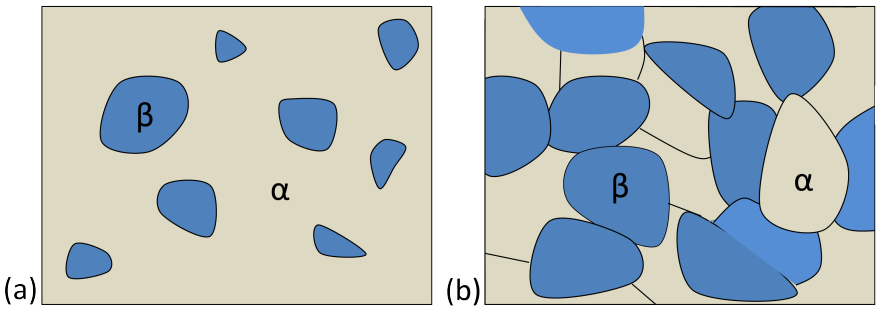

FIGURE C.1: Fig: Schematic representation of two different domain structures for a two-phase inhomogeneous material composed of (a) a relatively small fraction of the β phase which is incorporated as separated inclusions into a matrix, the α phase, and (b) an aggregate structure with similar fraction of the two phases. ε_α and ε_β are the macroscopic dielectric function of the locally homogeneous α and β phases, respectively.

It is useful to consider two different domain structures, shown in Fig. C.1, when discussing inhomogeneous materials. Both domains are composed by two different materials, characterized by homogeneous dielectric functions ε_α and ε_β. The key parameter f_β is the filling factor of the medium (here the volume fraction of the β phase domains). Maxwell Garnett [165] and Bruggeman's [162, 163] effective medium theories are used, taking into account the domain structure and the filling factor f_β (for example, the volume fraction of β phase domains) of the medium. In Fig. C.1(a) the β phase domains can be seen as inclusions that are spatially separated and randomly dispersed, with a relatively low filling factor, in a continuous matrix of α phase. The effective dielectric response of materials showing this structure, for spherical like inclusions with filling factor f_β, can be obtained using the Maxwell Garnett effective medium theory: [215, 216]

$$\varepsilon_{MG} = \varepsilon_\alpha \frac{\varepsilon_\beta + 2\varepsilon_\alpha + 2f_\beta(\varepsilon_\beta - \varepsilon_\alpha)}{\varepsilon_\beta + 2\varepsilon_\alpha - f_\beta(\varepsilon_\beta - \varepsilon_\alpha)}, \tag{C.1}$$

where ε_{MG} is the Maxwell Garnett effective dielectric function.

It can be seen that Eq. (C.1) is changed if we model the material, as inclusions of β phase with filling fractions f_β, or as α-phase inclusions with filling fraction $1 - f_\beta$. Therefore, this description means that the roles of the two phases are different, and the α phase must correspond to the matrix that occupies most of the volume. Maxwell Garnett effective medium theory is suitable for describing only materials in which the filling fraction of the inclusion [the beta phase in Eq. (C.1)] is small, and the approximation breaks for higher filling fractions of the inclusion close to 0.5, where it becomes impossible to distinguish between the inclusion and the matrix.

In the case of palladium hydride, the filling fraction f_β of the β phase PdH domains becomes high for high hydrogen concentrations, coming closer to the domain structure schematically shown in Fig. C.1(b). Maxwell Garnett theory is thus not appropriate, and we define the effective dielectric response using Bruggeman's effective medium theory that is more appropriate to describe equal filling fractions [217, 218]. In this description, we need then to solve:

$$f_\beta \frac{\varepsilon_\beta - \varepsilon_{Br}}{\varepsilon_\beta + 2\varepsilon_{Br}} + (1 - f_\beta) \frac{\varepsilon_\alpha - \varepsilon_{Br}}{\varepsilon_\alpha + 2\varepsilon_{Br}} = 0, \tag{C.2}$$

where ε_{Br} is the Bruggeman's effective dielectric function. In this approach, the inclusion and the matrix are treated in an identical manner, i.e. Eq (C.2) is invariant if the inclusion and the matrix are interchanged along with their corresponding filling fractions. This property constitute a key difference with the previous Maxwell Garnett approximation, as in the latter the matrix and the inclusion were strictly defined and could not be interchanged.

Maxwell-Garnett and Bruggeman's effective medium theories show some limitations connected with the description of extreme situations. For instance, both approximations considered some simplification in terms of the size and physical nature of the inclusions. When the size of the inclusions is very small, their dielectric response cannot be defined using a macroscopic dielectric function. On the other hand, the model assumes simple electric dipolar interaction between domains. Notably, when the size of the domains is large enough or when different domains interact very strongly, this approach is not valid. The effective medium approximations can be extended in some cases to incorporate higher order multipolar interactions [215, 217].

Bibliography

[1] Albert Van Helden. The invention of the telescope. *Amer. Philos. Soc., New Series*, 7:1–67 (1977).

[2] Albert Van Helden, Sven Dupré, Rob van Gent, and Huib Zuidervaart. *The origins of the telescope*. KNAW Press, Amsterdam, 2010.

[3] Samuel Hoole. *The select works of Antony van Leeuwenhoek: Containing his microscopical discoveries in many of the works of nature*. The Philandhropic Society, London, 1800.

[4] Robert Hooke. *Micrographia: or Some Physiological Descriptions of Minute Bodies Made by Magnifying Glasses with Observations and Inquiries Thereupon*. Royal Society of London, 1665.

[5] Isaac Newton. *Opticks or, a Treatise of the Reflections, Refractions, Inflections, and Colours of Light, 4th Ed.* William Innys at the West-End of St. Paul's. Mdccxxx., London., 1730.

[6] Christiaan Huygens. *Treatise on light*. Leiden, 1690.

[7] A. Einstein. On a heuristic point of view about the creation and conversion of light. *Ann. Phys.*, 322:132–148 (1905).

[8] Nikolay I. Zheludev. What diffraction limit? *Nat. Mater.*, 7:420–422 (2008).

[9] D. K. Gramotnev and S. I. Bozhevolnyi. Plasmonics beyond the diffraction limit. *Nat. Photon.*, 4:1749 (2010).

[10] E. Betzig and J. K. Trautman. Near-field optics microscopy spectroscopy and surface modification beyond the diffraction limit. *Science*, 257(5067):189–195 (1992).

[11] S. L. McCall, A. F. J. Levi, R. E. Slusher, S. J. Pearton, and R. A. Logan. Whispering-gallery mode microdisk lasers. *Appl. Phys. Lett.*, 60:289–291 (1992).

[12] R. D. Richtmyer. Dielectric resonators. *J. Appl. Phys.*, 10(6):391–398 (1939).

[13] K. J. Vahala. Optical microcavities. *Nature*, 424:839–846 (2003).

[14] V. I. Klimov, A. A. Mikhailovsky, Su Xu, A. Malko, J. A. Hollingsworth, C. A. Leatherdale, H.-J. Eisler, and M. G. Bawendi. Optical gain and stimulated emission in nanocrystal quantum dots. *Science*, 290(5490):314–317 (2000).

[15] O. Stier, M. Grundmann, and D. Bimberg. Electronic and optical properties of strained quantum dots modeled by 8-band k-p theory. *Phys. Rev. B*, 59:5688–5701 (1999).

[16] X. Michalet, F. F. Pinaud, L. A. Bentolila, J. M. Tsay, S. Doose, J. J. Li, G. Sundaresan, A. M. Wu, S. S. Gambhir, and S. Weiss. Quantum dots for live cells, in vivo imaging, and diagnostics. *Science*, 307(5709):538–544 (2005).

[17] E. Ozbay. Plasmonics: Merging photonics and electronics at nanoscale dimensions. *Science*, 311(5758):189–193 (2006).

[18] S. A. Maier, M. L. Brongersma, P. G. Kik, S. Meltzer, A. A. G. Requicha, and H. A. Atwater. Plasmonics-a route to nanoscale optical devices. *Adv. Mater.*, 13 (19):1501–1505 (2001).

[19] J. A. Schuller, E. S. Barnard, W. Cai, Y. C. Jun, J. S. White, and M. L. Brongersma. Plasmonics for extreme light concentration and manipulation. *Nat. Mater.*, 9(19):193–204 (2010).

[20] M. Pelton, J. Aizpurua, and G. Bryant. Metal-nanoparticle plasmonics. *Laser Photon. Rev.*, 2(3):136–159 (2008).

[21] R. K. Mongia and P. Bhartia. Dielectric resonator antennas- a review and general design relations for resonant frequency and bandwidth. *Int. J. Microwave. Mill.*, 4(3):230–247 (1994).

[22] A. Ittipiboon, M. Cuhaci, R. K. Mongia, P. Bhartia, and Y. M. M. Antar. Aperture fed rectangular and triangular dielectric resonators for use as magnetic dipole antennas. *Electron. Lett.*, 29:2001–2002 (1993).

[23] A. Boltasseva and H. A. Atwater. Low-loss plasmonic metamaterials. *Science*, 331 (6015):290–291 (2011).

[24] J. Chen, P. Albella, Z. Pirzadeh, P. Alonso-Gonzalez, F. Huth, S. Bonetti, V. Bonanni, J. Akerman, J. Nogues, P. Vavassori, A. Dmitriev, J. Aizpurua, and R. Hillenbrand. Plasmonic nickel nanoantennas. *Small*, 7(16):2341–2347 (2011).

[25] R. Li, W. Chen, H. Kobayashi, and C. Ma. Platinum-nanoparticle-loaded bismuth oxide: an efficient plasmonic photocatalyst active under visible light. *Green Chem.*, 12:212–215 (2010).

[26] C. Langhammer, Z. Yuan, I. Zorić, and B. Kasemo. Plasmonic properties of supported pt and pd nanostructures. *Nano Lett.*, 6(4):833–838 (2006).

[27] J. C. Banthi, D. Meneses-Rodriguez, F. Garcia, M. U. Gonzalez, A. Garcia-Martin, A. Cebollada, and G. Armelles. High magneto-optical activity and low optical losses in metal-dielectric au co au sio2 magnetoplasmonic nanodisks. *Adv. Mater.*, 24(10):36–41 (2012).

[28] A. García-Etxarri, R. Gómez-Medina, L. S. Froufe-Pérez, C. López, L. Chantada, F. Scheffold, J. Aizpurua, M. Nieto-Vesperinas, and J. J. Sáenz. Strong magnetic response of submicron silicon particles in the infrared. *Opt. Express*, 19:4815–4826 (2011).

[29] M. Nieto-Vesperinas, R. Gomez-Medina, and J. J. Sáenz. Angle-suppressed scattering and optical forces on submicrometer dielectric particles. *J. Opt. Soc. Am. A*, 28:54–60 (2011).

[30] M. K. Schmidt, R. Esteban, J. J. Sáenz, I. Suárez-Lacalle, S. Mackowski, and J. Aizpurua. Dielectric antennas - a suitable platform for controlling magnetic dipolar emission. *Opt. Express*, 20:13636–13650 (2012).

[31] C. Rockstuhl, Martin G. Salt, and Hans P. Herzig. Analysis of the phonon-polariton response of silicon carbide microparticles and nanoparticles by use of the boundary element method. *J. Opt. Soc. Am. B*, 22:481–487 (2005).

[32] R. Hillenbrand, T. Taubner, and F. Keilmann. Phonon-enhanced light-matter interaction at the nanometre scale. *Nat. Photon.*, 418:159 (2002).

[33] Frank. H. L. Koppens, D. E. Chang, and F. J. Garcia de Abajo. Graphene plasmonics: A platform for strong light-matter interactions. *Nano Lett.*, 11(8):3370–3377 (2011).

[34] J. Chen, M. Badioli, P. Alonso-Gonzalez, S. Florian Huth Thongrattanasiri, J. Osmond, M. Spasenovic, A. Centeno, A. Pesquera, P. Godignon, A. Z. Elorza, N. Camara, F. J. Garcia de Abajo, R. Hillenbrand, and Frank H. L. Koppens. Optical nano-imaging of gate-tunable graphene plasmons. *Nature*, 487:77 – 81 (2012).

[35] Z. Fei, A. S. Rodin, G. O. Andreev, W. Bao, A. S. McLeod, M. Wagner, Zhang, L. M., Z. Zhao, M. Thiemens, G. Dominguez, M. M. Fogler, A. H. Castro Neto, C. N. Lau, F. Keilmann, and D. N. Basov. Gate-tuning of graphene plasmons revealed by infrared nano-imaging. *Nature*, 487:82–85 (2012).

[36] M. Ameen, A. Garcia-Etxarri, M. Schnell, R. Hillenbrand, and J. Aizpurua. Infrared phononic nanoantennas: Localized surface phonon polaritons in sic disks. *Chin. Sci. Bull.*, 55:2625–2628 (2010).

[37] Stefan A. Maier. *Plasmonics: Fundamentals and Applications*. Springer, 2007.

[38] P. B. Johnson and R. W. Christy. Optical constants of the noble metals. *Phys. Rev. B*, 6:4370–4379 (1972).

[39] A. Hatta, Y. Chiba, and W. Suetaka. Infrared absorption study of adsorbed species at metal/water interface by use of the kretschmann configuration. *Surf. Sci.*, 158: 616–623 (1985).

[40] A. V. Zayats, I. I. Smolyaninov, and A. A. Maradudin. Nano-optics of surface plasmon polaritons. *Phys. Rep.*, 408:131 – 314 (2005).

[41] F. J. García-Vidal and L. Martín-Moreno. Transmission and focusing of light in one-dimensional periodically nanostructured metals. *Phys. Rev. B*, 66:155412 (2002).

[42] S. A. Maier, S. R. Andrews, L. Martín-Moreno, and F. J. García-Vidal. Terahertz surface plasmon-polariton propagation and focusing on periodically corrugated metal wires. *Phys. Rev. Lett.*, 97:176805 (2006).

[43] J. Homola, S. S. Yee, and G. Gauglitz. Surface plasmon resonance sensors: review. *Sens. Actuator B-Chem.*, 54:3 – 15 (1999).

[44] K. A. Willets and R. P. Van Duyne. Localized surface plasmon resonance spectroscopy and sensing. *Annu. Rev. Phys. Chem.*, 58(1):267–297 (2007).

[45] E. Hutter and J. H. Fendler. Exploitation of localized surface plasmon resonance. *Adv. Mater.*, 16(19):1685–1706 (2004).

[46] J. N. Anker, W. P. Hall, O. Lyandres, N. C. Shah, J. Zhao, and R. P. Van Duyne. Biosensing with plasmonic nanosensors. *Nat. Mater.*, 7:442–453 (2008).

[47] M. Moskovits. Surface-enhanced spectroscopy. *Rev. Mod. Phys.*, 57:783–826 (1985).

[48] S. Pillai, K. R. Catchpole, T. Trupke, and M. A. Green. Surface plasmon enhanced silicon solar cells. *Journal of Applied Physics*, 101(9):093105 (2007).

[49] K. R. Catchpole and A. Polman. Plasmonic solar cells. *Opt. Express*, 16:21793–21800 (2008).

[50] I. H. El-Sayed, X. Huang, and M. A. El-Sayed. Surface plasmon resonance scattering and absorption of anti-egfr antibody conjugated gold nanoparticles in cancer diagnostics: Applications in oral cancer. *Nano Letters*, 5(5):829–834 (2005).

[51] A. M. Gobin, Min H. Lee, N. J. Halas, W. D. James, R. A. Drezek, and J. L. West. Near-infrared resonant nanoshells for combined optical imaging and photothermal cancer therapy. *Nano Letters*, 7(7):1929–1934 (2007).

[52] C.F. Bohren and D.R. Huffman. *Absorption and Scattering of Light by Small Particles*. John Wiley & Sons, Inc., New York, 1998.

[53] J. Aizpurua, Garnett W. Bryant, Lee J. Richter, F. J. García de Abajo, Brian K. Kelley, and T. Mallouk. Optical properties of coupled metallic nanorods for field-enhanced spectroscopy. *Phys. Rev. B*, 71(23):235420 (2005).

[54] N. Liu, M. L. Tang, M. Hentschel, H. Giessen, and A. P. Alivisatos. Nanoantenna-enhanced gas sensing in a single tailored nanofocus. *Nat. Mater.*, 10:631–636 (2011).

[55] R. Carminati, J.-J. Greffet, C. Henkel, and J.M. Vigoureux. Radiative and non-radiative decay of a single molecule close to a metallic nanoparticle. *Opt. Commun.*, 261(2):368 – 375 (2006).

[56] E. C. Le Ru, W. R. C. Somerville, and B. Auguié. Radiative correction in approximate treatments of electromagnetic scattering by point and body scatterers. *Phys. Rev. A*, 87:012504 (2013).

[57] M. Grzelczak, J. Perez-Juste, P. Mulvaney, and L. M. Liz-Marzan. Shape control in gold nanoparticle synthesis. *Chem. Soc. Rev.*, 37:1783–1791 (1783).

[58] Y. Sun and Y. Xia. Shape-controlled synthesis of gold and silver nanoparticles. *Science*, 298(5601):2176–2179 (2002).

[59] J. B. Gonzalez-Diaz, A. Garcia-Martin, J. M. Garcia-Martin, A. Cebollada, G. Armelles, B. Sepulveda, Y. Alaverdyan, and M. Kall. Plasmonic au co au nanosandwiches with enhanced magneto-optical activity. *Small*, 4(2):202–205 (2008).

[60] Cesar Clavero. Plasmon-induced hot-electron generation at nanoparticle/metal-oxide interfaces for photovoltaic and photocatalytic devices. *Nat. Photon.*, 308:95 – 103 (2014).

[61] E. D. Palik. *Handbook of Optical Constants of Solids*. Academic Press, San Diego, 1991.

[62] M. Wilde, K. Fukutani, W. Ludwig, B. Brandt, J. H. Fischer, S. Schauermann, and H. J. Freund. Influence of carbon deposition on the hydrogen distribution in pd nanoparticles and their reactivity in olefin hydrogenation. *Angew. Chem. Int. Ed.*, 47(48):9289–9293 (2008).

[63] Y. Xiao, W. Dong, and H. F. Busnengo. Reactive force fields for surface chemical reactions: A case study with hydrogen dissociation on pd surfaces. *J. Chem. Phys.*, 132(1):014704 (2010).

[64] F. J. Garcia de Abajo and A. Howie. Retarded field calculation of electron energy loss in inhomogeneous dielectrics. *Phys. Rev. B*, 65(11):115418 (2002).

[65] F. J. García de Abajo and A. Howie. Relativistic electron energy loss and electron - induced photon emission in inhomogeneous dielectrics. *Phys. Rev. Lett.*, 80: 5180–5183 (1998).

[66] C. Langhammer, I. Zorić, B. Kasemo, and B. M. Clemens. Hydrogen storage in pd nanodisks characterized with a novel nanoplasmonic sensing scheme. *Nano Lett.*, 7(10):3122–3127 (2007).

[67] I. Zorić, E. M. Larsson, B. Kasemo, and C. Langhammer. Localized surface plasmons shed light on nanoscale metal hydrides. *Adv. Mater.*, 22(41):4628–4633 (2010).

[68] L. Schlapbach and A. Zuttel. Hydrogen-storage materials for mobile applications. *Nature*, 414(6861):353–358 (2001).

[69] M. Moskovits. Surface-enhanced spectroscopy. *Rev. Mod. Phys.*, 57:783–826 (1985).

[70] S. Nie and S. R. Emory. Probing single molecules and single nanoparticles by surface-enhanced raman scattering. *Science*, 275(5303):1102–1106 (1997).

[71] K. Kneipp, Y. Wang, H. Kneipp, L. T. Perelman, I. Itzkan, R. R. Dasari, and M. S. Feld. Single molecule detection using surface-enhanced raman scattering (sers). *Phys. Rev. Lett.*, 78:1667–1670 (1997).

[72] F. Le, D. W. Brandl, Y. A. Urzhumov, H. Wang, J. Kundu, N. J. Halas, J. Aizpurua, and P. Nordlander. Metallic nanoparticle arrays: A common substrate for both surface-enhanced raman scattering and surface-enhanced infrared absorption. *ACS Nano*, 2(4):707–718 (2008).

[73] Y Zhang, R. andZhang, Z. C. Dong, S. Jiang, C. Zhang, L. G. Chen, L. Zhang, Y. Liao, J. Aizpurua, Y. Luo, J. L. Yang, and J. G. Hou. Chemical mapping of a single molecule by plasmon-enhanced raman scattering. *Nature*, 498:82–86 (2013).

[74] F. Neubrech, A. Pucci, T. W. Cornelius, S. Karim, A. Garcia-Etxarri, and J. Aizpurua. Resonant plasmonic and vibrational coupling in a tailored nanoantenna for infrared detection. *Phys. Rev. Lett.*, 101:157403 (2008).

[75] D. Enders and A. Pucci. Surface enhanced infrared absorption of octadecanethiol on wet-chemically prepared au nanoparticle films. *Appl. Phys. Lett.*, 88:184104 (2006).

[76] J. C. Ginn, R. L. Jarecki, E. A. Shaner, and P. S. Davids. Infrared plasmons on heavily-doped silicon. *J. Appl. Phys.*, 110(4):043110 (2011).

[77] A. Berrier, P. Albella, M. Ameen Poyli, R. Ulbricht, M. Bonn, J. Aizpurua, and J. Gómez Rivas. Detection of deep-subwavelength dielectric layers at terahertz frequencies using semiconductor plasmonic resonators. *Opt. Express*, 20(5):5052–5060 (2012).

[78] G. Pellegrini, G. Mattei, and P. Mazzoldi. Light extraction with dielectric nanoantenna arrays. *ACS Nano*, 3(9):2715–2721 (2009).

[79] A.E. Krasnok, A.E. Miroshnichenko, P.A. Belov, and Yu.S. Kivshar. Huygens optical elements and yagi uda nanoantennas based on dielectric nanoparticles. *J. Exp. Theor. Phys.*, 94(8):593–598 (2011).

[80] Y. H. Fu, A. I. Kuznetsov, A. E. Miroshnichenko, Y. F. Yu, and B. Luk/'yanchuk. Directional visible light scattering by silicon nanoparticles. *Nat. Commun.*, 4:1527 (2013).

[81] U. Zywietz, A. B. Evlyukhin, C. Reinhardt, and B. N. Chichkov. Laser printing of silicon nanoparticles with resonant optical electric and magnetic responses. *Nat. Commun.*, 5:3402 (2014).

[82] A. B. Evlyukhin, C. Reinhardt, A. Seidel, B. S. Luk'yanchuk, and B. N. Chichkov. Optical response features of si-nanoparticle arrays. *Phys. Rev. B*, 82:045404 (2010).

[83] A. B. Evlyukhin, S. M. Novikov, U. Zywietz, R. Lynge Eriksen, C. Reinhardt, Sergey I. B., and B. N. Chichkov. Demonstration of magnetic dipole resonances of dielectric nanospheres in the visible region. *Nano Lett.*, 12(7):3749–3755 (2012).

[84] A. E. Krasnok, A. E. Miroshnichenko, P. A. Belov, and Y. S. Kivshar. All-dielectric optical nanoantennas. *Opt. Express*, 20(18):20599–20604 (2012).

[85] B. Rolly, B. Bebey, S. Bidault, B. Stout, and N. Bonod. Promoting magnetic dipolar transition in trivalent lanthanide ions with lossless mie resonances. *Phys. Rev. B*, 85:245432 (2012).

[86] C. M. Dodson and R. Zia. Magnetic dipole and electric quadrupole transitions in the trivalent lanthanide series: Calculated emission rates and oscillator strengths. *Physical Review B*, 86(12):125102 (2012).

[87] S. Karaveli and R. Zia. Spectral tuning by selective enhancement of electric and magnetic dipole emission. *Physical Review Letters*, 106(19):193004 (2011).

[88] B. Rolly, B. Stout, and N. Bonod. Boosting the directivity of optical antennas with magnetic and electric dipolar resonant particles. *Opt. Express*, 20:20376–20386 (2012).

[89] M. Kerker, D.-S. Wang, and C. L. Giles. Electromagnetic scattering by magnetic spheres. *J. Opt. Soc. Am.*, 73:765–767 (1983).

[90] J. M. Geffrin, J. J. Sáenz, and F. *et al.* Moreno. Magnetic and electric coherence in forward- and back-scattered electromagnetic waves by a single dielectric subwavelength sphere. *Nat Commun*, 20:1171 (2012).

[91] S. Person, M. Jain, Z. Lapin, J. J. Sáenz, G. Wicks, and L. Novotny. Demonstration of zero optical backscattering from single nanoparticles. *Nano Lett.*, 13(4):1806–1809 (2013).

[92] M. Nieto-Vesperinas, J. J. Sáenz, R. Gómez-Medina, and L. Chantada. Optical forces on small magnetodielectric particles. *Opt. Express*, 18(11):11428–11443 (2010).

[93] R. Gómez-Medina, B. García-Cámara, I. Suárez-Lacalle, L.S. Froufe-Pérez, F. González, F. Moreno, M. Nieto-Vesperinas, and J.J. Sáenz. Electric and magnetic optical response of dielectric nanospheres: Optical forces and scattering anisotropy. *Phot. Nano. Fund. Appl.*, 10:345–352 (2012).

[94] A. J. Huber, B. Deutsch, L. Novotny, and R. Hillenbrand. Focusing of surface phonon polaritons. *Appl. Phys. Lett.*, 92:203104 (2008).

[95] Bo E. Sernelius. *Surface modes in Physics, 1st Ed.* Wiley-VCH, Berlin, 2001.

[96] R. Esteban, J. Aizpurua, and G. W. Bryant. Strong coupling of single emitters interacting with phononic infrared antennae. *New J. Phys.*, 16(1):013052 (2014).

[97] J. Le Gall, M. Olivier, and J.-J. Greffet. Experimental and theoretical study of reflection and coherent thermal emissionby a sic grating supporting a surface-phonon polariton. *Phys. Rev. B*, 55:10105–10114 (1997).

[98] J. J. Greffet, R. Carminati, K. Joulain, J. P. Mulet, S. Mainguy, and Y. Chen. Coherent emission of light by thermal sources. *Nature*, 416:61 (2002).

[99] J. A. Schuller, T. Taubner, and M. L. Brongersma. Optical antenna thermal emitters. *Nat Photon*, 3:658–661 (2009).

[100] J. Renger, S. Grafström, L. M. Eng, and R. Hillenbrand. Resonant light scattering by near-field-induced phonon polaritons. *Phys. Rev. B*, 71:075410 (2005).

[101] Mark S. Anderson. Surface enhanced infrared absorption by coupling phonon and plasma resonance. *Applied Physics Letters*, 87(14):144102 (2005).

[102] A.J. Huber, N. Ocelic, and R. Hillenbrand. Local excitation and interference of surface phonon polaritons studied by near-field infrared microscopy. *J. Microsc.*, 229(3):389–395 (2008).

[103] E. Prodan, C. Radloff, N. J. Halas, and P. Nordlander. A hybridization model for the plasmon response of complex nanostructures. *Science*, 302:419–422 (2003).

[104] H. Xu, J. Aizpurua, M. Käll, and P. Apell. Electromagnetic contributions to single-molecule sensitivity in surface-enhanced raman scattering. *Phys. Rev. E*, 62:4318–4324 (2000).

[105] Aitzol Garcia Etxarri. *Modelization of plasmonic nanoantennas for optical microscopy and surface enhanced spectroscopy.* PhD thesis, Departamento de Fisica de Materiales, The University of the Basque Country, Spain., October 2010.

[106] M. Shahzad, G. Medhi, R. E. Peale, W. R. Buchwald, J. W. Cleary, R. Soref, Glenn D. Boreman, and O. Edwards. Infrared surface plasmons on heavily doped silicon. *J. Appl. Phys.*, 110(12):123105 (2011).

[107] D. Li and C. Z. Ning. All-semiconductor active plasmonic system in mid-infrared wavelengths. *Opt. Express*, 19(15):14594–14603 (2011).

[108] S. Law, L. Yu, A. Rosenberg, and D. Wasserman. All-semiconductor plasmonic nanoantennas for infrared sensing. *Nano Lett.*, 13(9):4569–4574 (2013).

[109] P. Biagioni, J-S. Huang, and B. Hecht. Nanoantennas for visible and infrared radiation. *Rep. Prog. Phys.*, 75(2):024402 (2012).

[110] R. H. Jacobsen, D. M. Mittleman, and M. C. Nuss. Chemical recognition of gases and gas mixtures with terahertz waves. *Opt. Lett.*, 21(24):2011–2013 (1996).

[111] T. R. Globus, D. L. Woolard, T. Khromova, T. W. Crowe, M. Bykhovskaia, B. L. Gelmont, J. Hesler, and A. C. Samuels. Thz-spectroscopy of biological molecules. *Journal of Biological Physics*, 29:89–100 (2003).

[112] M. Tonouchi. Cutting-edge terahertz technology. *Nat. Photon.*, 1:97 – 105 (2007).

[113] P. U. Jepsen, D. G. Cooke, and M. Koch. Terahertz spectroscopy and imaging modern techniques and applications. *Laser Photon. Rev.*, 5(1):124–166 (2011).

[114] D. F. Plusquellic, K. Siegrist, E. J. Heilweil, and O. Esenturk. Applications of terahertz spectroscopy in biosystems. *ChemPhysChem*, 8(17):2412–2431 (2007).

[115] P. Y. Han and X.-C. Zhang. Coherent, broadband midinfrared terahertz beam sensors. *Appl. Phys. Lett.*, 73(21):3049–3051 (1998).

[116] Y. C. Shen, T. Lo, P. F. Taday, B. E. Cole, W. R. Tribe, and M. C. Kemp. Detection and identification of explosives using terahertz pulsed spectroscopic imaging. *Applied Physics Letters*, 86:241116 (2005).

[117] A. G. Davies, A. D. Burnett, W. Fan, E. H. Linfield, and J. E. Cunningham. Terahertz spectroscopy of explosives and drugs. *Materials Today*, 11(3):18 – 26 (2008).

[118] P. J. Burke, S. Li, and Z. Yu. Quantitative theory of nanowire and nanotube antenna performance. *Nanotechnology, IEEE Transactions on*, 5:314–334 (2006).

[119] S. Li, Z. Yu, S. F. Yen, W. C. Tang, and P. J. Burke. Carbon nanotube transistor operation at 2.6 GHz. *Nano Lett.*, 4(4):753–756 (2004).

[120] M. Nagel, P. H. Bolivar, M. Brucherseifer, H. Kurz, A. Bosserhoff, and R. Buttner. Integrated thz technology for label-free genetic diagnostics. *Appl. Phys. Lett.*, 80 (1):154–156 (2002).

[121] L. Razzari and E. N. M. Fabrizio *et al.* Nanoantenna enhanced terahertz spectroscopy of a monolayer of cadmium selenide quantum dots. In *CLEO: 2014*, page SW3F.4 (2014). OSA, 2014.

[122] J. M. Jornet and I. F. Akyildiz. Graphene-based nano-antennas for electromagnetic nanocommunications in the terahertz band communication in nanonetworks. *Proceedings of the Fourth European Conference on Antennas and Propagation (EuCAP)*, pages 1–5 (2010).

[123] I. Llatser, C. Kremers, A. Cabellos-Aparicio, M. J. Jornet, E. Alarcon, and D. N. Chigrin. Graphene-based nano-patch antenna for terahertz radiation. *Phot. Nano. Fund. Appl.*, 10(4):353–358 (2012).

[124] S. Li, M. M. Jadidi, T. E. Murphy, and G. Kumar. Terahertz surface plasmon polaritons on a semiconductor surface structured with periodic v-grooves. *Opt. Express*, 21(6):7041–7049 (2013).

[125] A. Yu. Nikitin, F. Guinea, F. J. Garcia-Vidal, and L. Martin-Moreno. Surface plasmon enhanced absorption and suppressed transmission in periodic arrays of graphene ribbons. *Phys. Rev. B*, 85:081405 (2012).

[126] A. Yu. Nikitin, F. Guinea, F. J. García-Vidal, and L. Martín-Moreno. Edge and waveguide terahertz surface plasmon modes in graphene microribbons. *Phys. Rev. B*, 84:161407 (2011).

[127] A. Yu. Nikitin, F. Guinea, F. J. Garcia-Vidal, and L. Martin-Moreno. Fields radiated by a nanoemitter in a graphene sheet. *Phys. Rev. B*, 84:195446 (2011).

[128] M. Z. Hasan and C. L. Kane. Colloquium: Topological insulators. *Rev. Mod. Phys.*, 82:3045–3067 (2010).

[129] F. Francois, E. Ludovic, and B. Gérard. Optical properties of nanostructured materials a review. *J. Nanophoton.*, 5:052502 (2011).

[130] S. Lal, S. Link, and N. J. Halas. Nano-optics from sensing to waveguiding. *Nat. Photon.*, 1:641–648 (2007).

[131] M. W. Knight, N. S. King, L. Liu, H. O. Everitt, P. Nordlander, and N. J. Halas. Aluminum for plasmonics. *ACS Nano*, 8(1):834–840 (2014).

[132] M. Yamauchi, H. Kobayashi, and H. Kitagawa. Hydrogen storage mediated by pd and pt nanoparticles. *ChemPhysChem*, 10(15):2566–2576 (2009).

[133] P. A. Bennett and J. C. Fuggle. Electronic structure and surface kinetics of palladium hydride studied with x-ray photoelectron spectroscopy and electron-energy-loss spectroscopy. *Phys. Rev. B*, 26:6030–6039 (1982).

[134] W. E. Vargas, I. Rojas, D. E. Azofeifa, and N. Clark. Optical and electrical properties of hydrided palladium thin films studied by an inversion approach from transmittance measurements. *Thin Solid Films*, 496(2):189 – 196 (2006).

[135] A. Pundt and R. Kirchheim. Hydrogen in metals: Microstructural aspects. *Annu. Rev. Mater.*, 36:555–608 (2006).

[136] F. Favier, E. C. Walter, Michael P. Zach, T. Benter, and R. M. Penner. Hydrogen sensors and switches from electrodeposited palladium mesowire arrays. *Science*, 293(5538):2227–2231 (2001).

[137] V. M. Silkin, I. P. Chernov, Yu. M. Koroteev, and E. V. Chulkov. Low-energy collective electronic excitations in pd metal. *Phys. Rev. B*, 80(24):245114 (2009).

[138] U. Eberle, M. Felderhoff, and F. Schulth. Chemical and physical solutions for hydrogen storage. *Angew. Chem. Int. Ed.*, 48:6608–6630 (2009).

[139] V. M. Silkin, R. Díez Muiño, I. P. Chernov, E. V. Chulkov, and P. M. Echenique. Tuning the plasmon energy of palladium hydrogen systems by varying the hydrogen concentration. *J. Phys.: Condens. Matter.*, 24(10):104021 (2012).

[140] B. Xie, L. Liu, X. Peng, Y. Zhang, Q. Xu, M. Zheng, T. Takiya, and M. Han. Optimizing hydrogen sensing behavior by controlling the coverage in pd nanoparticle films. *J. Phys. Chem. C*, 115(32):16161–16166 (2011).

[141] A. Tittl, C. tian Kremers, J. Dorfmüller, D. N. Chigrin, and H. Giessen. Spectral shifts in optical nanoantenna-enhanced hydrogen sensors. *Opt. Mater. Express*, 2 (2):111–118 (2012).

[142] C. Langhammer, Vladimir P. Zhdanov, Igor Zorić, and Bengt Kasemo. Size-dependent kinetics of hydriding and dehydriding of pd nanoparticles. *Phys. Rev. Lett.*, 104(13):135502 (2010).

[143] A. Tittl, P. Mai, R. Taubert, D. Dregely, N. Liu, and H. Giessen. Palladium-based plasmonic perfect absorber in the visible wavelength range and its application to hydrogen sensing. *Nano Lett.*, 11:4366–4369 (2011).

[144] M. Ameen Poyli, V. M. Silkin, I. P. Chernov, P. M. Echenique, R. Díez Muiño, and J. Aizpurua. Multiscale theoretical modeling of plasmonic sensing of hydrogen uptake in palladium nanodisks. *J. Phys. Chem. Lett.*, 3(18):2556–2561 (2012).

[145] B. Ingham, M. F. Toney, S. C. Hendy, T. Cox, D. D. Fong, J. A. Eastman, P. H. Fuoss, K. J. Stevens, A. Lassesson, S. A. Brown, and M. P. Ryan. Particle size effect of hydrogen-induced lattice expansion of palladium nanoclusters. *Phys. Rev. B*, 78:245408 (2008).

[146] R. J. Wolf, M. W. Lee, R. C. Davis, P.J. Fay, and J. R. Ray. Pressure-composition isotherms for palladium hydride. *Phys. Rev. B*, 48(17):12415–12418 (1993).

[147] R. Díez Muiño, D. Sánchez-Portal, V. M. Silkin, E. V. Chulkov, and P. M. Echenique. Time-dependent electron phenomena at surfaces. *Proc. Natl. Acad. Sci. U.S.A.*, 108:971–976 (2011).

[148] V. M. Silkin, I. P. Chernov, P. M. Echenique, Yu. M. Koroteev, and E. V. Chulkov. Influence of hydrogen absorption on low-energy electronic collective excitations in palladium. *Phys. Rev. B*, 76(24):245105 (2007).

[149] J. E. Schirber and B. Morosin. Lattice constants of $\beta - \mathrm{PdH}_x$ and $\beta - \mathrm{PdD}_x$ with x near 1.0. *Phys. Rev. B*, 12:117–118 (1975).

[150] Y. Koroteev, O. Gimranova, and I. Chernov. Hydrogen migration in palladium: First-principles calculations. *Phys. Solid State*, 53:896–900 (2011).

[151] E. G. Maksimov, I. I. Mazin, S. N. Rashkeev, and Y. A. Uspenski. First-principles calculations of the optical properties of metals. *J. Phys.: Condens. Matter.*, 18: 833 (1988).

[152] G. M. Fehrenbach. Theoretical prediction of the peak structure in the eels spectrum of palladium. *Phys. Rev. B*, 59:15085–15092 (1999).

[153] E. E. Krasovskii and W. Schattke. Semirelativistic technique for k.p calculations: Optical properties of pd and pt. *Phys. Rev. B*, 63:235112 (2001).

[154] V.J. Keast. Ab initio calculations of plasmons and interband transitions in the low-loss electron energy-loss spectrum. *J. Electron. Spectrosc. Relat. Phenom.*, 143:97 – 104 (2005).

[155] F. P. Netzer and M. M. El Gomati. Electronic excitations on clean and adsorbate covered pd(111) by angle resolved electron energy loss spectroscopy. *Surf. Sci.*, 124(1):26–38 (1983).

[156] T. Bornemann, J. Eickmans, and A. Otto. Interaction of d-electron excitations and plasmons in pd, ag, cd, in, sn and sb. *Solid State Commun.*, 65(5):381–384 (1988).

[157] H. A. E. Hagelin, J. F. Weaver, G. B. Hoflund, and G. N. Salaita. Electron energy loss spectroscopic investigation of palladium metal and palladium(ii) oxide. *J. Electron. Spectrosc. Relat. Phenom.*, 124(1):1–14 (2002).

[158] J. H. Weaver. Optical properties of rh, pd, ir, and pt. *Phys. Rev. B*, 11:1416–1425 (1975).

[159] J. Aizpurua, P. Hanarp, D. S. Sutherland, M. Käll, Garnett W. Bryant, and F. J. García de Abajo. Optical properties of gold nanorings. *Phys. Rev. Lett.*, 90:057401 (2003).

[160] T. Mitsui, M. K. Rose, E. Fomin, D. F. Ogletree, and M. Salmeron. Dissociative hydrogen adsorption on palladium requires aggregates of three or more vacancies. *Nature*, 422:705–707 (2003).

[161] V. Berube, G. Radtke, M. Dresselhaus, and G. Chen. Size effects on the hydrogen storage properties of nanostructured metal hydrides: A review. *International Journal of Energy Research*, 31:637–663 (2007).

[162] D. A. G. Bruggeman. Bruggeman effective medium approximation. *Ann. Physik (Leipzig)*, 7:636 (1935).

[163] D.E. Aspnes. Plasmonics and effective-medium theories. *Thin Solid Films*, 519 (9):2571 – 2574 (2011).

[164] J. S. Ahn, K. H. Kim, T. W. Noh, Doh-Hyung Riu, Kyung-Ho Boo, and Hyoun-Ee Kim. Effective-medium theories for spheroidal particles randomly oriented on a plane: Application to the optical properties of a sic whisker-al_2o_3 composite. *Phys. Rev. B*, 52:15244–15252 (1995).

[165] J. C. Maxwell Garnett. Colours in metal glasses and in metallic films. *Phil. Trans. R. Soc. Lond. A*, 203:385–420 (1904).

[166] F. Delogu. Smooth size effects in pd and pdhx nanoparticles. *J. Phys. Chem. C*, 114(42):18085–18090 (2010).

[167] E. Yablonovitch. Inhibited spontaneous emission in solid-state physics and electronics. *Phys. Rev. Lett.*, 58:2059–2062 (1987).

[168] S. John. Strong localization of photons in certain disordered dielectric superlattices. *Phys. Rev. Lett.*, 58:2486–2489 (1987).

[169] K. G. Lee, X. W. Chen, H. Eghlidi, P. Kukura, R. Lettow, A. Renn, V. Sandoghdar, and S. Gotzinger. A planar dielectric antenna for directional single-photon emission and near-unity collection efficiency. *Nat. Photon.*, 5:166–169 (2011).

[170] A. Devilez, B. Stout, and N. Bonod. Compact metallo-dielectric optical antenna for ultra directional and enhanced radiative emission. *ACS Nano*, 4(6):3390–3396 (2010).

[171] T. H. Taminiau, S. Karaveli, N. F. van Hulst, and R. Zia. Quantifying the magnetic nature of light emission. *Nat. Commun.*, 3:1–6 (2012).

[172] A. Taflove. Application of the finite-difference time-domain method to sinusoidal steady-state electromagnetic-penetration problems. *Electromagnetic Compatibility, IEEE Transactions on*, EMC-22(3):191–202 (1980).

[173] P. Anger, P. Bharadwaj, and L. Novotny. Enhancement and quenching of single-molecule fluorescence. *Physical Review Letters*, 96(11):113002 (2006).

[174] X. W. Chen, M. Agio, and V. Sandoghdar. Metallodielectric hybrid antennas for ultrastrong enhancement of spontaneous emission. *Phys. Rev. Lett.*, 108:233001 (2012).

[175] S. Reitzenstein, S. Münch, P. Franeck, A. Rahimi-Iman, A. Löffler, S. Höfling, L. Worschech, and A. Forchel. Control of the strong light-matter interaction between an elongated $in_{0.3}ga_{0.7}As$ quantum dot and a micropillar cavity using external magnetic fields. *Phys. Rev. Lett.*, 103:127401 (2009).

[176] P. Nordlander, C. Oubre, E. Prodan, K. Li, and M. I. Stockman. Plasmon hybridization in nanoparticle dimers. *Nano Lett.*, 4(5):899–903.

[177] Chen-To Tai. *Dyadic Green Functions in Electromagnetic Theory, 2nd ed.* IEEE Press, New York, 1993.

[178] Lukas Novotny and Bert Hecht. *Principles of Nano-Optics.* Cambridge University Press, Cambridge, 2006.

[179] J. D. Jackson. *Classical Electrodynamics, 3rd Ed.* John Wiley & Sons, Inc., New York, 2009.

[180] M. Jablan, H. Buljan, and M. Soljacic. Plasmonics in graphene at infrared frequencies. *Phys. Rev. B*, 80:245435 (2009).

[181] M. Orlita and M. Potemski. Dirac electronic states in graphene systems: optical spectroscopy studies. *Semicond. Sci. Technol.*, 25(6):063001 (2010).

[182] A. Manjavacas and F. J. García de Abajo. Tunable plasmons in atomically thin gold nanodisks. *Nat. Commun.*, 5:3548 (2013).

[183] C. L. Kane and E. J. Mele. Quantum spin hall effect in graphene. *Phys. Rev. Lett.*, 95:226801 (2005).

[184] C. Wu, B. A. Bernevig, and S. C. Zhang. Helical liquid and the edge of quantum spin hall systems. *Phys. Rev. Lett.*, 96:106401 (2006).

[185] H. Z. Lu, W. Y. Shan, W. Yao, Q. Niu, and S. Q. Shen. Massive dirac fermions and spin physics in an ultrathin film of topological insulator. *Phys. Rev. B*, 81: 115407 (2010).

[186] H Zhang and S. C. Zhang. Topological insulators in bi2se3, bi2te3 and sb2te3 with a single dirac cone on the surface. *Nature Phys.*, 5:438 – 442 (2009).

[187] D Hsieh and M. Z. Hasan. A tunable topological insulator in the spin helical dirac transport regime. *Nature*, 460:1101–1105 (2009).

[188] Y. P. Lai, I. T. Lin, K. H. Wu, and J. M. Liu. Plasmonics in topological insulators. *Nanomater. Nanotechnol.*, 4:1–8 (2014).

[189] R. Schütky, C. Ertler, A. Trügler, and U. Hohenester. Surface plasmons in doped topological insulators. *Phys. Rev. B*, 88:195311 (2013).

[190] P. Di Pietro, M. Ortolani, O. Limaj, A. Di Gaspare, V. Giliberti, Giorgianni, Brahlek, N. Bansal, N. Koirala, S. Oh, Calvani P., and S. Lupi. Observation of dirac plasmons in a topological insulator. *Nat. Nanotechnol.*, 8:556 – 560 (2013).

[191] J. Qi, H. Liu, and X. C. Xie. Surface plasmon polaritons in topological insulators. *Phys. Rev. B*, 89:155420 (2014).

[192] S. Raghu, S. B. Chung, X. L. Qi, and S. C. Zhang. Collective modes of a helical liquid. *Phys. Rev. Lett.*, 104:116401 (2010).

[193] M. Konig, H. Buhmann, L. W. Molenkamp, T. Hughes, C. X. Liu, Xi. L. Qi, and S. C. Zhang. The quantum spin hall effect: Theory and experiment. *J. Phys. Soc. Jpn.*, 77(3):031007 (2008).

[194] T. Stauber, G. Gómez-Santos, and L. Brey. Spin-charge separation of plasmonic excitations in thin topological insulators. *Phys. Rev. B*, 88:205427 (2013).

[195] A. Fallahi, T. Low, M. Tamagnone, and J. Perruisseau-Carrier. Nonlocal electromagnetic response of graphene nanostructures. *Phys. Rev. B*, 91:121405 (2015).

[196] I. A. Nechaev, R. C. Hatch, M. Bianchi, D. Guan, C. Friedrich, I. Aguilera, J. L. Mi, B. B. Iversen, S. Blügel, Ph. Hofmann, and E. V. Chulkov. Evidence for a direct band gap in the topological insulator bi_2se_3 from theory and experiment. *Phys. Rev. B*, 87:121111 (2013).

[197] M. Stordeur, K. K. Ketavong, A. Priemuth, H. Sobotta, and V. Riede. Optical and electrical investigations of n-type bi2se3 single crystals. *Phys. Status Solidi (b)*, 169(2):505–514 (1992).

[198] N. D. Mermin. Lindhard dielectric function in the relaxation-time approximation. *Phys. Rev. B*, 1:2362–2363 (1970).

[199] D-. X. Qu, Y. S. Hor, J. Xiong, R. J. Cava, and N. P. Ong. Quantum oscillations and hall anomaly of surface states in the topological insulator bi2se3. *Science*, 329:821–824 (2010).

[200] J. Qi, X. Chen, W. Yu, P. Cadden-Zimansky, D. Smirnov, N. H. Tolk, I. Miotkowski, H. Cao, Y. P. Chen, Y. Wu, S. Qiao, and Z. Jiang. Ultrafast carrier and phonon dynamics in bi2se3 crystals. *Appl. Phys. Lett.*, 97:182102 (2010).

[201] Y. D. Glinka, S. Babakiray, T. A. Johnson, A. D. Bristow, M. B. Holcomb, and D. Lederman. Ultrafast carrier dynamics in thin-films of the topological insulator bi2se3. *Appl. Phys. Lett.*, 103:151903 (2013).

[202] J. A. Sobota, S. Yang, J. G. Analytis, Y. L. Chen, I. R. Fisher, P. S. Kirchmann, and Z. X. Shen. Ultrafast optical excitation of a persistent surface-state population in the topological insulator bi_2se_3. *Phys. Rev. Lett.*, 108:117403 (2012).

[203] B. Wunsch, T. Stauber, F. Sols, and F. Guinea. Dynamical polarization of graphene at finite doping. *New J. Phys.*, 8:2362–2363 (2006).

[204] Y. Wang, F. Xiu, L. Cheng, L. He, M. Lang, J. Tang, X. Kou, X.n Yu, X. Jiang, Z. Chen, J. Zou, and K. L. Wang. Gate-controlled surface conduction in na-doped bi2te3 topological insulator nanoplates. *Nano Lett.*, 12(3):1170–1175 (2012).

[205] F. Xiu, L. He, Y. Wang, L. Cheng, Li-Te. Chang, M. Lang, G. Huang, X. Kou, Y. Zhou, X. Jiang, Z. Chen, J. Zou, A. Shailos, and K. L. Wang. Manipulating surface states in topological insulator nanoribbons. *Nat. Nanotechnol.*, 6:216–221 (2011).

[206] R. Esteban, T. V. Teperik, and J. J. Greffet. Optical patch antennas for single photon emission using surface plasmon resonances. *Phys. Rev. Lett.*, 104:026802 (2010).

[207] Lukas Novotny. Effective wavelength scaling for optical antennas. *Phys. Rev. Lett.*, 98:266802 (2007).

[208] Sergey I. Bozhevolnyi and Thomas Søndergaard. General properties of slow-plasmon resonant nanostructures: nano-antennas and resonators. *Opt. Express*, 15(17):10869–10877(2007).

[209] F. J. García de Abajo. Graphene plasmonics: Challenges and opportunities. *ACS Photonics*, 1(3):135–152 (2004).

[210] Sukosin Thongrattanasiri, Alejandro Manjavacas, and F. Javier García de Abajo. Quantum finite-size effects in graphene plasmons. *ACS Nano*, 6(2):1766–1775 (2012).

[211] M. Kuttge, F. J. Garciá de Abajo, and A. Polman. Circular optical nanoantennas: an analytical theory. *Nano Lett.*, 10:125429 (2010).

[212] R. Filter, J. Qi, C. Rockstuhl, and F. Lederer. Circular optical nanoantennas: an analytical theory. *Phys. Rev. B*, 85:125429 (2012).

[213] M. Karamehmedović, R. Schuh, V. Schmidt, T. Wriedt, C. Matyssek, W. Hergert, A. Stalmashonak, G. Seifert, and O. Stranik. Comparison of numerical methods in

near-field computation for metallic nanoparticles. *Opt. Express*, 19(9):8939–8953 (2011).

[214] By A. P. Prudnikov, By Yu.A. Brychkov, and O.I. Marichev. *Integrals and Series*. Taylor & Francis Ltd, London, 1998.

[215] G. A. Niklasson, C. G. Granqvist, and O. Hunderi. Effective medium models for the optical properties of inhomogeneous materials. *Appl. Opt.*, 20(1):26–30 (1981).

[216] A.H. Sihvola and J. A. Kong. Effective permittivity of dielectric mixtures. *IEEE Trans. Geosci. Remote Sens.*, 26:420–429 (1988).

[217] W. Lamb, D. M. Wood, and N. W. Ashcroft. Long-wavelength electromagnetic propagation in heterogeneous media. *Phys. Rev. B*, 21:2248–2266 (1978).

[218] K. Karkkainen, A. Sihvola, and K. Nikoskinen. Analysis of a three-dimensional dielectric mixture with finite difference method. *Geoscience and Remote Sensing, IEEE Transactions on*, 39(5):1013–1018 (2001).

Abbreviations

BEM	**B**oundary **E**lement **M**ethod
FDTD	**F**inite **D**ifference **T**ime **D**omain
LSP	**L**ocalized **S**urface **P**lasmon
LSPR	**L**ocalized **S**urface **P**lasmon **R**esonance
PdH	**P**alladium **H**ydride
SPP	**S**urface **P**lasmon **P**olariton
SEIRA	**S**urface **E**nhanced **I**nfra**R**ed **A**bsorption
SERS	**S**urface **E**nhanced **R**aman **S**cattering
TDDFT	**T**ime **D**ependent **D**ensity **F**unctional **T**heory

CSIC

CFM
Materials Physics Center
Centro de Física de Materiales

DIPC

One of the main goals of nanophotonics is to manipulate light in nanometric regions using extremely compact devices. As demonstrated by many studies, gold and silver particles are very useful for this objective, as they support resonant collective oscillations of electrons at optical frequencies, so called surface plasmons. This thesis researches nanostructures based on alternative materials, which can offer complementary advantages to typical plasmonic systems. By exploiting different electromagnetic resonances in these novel materials, light can be controlled in nanophotonic applications, covering a very large spectral range going from the visible to terahertz. The calculation of the optical response of these nanostructures often requires to combine classical optics together with a microscopic description of the system based on quantum models. This thesis discusses first how the plasmonic response of palladium nanostructures allows to obtain information about the absorption of hydrogen by this material, a process of interest for energy storage. Next, the optical coupling between two dielectric sub-micrometer spheres separated by nanometric distances is analyzed with implications in the context of molecular spectroscopy. Numerical simulations and a dipolar model are combined to analyze the complex interaction between electric and magnetic modes. The third system of interest are thin films made of topological insulators, which exhibit plasmonic modes tunable by an external voltage. These resonances are due to the coupling between two-dimensional plasmons excited in the two flat interfaces of the thin film. In particular, control over the charge and spin properties of the system is demonstrated, with possible applications in spintronics. All together, the novel materials explored in this thesis provide alternative paths to exploit many applications in nanophotonics.